AERODYNAMIC DESIGN OF ACTIVE FLOW CONTROL SYSTEMS AIMED TOWARDS DRAG REDUCTION IN HEAVY VEHICLES

A DISSERTATION
SUBMITTED TO THE DEPARTMENT OF
AERONAUTICS & ASTRONAUTICS
AND THE COMMITTEE ON GRADUATE STUDIES
OF STANFORD UNIVERSITY
IN PARTIAL FULFILLMENT OF THE REQUIREMENTS
FOR THE DEGREE OF
DOCTOR OF PHILOSOPHY

David E. Manosalvas-Kjono
July 2018

This dissertation is online at: http://purl.stanford.edu/ct909cg9679

I certify that I have read this dissertation and that, in my opinion, it is fully adequate in scope and quality as a dissertation for the degree of Doctor of Philosophy.

Antony Jameson, Primary Adviser

I certify that I have read this dissertation and that, in my opinion, it is fully adequate in scope and quality as a dissertation for the degree of Doctor of Philosophy.

Juan Alonso

I certify that I have read this dissertation and that, in my opinion, it is fully adequate in scope and quality as a dissertation for the degree of Doctor of Philosophy.

Brian Cantwell

Approved for the Stanford University Committee on Graduate Studies.

Patricia J. Gumport, Vice Provost for Graduate Education

This signature page was generated electronically upon submission of this dissertation in electronic format. An original signed hard copy of the signature page is on file in University Archives.

Abstract

The trucking industry is an irreplaceable sector of our economy. Over 80% of the world population relies on it for the transportation of commercial and consumer goods. In the US alone, this industry is responsible for over 38% of fuel consumption as it distributes over 70% of our freight tonnage. In the design of these vehicles, particular emphasis has been placed on equipping them with a strong engine, a relatively comfortable cabin, a spacious trailer, and a flat back to improve loading efficiency. The geometrical design of these vehicles makes them prone to flow separation and at highway speeds overcoming aerodynamic drag accounts for over 65% of their energy consumption.

The flat back on the trailer causes flow to separate, which generates a turbulent wake. This region is responsible for a significant portion of the aerodynamic drag and currently the most popular solution is the introduction of flat plates attached to the back of the trailer to push the wake downstream. These passive devices improve the aerodynamic performance of the vehicle, but leave opportunities for significant improvement that can only be achieved with active systems. The current procedure to analyze the flow past heavy vehicles and design add-on drag reduction devices focuses on the use of wind tunnels and full-scale tests. This approach is very time consuming and incredibly expensive, as it requires the manufacturing of multiple models and the use of highly specialized facilities.

This Dissertation presents a computational approach to designing Active Flow Control (AFC) systems to reduce drag and energy consumption for the trucking industry. First, the numerical tools were selected by studying the capabilities of various numerical schemes and turbulence model combinations using canonical bluff bodies. After various numerical studies and comparisons with experimental results, the Jameson-Schmidt-Turkel (JST) scheme in combination with the Shear-Stress-Transport (SST) turbulence model were chosen. This combination of tools was used to study the effect of AFC in the Ground Transportation System (GTS) model, which is a simplified representation of a tractor-trailer introduced by the US Department of Energy to study the separation behind this type of vehicle and the drag it induces.

Using the top-view of the GTS model as a two-dimensional representation of a heavy vehicle, the effect that the Coanda jet-based AFC system has on the wake and integrated forces have been studied. These two-dimensional studies drove the development of the design methodology presented,

and produced the starting condition for the three-dimensional Coanda surface geometry and the jet velocity profile. In addition, the influence in wake stability that this system demonstrated when operating near its optimum drag configuration, allowed for the decoupling of time from the three-dimensional design process.

A design methodology that minimizes the number of required function evaluations was developed by leveraging insights obtained from previous studies; using the physical changes in the flow induced by the AFC system to eliminate the need for time integration during the design process; and leveraging surrogate model optimization techniques . This approach significantly reduces the computational cost during the design of AFC drag reduction systems and has led to the design of a system that reduces drag by over 19% and power by over 16%. In the US trucking fleet alone, these energy savings constitute 8.6 billion gallons of fuel that will not be burned and over 75 million tons of CO_2 that will not be released into the atmosphere each year.

Acknowledgments

The research presented in this dissertation was made possible thanks to the financial support of the Aeronautics & Astronautics Department, the School of Engineering, the Vice Provost of Graduate Educations Gerald J. Lieberman and Diversifying Academia Recruiting Excellence (DARE) Fellowships, the Achievement Rewards for College Scientists (ARCS) Foundation, and the Ford Foundation. These funding sources have afforded me the freedom to explore and select research directions without external constraints. This experience has been very rewarding and has allowed me to think outside the box and more importantly, to grow into an independent researcher. I would also like to thank Extreme Science and Engineering Discovery Environment (XSEDE) under grants TG-DMS150004 and TG-ENG160027, which are supported by National Science Foundation (NSF) grant number ACI-1053575, for the computational resources required to make this work possible.

I would like to thank the members of my committee starting with the chair, Professor Michael Saunders, for being so generous with his time. Professor Robert MacCormack for sharing so many inspiring stories that encouraged me to study Computational Fluid Dynamics (CFD). Professor Brian Cantwell for teaching me the fundamentals of fluid mechanics, helping me to become a better teacher, and always making time to talk about research. Professor Juan Alonso for countless conversations about aerodynamics, and for welcoming me into his lab as an adopted lab member. Finally, I would like to thank my advisor, Professor Antony Jameson, for striking the right combination of guidance and freedom in his advising strategy.

I have been fortunate to work with Dr. Francisco Palacios, Dr. Thomas Economon, and Dr. Carsten Othmer. They welcomed me into the development team of SU2, introduced me to shape and topology optimization, and served as sounding boards for new ideas and research directions. I am truly thankful to have had the opportunity to collaborate and learn from Carsten, Tom, and Francisco, whom in addition to my PhD committee members and my advisor, have been generous, candid, and supportive mentors and collaborators. I look forward to maintaining these connections for many years to come.

My time at Stanford has been incredibly enjoyable, and for this I would like to thank the Faculty and Staff of the Aeronautics & Astronautics Department, the members of the Aerospace Computing Laboratory, the members of the Aerospace Design Laboratory, the SU2 development community

worldwide, the Native American Cultural Center, El Centro Chicano y Latino, the Enhancing Diversity in Graduate Education (EDGE) community, the DARE community and especially the members of the D9 cohort, the Diversity office in the School of Engineering, the Stanford Technology Ventures Programs, and the Graduate Life Office. These organizations have been an active part of my time at Stanford and have given me a platform to give back to the community. In addition, I would like to thank all my Stanford friends without whom I would not have enjoyed my time here as much, as well as my undergrad and high-school friends who have always been there for me.

Finally, I want to thank my family, starting with my wife, Sandy, for all her support and encouragement. It has been fun to work on our PhDs side-by-side and I am looking forward to our next adventure together. To my mom, Cecilia, and grandma, Luz Angelica, thank you for being my inspiration and role models. And thank you to my Dad, Enrique, my brother and sisters, my uncles and aunt, as well as the rest of my family who have always supported my crazy ideas.

Contents

Abstract **iv**

Acknowledgments **vi**

1 Introduction and Background **1**

1.1 Heavy Vehicle Aerodynamics 1

1.1.1 Aerodynamic Features 1

1.1.2 Ground Effect 3

1.1.3 Models Used for the Study of Heavy Vehicles 4

1.2 Drag Reduction Systems 6

1.2.1 Passive Systems 6

1.2.2 Active Systems 7

1.3 Research Objective 8

1.3.1 Contributions 8

1.3.2 Dissertation Layout 9

2 Governing Equations **10**

2.1 Navier-Stokes Equations 10

2.2 Reynolds-Averaged Navier-Stokes Equations 11

2.2.1 Spalart-Allmaras Model 14

2.2.2 Menter Shear-Stress-Transport Model 14

2.3 Selection of Numerical Tools 15

2.3.1 Circular Cylinder 16

2.3.2 Square Cylinder 19

3 Two-Dimensional Studies **22**

3.1 Physical Model 22

3.1.1 Geometrical Model 22

3.1.2 Flow Conditions 24

3.2 Computational Model . . . 25
3.3 Design Optimization . . . 27
3.3.1 Jet Strength Optimization . . . 27
3.3.2 Full System Optimization . . . 33
3.3.3 Conclusion . . . 41

4 Three-Dimensional Studies **43**
4.1 Physical Model . . . 43
4.1.1 Geometrical Model . . . 43
4.1.2 Flow Conditions . . . 45
4.2 Computational Model . . . 47
4.2.1 Velocity Profile . . . 50
4.3 Design Optimization . . . 51
4.3.1 Parametric Study . . . 53
4.3.2 Full Factorial Study . . . 60
4.3.3 Conclusion . . . 66

5 Grid Refinement Studies **68**
5.1 Computational Grids . . . 68
5.2 Flow Features . . . 77
5.3 Base Ground Transportation System . . . 77
5.4 Enhanced Ground Transportation System . . . 83
5.5 Design Outcomes . . . 88

6 Conclusions and Future Directions **90**

A Mesh Study Expanded **92**
A.1 Coarse Level Grids . . . 92
A.2 Mid Level Grids . . . 96
A.3 Fine Level Grids . . . 100
A.4 Extra Fine Level Grids . . . 104

Bibliography **109**

List of Tables

2.1 Results for the circular cylinder M = 0.1. $\overline{C_d}$ is the time-averaged drag coefficient, Re is the Reynolds number, S_t is the Strouhal number, θ_s is the average angle at which it separates, and C_b is the pressure coefficient inside the wake of the cylinder. 17

2.2 Results for the square cylinder at Re = 22,000 and M = 0.1. x_r/h is the recirculation length, $\overline{C_d}$ is the time averaged drag coefficient, $\widetilde{c_d}$ is the drag coefficient variance, $\widetilde{c_l}$ is the lift coefficient variance, and S_t is the Strouhal number. 20

3.1 Results for the Ground Transportation System (GTS) model and the enhanced GTS model injecting flow through Coanda jets in the trailing end at momentum coefficients ranging from 0.0 to 0.0501. C_μ is the jet momentum coefficient, $\overline{C_D}$ is the time averaged drag coefficient, $\overline{C_{Pow}}$ is the time averaged power coefficient, $\widetilde{c_D}$ is the drag coefficient variance, $\widetilde{c_{LF}}$ is the lateral force coefficient variance, and S_t is the Strouhal number. 31

3.2 Results for the GTS model and the enhanced GTS model injecting flow through the Coanda jets in the trailing end at momentum coefficients ranging from 0.00 to 0.05 and Coanda radius from 0.01 to 0.0286 m. C_μ is the jet momentum coefficient, $\overline{C_D}$ is the time averaged drag coefficient, $\widetilde{c_D}$ is the drag coefficient variance, $\widetilde{c_{LF}}$ is the lateral force coefficient variance, C_P is the power coefficient, and St is the Strouhal number. 35

4.1 Summary of the momentum coefficient and the corresponding velocities for each jet. C_μ is the total momentum coefficient, C_{μ_j} is the momentum coefficient per jet, $V_{tb_{peak}}$ is peak velocity for the top and bottom jets in $\frac{m}{s}$, $V_{ps_{peak}}$ is the peak velocity for the port and starboard jets in $\frac{m}{s}$. 53

4.2 Experimental and computational results for the flow past the base GTS model. *Supports* are the number of cylindrical supports holding the GTS model, Re_W is the width based Reynolds number, and C_D is the vehicle drag coefficient. 54

4.3 Parametric study results for a Coanda jet-based Active Flow Control (AFC) system mounted in the trailing end of the GTS model. C_μ is the total momentum coefficient, C_{μ_j} is the momentum coefficient per jet, C_D is the drag coefficient and C_{Pow} is the power coefficient. 56
4.4 C_D and C_{Pow} break down. C_μ is the jet momentum coefficient, $C_{D\ back}$ is the drag contribution from the back of the truck, $C_{D\ Coanda}$ is the drag contribution from the Coanda surfaces, C_D is the vehicle drag coefficient, $C_{Pow\ aero}$ is the power required to overcome aerodynamic drag, $C_{Pow\ comp}$ is the power required to energize the jets and C_{Pow} is the overall required power coefficient. 59
4.5 Blowing strength configurations and resulting drag and power coefficients for the full-factorial study of a GTS model outfitted with the AFC system. $C_{\mu B}$ is the bottom jet momentum coefficient, $V_{PBottom}$ is the peak velocity on the bottom jet, $C_{\mu T}$ is the top jet momentum coefficient, V_{PTop} is the peak velocity on the top jet, $C_{\mu S}$ is the momentum coefficient on each of the side jets, V_{PSide} is the peak velocity on each of the side jets, C_D is the drag coefficient and C_{Pow} is the power coefficient. 62

5.1 Summary of the family of meshes used to study the effects of mesh resolution in the GTS model with and without the AFC system. 76
5.2 Drag breakdown for the base GTS model. C_D is the vehicle drag coefficient, $C_{D\ Pressure}$ is the pressure contribution to drag, $C_{D\ Friction}$ is the viscous friction contribution to drag, $C_{D\ Front}$ is the pressure contribution to drag from the front of the vehicle, and $C_{D\ Back}$ is the pressure contribution to drag from the back of the vehicle. 79
5.3 Drag breakdown for the GTS model outfitted with an AFC system. C_D is the vehicle drag coefficient, $C_{D\ Pressure}$ is the pressure contribution to drag, $C_{D\ Friction}$ is the viscous friction contribution to drag, $C_{D\ Front}$ is the pressure contribution to drag from the front of the vehicle, and $C_{D\ Back}$ is the pressure contribution to drag from the back of the vehicle. 84
5.4 Summary of the drag changes in the base GTS and model outfitted with an AFC system due to mesh resolution. C_D is the vehicle drag coefficient, $C_{D\ Front}$ is the pressure contribution to drag from the front of the vehicle, and $C_{D\ Back}$ is the pressure contribution to drag from the back of the vehicle, ΔC_D is the percentage change in drag due to the AFC system. 88

List of Figures

1.1 Horizontal contribution to the integrated forces by the pressure acting in the front of the Ground Transportation System (GTS) model. The contribution to drag is shown in red and the contribution against it is in green. 2
1.2 Streamlines showing the flow past the Ground Transportation System (GTS) model. 3
1.3 Models used to study the aerodynamic behavior of ground vehicles. 3
1.4 Three-dimensional model of the Ground Transportation System (GTS). 4
1.5 Three-dimensional model of the Generic European Transport System (GETS). . . . 5
1.6 Three-dimensional model of the Generic Conventional Model (GCM). 5

2.1 Computational grid for the circular cylinder. 16
2.2 Mach number contours of the time history of the streamlines past a circular cylinder. T represents one shedding period. 18
2.3 Computational grid for the square cylinder. 19
2.4 Mach number contours of the time history of the streamlines past a square cylinder. T represents one shedding period. 21

3.1 Baseline three-dimensional Customized Ground Transportation System (CGTS) model - Scale 6.5%. All dimensions in meters. 23
3.2 Three-dimensional CGTS model with Coanda Jets in the trailing edge - Scale 6.5%. All dimensions in meters. 23
3.3 Two-dimensional CGTS models - Scale 6.5%. All dimensions in meters. 24
3.4 Coanda jet model and flow features. 24
3.5 Computational grid for the two-dimensional base CGTS model. 26
3.6 Computational grid for the two-dimensional enhanced CGTS model. 27

3.7 Process used to refine the surrogate model for the drag coefficient C_D. The dashed lines represent the 95% certainty limits. (a) shows the surrogate model developed by using only three function evaluations and the suggested location for the next function evaluation by the expected improvement function. (b) shows the improved model obtained by using four function evaluations and the suggested next function evaluation location. (c) shows the surrogate model generated using five function evaluations. (d) Shows the surrogate model generated after evaluating the predicted minimum using the surrogate model shown in (c). 29
3.8 Mach number contours of the base GTS model. 30
3.9 Mach number contours of the enhanced GTS model without jet injection. 30
3.10 Surrogate models for the drag and power coefficients as a function of momentum coefficient. 31
3.11 Mach number contours of the enhanced GTS model injecting air through the AFC system with $C_\mu = 0.0336$. 32
3.12 Coanda jet geometry deformation. 33
3.13 Surrogate model of the power coefficient (C_{Pow}) as a function of momentum coefficient (C_μ) and Coanda radius. The blue markers are the sampling locations used to generate the response surface. 36
3.14 Pressure contours of the GTS model. Pressure in Pascals. 37
3.15 Mach number contours of the GTS model. 37
3.16 Snapshot of the Enhanced GTS Mach number contour with a Coanda radius = 0.0160 m and $C_\mu = 0.0253$. (Case 7) 38
3.17 Snapshot of the Enhanced GTS Mach number contour with a Coanda radius = 0.0155 m and $C_\mu = 0.043$. (Case 11) 39
3.18 Snapshot of the Enhanced GTS Mach number contour with a Coanda radius = 0.0248 m and $C_\mu = 0.0315$. (Case 12) 39
3.19 Pressure contours of the time history of the streamlines past the base and enhanced GTS model with a Coanda radius of 0.0160 m and C_μ of 0.0253 (Case 7). Tb and Tj represent one shedding period for each the base case and the enhanced case respectively. Pressure in Pascals. 41

4.1 Baseline three-dimensional GTS model - Scale 6.5%. All dimensions in meters. . . . 44
4.2 Three-dimensional GTS model with Coanda Jets in the trailing edge - Scale 6.5%. All dimensions in meters. 44
4.3 Coanda jets in the back of the enhanced GTS model. In the detailed view the top jet is shown in red and the port jet in blue. 46
4.4 Mach number contours of the two-dimensional GTS model. 48
4.5 Grid for the GTS base model. 49

4.6 Grid for the GTS model with Coanda jets 49
4.7 Velocity profile extracted from the 2D Coanda jet. 50
4.8 Normalized transverse velocity profile for the top jet. 52
4.9 Normalized three-dimensional profile for the top jet. 52
4.10 Pressure coefficient and the location of the planes where the wake is visualized in the base GTS model. Cut 1 is located at y/W = 0, cut 2 is located at z/W = 1.05 and cut 3 is located at z/W = 0.35. 55
4.11 Visualization of the wake flow for the base GTS model at a Re_W of 359,900 and a Mach number of 0.09195. 55
4.12 Surrogate models representing the behavior of power and drag for the GTS model outfitted with Coanda jets. 56
4.13 Wake comparison between the base GTS model and the GTS model outfitted with the add-on Coanda jet-base AFC system. (a) and (e) show the non-dimensional axial velocity at plane $y/W = 0$, (b) and (f) show the non-dimensional ground normal velocity at plane $z/W = 1.05$, (c) and (g) show the non-dimensional ground normal velocity at plane $z/W = 0.35$, and (d) and (g) the plane locations in the three-dimensional models. Figures (a), (b), (c), and (d) represent the base GTS and figures (e), (f), (g), and (h) the GTS model outfitted with the AFC system at a blowing strength $C_\mu = 0.01957$ (Case 5). Both simulations took place at a width-based Reynolds number of 359,900, and Mach number of 0.09195. 57
4.14 Pressure coefficient distribution on the back of the base and enhanced GTS model at a Re_W of 359,900 and Mach number of 0.09195. 58
4.15 Pressure coefficient distribution on the back of the enhanced GTS model at a Re_W of 359,900 and Mach number of 0.09195. 59
4.16 Surrogate models of the power coefficient in the left column (a, c, e, g) and the drag coefficient in the right column (b, d, f, h) for the full-factorial study at different bottom jet momentum coefficient values. 61
4.17 Location of the slices used to study the wake of a GTS model outfitted with a Coanda based AFC system. (1) is a vertical slice located at $y/W = 0$, (2) is a horizontal slice located at $z/W = 1.05$ and (3) is a horizontal slice placed at $z/W = 0.35$. Pressure coefficient is shown in the vehicle's surface. 63
4.18 Wake structure and pressure distribution of the flow triggered by the blowing configuration of case 25. (a) shows the back pressure coefficient, (b) is slice 1 showing a contour of the normalized stream-wise velocity, (c) is slice 2 showing a contour of the normalized ground-normal velocity, and (d) is slice 3 showing a contour of the normalized ground-normal velocity. 64

4.19 Wake structure and pressure distribution of the flow triggered by the blowing configuration of case 27. (a) shows the back pressure coefficient, (b) is slice 1 showing a contour of the normalized stream-wise velocity, (c) is slice 2 showing a contour of the normalized ground-normal velocity, and (d) is slice 3 showing a contour of the normalized ground-normal velocity. 64
4.20 Wake structure and pressure distribution of the flow triggered by the blowing configuration of case 15. (a) shows the back pressure coefficient, (b) is slice 1 showing a contour of the normalized stream-wise velocity, (c) is slice 2 showing a contour of the normalized ground-normal velocity, and (d) is slice 3 showing a contour of the normalized ground-normal velocity. 65
4.21 Wake structure and pressure distribution of the flow triggered by the blowing configuration of case 2. (a) shows the back pressure coefficient, (b) is slice 1 showing a contour of the normalized stream-wise velocity, (c) is slice 2 showing a contour of the normalized ground-normal velocity, and (d) is slice 3 showing a contour of the normalized ground-normal velocity. 66

5.1 Coarse level surface grid of the base GTS model. 69
5.2 Coarse level volume grid of the base GTS model. (a), (c), and (e) show the top view perspective of a grid slice located at 0.1 m from the bottom of the vehicle. (b),(d), and (f) show the side view perspective of a grid slice located a the center plane of the vehicle. 70
5.3 Coarse level volume grid of the wake region behind the base GTS model. (a) shows the top view perspective of a grid slice located at 0.1 m from the bottom of the vehicle, and (b) shows the side view perspective of a grid slice located a the center plane of the vehicle. 71
5.4 Coarse level surface grid of the GTS model outfitted with the AFC system. 72
5.5 Side view slice located at the center plane of the vehicle of the Coarse level grid used to capture the boundary layer behavior in the back of the vehicle. 72
5.6 Mid level surface grid of the base GTS model. 73
5.7 Mid level surface grid of the GTS model outfitted with the AFC system. 74
5.8 Fine level surface grid of the base GTS model. 74
5.9 Fine level surface grid of the GTS model outfitted with the AFC system. 75
5.10 Extra fine level surface grid of the base GTS model. 75
5.11 Extra fine level surface grid of the GTS model outfitted with the AFC system. . . . 76
5.12 Pressure distribution in the front of the GTS model at different mesh resolutions. . 78

5.13 Mach number contours to visualize the flow structures in front of the base GTS model at different mesh resolutions. (a), (b), and (c) used the coarse level mesh, (d), (e), and (f) used the mid level mesh, (g), (h), and (i) used the fine level mesh, and (j), (k), and (l) used the extra fine level mesh. 80
5.14 Mach number contours of the flow in the back of the base GTS model at different mesh resolutions. (a), (b), and (c) used the coarse level mesh, (d), (e), and (f) used the mid level mesh, (g), (h), and (i) used the fine level mesh, and (j), (k), and (l) used the extra fine level mesh. 81
5.15 Pressure distribution in the back of the GTS model at different mesh resolutions. . 82
5.16 Pressure distribution in the front of the enhanced GTS model at different mesh resolutions. 83
5.17 Mach number contours to visualize the flow structures in front of the GTS model outfitted with an AFC system at different mesh resolutions. (a), (b), and (c) used the coarse level mesh, (d), (e), and (f) used the mid level mesh, (g), (h), and (i) used the fine level mesh, and (j), (k), and (l) used the extra fine level mesh. 85
5.18 Mach number contours of the flow in the back of the GTS model outfitted with a AFC system at different mesh resolutions. (a), (b), and (c) used the coarse level mesh, (d), (e), and (f) used the mid level mesh, (g), (h), and (i) used the fine level mesh, and (j), (k), and (l) used the extra fine level mesh. 86
5.19 Pressure distribution in the back of the enhanced GTS model at different mesh resolutions. 87
5.20 Drag coefficient history for the base and enhanced GTS models as the mesh resolution changes. 88
5.21 Base drag contribution history of the front and back of the base and enhanced GTS model as the mesh resolution changes. 89

A.1 Coarse level surface grid of the base GTS model. 92
A.2 Coarse level volume grid of the base GTS model. (a), (c), and (e) show the top view perspective of a grid slice located at 0.1 m from the bottom of the vehicle. (b),(d), and (f) show the side view perspective of a grid slice located a the center plane of the vehicle. 93
A.3 Coarse level volume grid of the wake region behind the base GTS model. (a) shows the top view perspective of a grid slice located at 0.1 m from the bottom of the vehicle, and (b) shows the side view perspective of a grid slice located a the center plane of the vehicle. 94
A.4 Coarse level surface grid of the GTS model outfitted with the AFC system. 94

A.5 Coarse level volume grid of the GTS model outfitted with the AFC system. (a), (c), and (e) show the top view perspective of a grid slice located at 0.1 m from the bottom of the vehicle. (b),(d), and (f) show the side view perspective of a grid slice located a the center plane of the vehicle. 95
A.6 Coarse level volume grid of the wake region behind the GTS model outfitted with the AFC system. (a) shows the top view perspective of a grid slice located at 0.1 m from the bottom of the vehicle, and (b) shows the side view perspective of a grid slice located a the center plane of the vehicle. 96
A.7 Mid level surface grid of the base GTS model. 96
A.8 Mid level volume grid of the base GTS model. (a), (c), and (e) show the top view perspective of a grid slice located at 0.1 m from the bottom of the vehicle. (b),(d), and (f) show the side view perspective of a grid slice located a the center plane of the vehicle. 97
A.9 Mid level volume grid of the wake region behind the base GTS model. (a) shows the top view perspective of a grid slice located at 0.1 m from the bottom of the vehicle, and (b) shows the side view perspective of a grid slice located a the center plane of the vehicle. 98
A.10 Mid level surface grid of the GTS model outfitted with the AFC system. 98
A.11 Mid level volume grid of the GTS model outfitted with the AFC system. (a), (c), and (e) show the top view perspective of a grid slice located at 0.1 m from the bottom of the vehicle. (b),(d), and (f) show the side view perspective of a grid slice located a the center plane of the vehicle. 99
A.12 Mid level volume grid of the wake region behind the GTS model outfitted with the AFC system. (a) shows the top view perspective of a grid slice located at 0.1 m from the bottom of the vehicle, and (b) shows the side view perspective of a grid slice located a the center plane of the vehicle. 100
A.13 Fine level surface grid of the base GTS model. 100
A.14 Fine level volume grid of the base GTS model. (a), (c), and (e) show the top view perspective of a grid slice located at 0.1 m from the bottom of the vehicle. (b),(d), and (f) show the side view perspective of a grid slice located a the center plane of the vehicle. 101
A.15 Fine level volume grid of the wake region behind the base GTS model. (a) shows the top view perspective of a grid slice located at 0.1 m from the bottom of the vehicle, and (b) shows the side view perspective of a grid slice located a the center plane of the vehicle. 102
A.16 Fine level surface grid of the GTS model outfitted with the AFC system. 102

A.17 Fine level volume grid of the GTS model outfitted with the AFC system. (a), (c), and (e) show the top view perspective of a grid slice located at 0.1 m from the bottom of the vehicle. (b),(d), and (f) show the side view perspective of a grid slice located a the center plane of the vehicle. 103
A.18 Fine level volume grid of the wake region behind the GTS model outfitted with the AFC system. (a) shows the top view perspective of a grid slice located at 0.1 m from the bottom of the vehicle, and (b) shows the side view perspective of a grid slice located a the center plane of the vehicle. 104
A.19 Extra fine level surface grid of the base GTS model. 104
A.20 Extra fine level volume grid of the base GTS model. (a), (c), and (e) show the top view perspective of a grid slice located at 0.1 m from the bottom of the vehicle. (b),(d), and (f) show the side view perspective of a grid slice located a the center plane of the vehicle. 105
A.21 Extra fine level volume grid of the wake region behind the base GTS model. (a) shows the top view perspective of a grid slice located at 0.1 m from the bottom of the vehicle, and (b) shows the side view perspective of a grid slice located a the center plane of the vehicle. 106
A.22 Extra fine level surface grid of the GTS model outfitted with the AFC system. . . . 106
A.23 Extra fine level volume grid of the GTS model outfitted with the AFC system. (a), (c), and (e) show the top view perspective of a grid slice located at 0.1 m from the bottom of the vehicle. (b),(d), and (f) show the side view perspective of a grid slice located a the center plane of the vehicle. 107
A.24 Extra fine level volume grid of the wake region behind the GTS model outfitted with the AFC system. (a) shows the top view perspective of a grid slice located at 0.1 m from the bottom of the vehicle, and (b) shows the side view perspective of a grid slice located a the center plane of the vehicle. 108

Chapter 1

Introduction and Background

1.1 Heavy Vehicle Aerodynamics

The trucking industry is one of the most prominent in our society [103], as over 80% of the world population relies on it for the transportation of commercial and consumer goods. In the US alone, over 70% of freight tonnage is moved by trucks driving more than 448 billion miles and using over 54 billion gallons of fuel per year [6].

These vehicles spend the majority of their life-cycle traveling at highway speeds ($\sim$ 70 mph) where over 65% of the total energy usage goes towards overcoming aerodynamic drag [58, 37]. The resistance to motion experienced by these vehicles is divided between pressure drag (80%) and parasitic drag (20%) [101].

Heavy vehicles were not designed for aerodynamic efficiency, but to maximize the amount of goods that are being transported. In recent years the tractor has attracted some attention, but the trailer, which contributes over 50% of drag in these vehicles [93, 14], has not changed much. The chosen trailer shape improves packing efficiency but, due to the presence of sharp corners, induces flow separation and the appearance of a low pressure wake. This phenomenon is commonly known as viscous pressure drag or base drag [103, 23].

1.1.1 Aerodynamic Features

Heavy vehicles have a box like shape and have been designed to carry as much cargo as possible, while remaining within the regulated external dimensions [14, 28, 37, 83]. Their aerodynamic profile can be thought of as that of two bluff bodies traveling in tandem near the ground, and as such, many models that encompass this behavior have been used. Taking a flow-through approach to describe the flow for a no-crosswind configuration, the aerodynamic signature of these vehicles is characterized by the presence of a stagnation point in the front. As the flow expands towards the

sides of the vehicle, it speeds up and decreases the surface pressure. The effect of this expansion is enhanced in areas where small turning radii have been used [37]. In the front face of the vehicle, the stagnation point is the main contributor to its pressure distribution and drives the contribution of this section to the stream-wise force.

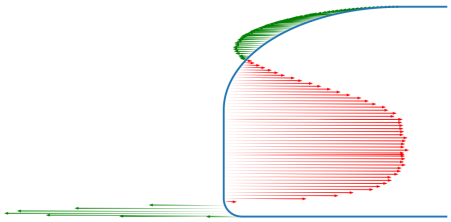

Figure 1.1: Horizontal contribution to the integrated forces by the pressure acting in the front of the Ground Transportation System (GTS) model. The contribution to drag is shown in red and the contribution against it is in green.

Once the flow moves past the front of the vehicle, it transitions to flowing parallel to the free-stream and encounters the junction between the tractor and the trailer. This gap enables the vehicle to have a better turning radius and allows for the modularity of the trailer connection to the tractor. Aerodynamically speaking, the flow separates at the trailing end of the tractor forming steady, symmetric, counter rotating vortices that are trapped within the gap. The gap distance has a significant effect on the behavior of the vortices, vehicle stability, and the overall drag [14]. The counter-rotating vortices produce a low pressure region behind the tractor, which decreases the drag of the trailer while increasing the drag of the truck [31, 34, 60]. As the gap size is decreased, the pressure within this region increases, which decreases the tractor drag and increases the trailer drag. Furthermore, as the gap size continues to decrease the vortex symmetry within this region breaks down, and the gap flow bleeds outside causing separation bubbles on the trailer and an overall vehicle drag increase [11]. Through these studies, it was determined that there is a range of gap distances that minimize the drag penalty and most heavy vehicle operate within this range [31, 60, 11].

The undercarriage contribution to the aerodynamic drag of the vehicle is significant [102]. The flow in this region is perturbed by cables, chains, emergency tires, etc. which are located in this area to support day-to-day operations. In addition, side winds bleed through this area perturbing the flow [67, 60, 90, 15], the wheels and their interaction with the road introduce turbulent structures, and the wheel housing interaction with the free-stream introduce vortical structures [61, 63, 75, 76].

The flow on the top and sides of the vehicle is parallel to the free-stream and exhibits a turbulent

boundary layer. The flow remains attached through the entire length of the vehicle until the back of the trailer where the sharp edge acts as a fixed point of separation. The flow leaving the rear end of the trailer develops shear layers that roll up into vortex rings which extend downstream forming a low pressure turbulent wake [14, 67, 60]. The presence of these flow features is characteristic of bluff body aerodynamics and is the main contributor to the viscous pressure drag, which is also known as base drag [13].

Figure 1.2: Streamlines showing the flow past the Ground Transportation System (GTS) model.

The flow walk through described above is accurate for flat-back – as the one that was been studied by the author – as well as for fast-back vehicles, and can be used as a guideline to understand the aerodynamic characteristics of other vehicle shapes [10, 14, 4, 3, 45].

(a) Ground Transportation System (GTS) representing a flat-back.

(b) Ahmed body [4] representing a fast-back.

Figure 1.3: Models used to study the aerodynamic behavior of ground vehicles.

1.1.2 Ground Effect

Bluff body aerodynamics at high Reynolds numbers are characterized by the presence of vortex shedding and oscillatory, turbulent, unsteady wakes [79, 13]. These structures are present when precautions are taken to assure that the body is not being influenced by its surroundings. As the body is placed closer to a wall, such as the ground, the wake behavior starts to change. The oscillation frequency of the wake drops and becomes stable in the surface normal direction. These aerodynamic changes modify the aerodynamic forces and the structure of the wake, and are referred to as ground effect [44, 2, 14].

1.1.3 Models Used for the Study of Heavy Vehicles

The bluff body behavior inherent to ground vehicles causes the aerodynamic features previously described, but it is important to remember that heavy vehicles have mirrors, antennas, steps, exhaust pipes, etc. which influence and modify the overall flow behavior around the vehicle. To study the fundamental flow features of these vehicles and the systems used to modify them, streamlined models are sufficient [93, 30]. There are various geometries that have been used though the years to study the tractor, the gap size, the wake formation, etc. but since the focus of this work is to better understand drag reduction systems for heavy vehicles, the presented models are the most commonly used subset of those used to study the aerodynamic behavior on flat-back vehicles.

Ground Transportation System (GTS)

This geometrical model was developed by a United States Department of Energy (DoE) consortium to focus on the study of viscous pressure drag. The GTS effectively combines both the tractor and the trailer into a single simplified bluff body that has an elliptical leading shape and ends in a sharp straight cut in the back [30]. There are variations of this geometry, which are referred to as Modified Ground Transportation System (MGTS). The MGTS contains features that increase the model complexity, such as the tractor-trailer gap, wheels, and variations in the model dimensions [58, 23, 14].

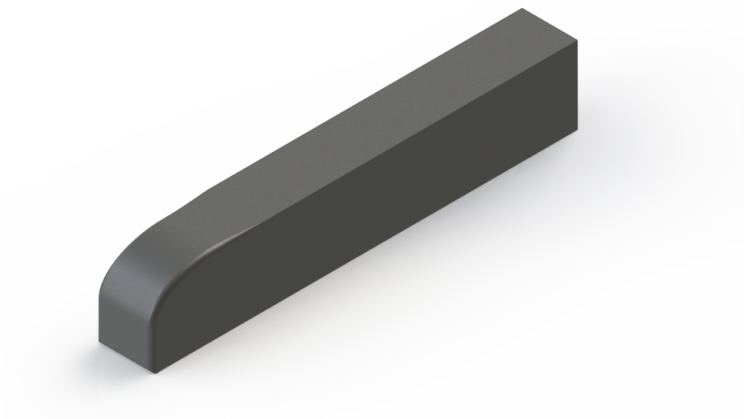

Figure 1.4: Three-dimensional model of the Ground Transportation System (GTS).

Generic European Transport System (GETS)

This model is used to represent heavy vehicle type that is most prevalent in Europe. It is commonly described as the European version of the GTS and the main difference is in the front, where the geometry is rounded in all four corners of the front face [93].

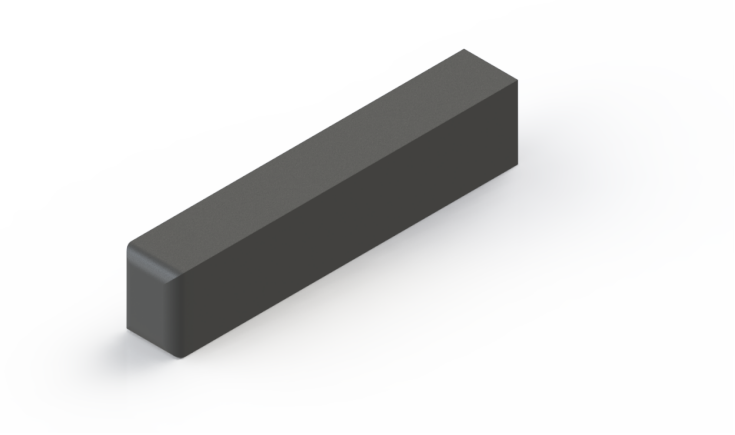

Figure 1.5: Three-dimensional model of the Generic European Transport System (GETS).

Generic Conventional Model (GCM)

This model has a realistic representation of the tractor. It contains the general features representing the bumper, radiator grille, fenders, hood, windshield, and tires. The trailer features a realistic tractor-trailer gap geometry and connection mechanism [91, 34, 60, 24]. Following the same trend as the MGTS, the Modified Generic Conventional Model (MGCM) introduces more features in the tractor, a detailed wheel/rim geometry, mud flaps, and under-body features [14].

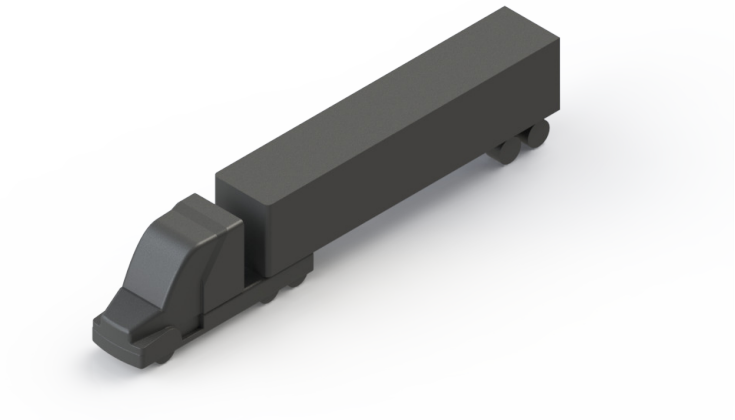

Figure 1.6: Three-dimensional model of the Generic Conventional Model (GCM).

The focus of this dissertation is the study of heavy vehicle base drag and drag reduction systems capable of changing the wake's behavior. Therefore, the GTS model has been chosen as it allows the author to focus exclusively in the separation region in the back and on the optimization of systems

to improve the vehicle power consumption. Nonetheless, an overview of general models for the study of ground vehicle aerodynamics can be found in the work of Han *et al.* [33] and LeGood *et al.* [45].

1.2 Drag Reduction Systems

According to recent studies, the drag on modern trucks could be reduced as much as 50%, which translates into a fuel consumption decrease of 25 to 35% [58, 60, 101]. Just a 12% reduction in fuel consumption across the national fleet of heavy vehicles would save 3.2 billion gallons of diesel per year and prevent the production of 28 million tons of CO_2 emissions [60].

In an effort to reduce fuel consumption, decrease the carbon footprint of the freight transport industry, and improve the profit margins, drag reduction systems have been introduced. For the development and understanding of these systems and the effects they have, the vehicle has been divided in three main parts: forebody (tractor and gap), underbody, and afterbody (trailer) [14]. This differentiation allows for the understanding of each of the sections separately, and leads to the development of simpler models – as shown in Section 1.1.3 – to isolate their contribution to the aerodynamic features and to drag. There are two main avenues to aerodynamic modification of heavy vehicles, the first one introduces significant modifications to the vehicle's geometry and is characterized as passive, and the second one uses small geometry modifications in coalition with blowing and/or suction and is categorized as active.

1.2.1 Passive Systems

Due to regulatory constraints in the trailer of the vehicle, most of the improvements in the early days of aerodynamic awareness for heavy vehicles took place in the tractor [28, 37]. One of the earliest efforts to improve aerodynamic performance in this region was to increase the radius of curvature of corners and edges [37, 83]. After the general geometry was softened, the focus was shifted to the development of add-on mechanisms on the roof of the tractor, which help the incoming flow navigate the change in height between the tractor and trailer, and allow for smooth flow. These devices included vertical fences [5, 14], cap deflectors, and multiple iterations of roof fairings [15, 47, 53, 14].

Another avenue for the improvement of aerodynamic performance in the forebody is the modification of the gap flow, which was described in Section 1.1.1. The techniques used for this purpose include gap enclosures [5, 65], cab-side extenders [11, 15, 38, 90], center body splitter plates in the front face of the trailer [11, 38, 60, 64], splitter plates at the back of the tractor [15], and cross-flow vortex trap plates in the front face of the trailer [102, 104]. All these devices are introduced to reduce the unsteadiness of this region, which in addition to increasing the pressure in the trailing end of the tractor, reduce bleeding and separation in the trailer.

Although considered a significant contributor to aerodynamic drag [102] the underbody has attracted little attention from the community [14]. The main approach taken to address this problem

has been to limit the flow allowed between the ground and the vehicle. The main approach has focused on limiting the perpendicular flow allowed to pass between the ground and the trailer, which has been accomplished by the use of undercarriage skirts, which can be either straight [10, 16, 59, 66] or wedged [16, 90], as well as with the introduction of belly boxes [16, 90]. These devices achieve greater performance when the flow conditions around the vehicle are close to zero yaw angle. The introduction of wedged skirts produce a small range increase in the efficiency of these devices, but they remain best suited to handle zero yaw angle configurations [14, 66]. Belly boxes on the other hand are advantageous as they combine all the benefits of a straight skirt with the functionality of a wheel box, where in addition to blocking the lateral flow, it shields the trailer wheels from cross flow [90]. Furthermore, the undercarriage flow coming parallel to the vehicle has also been studied and in order to reduce its effect in the overall drag an underbody spoiler on the front of the vehicle has been introduced to reduce the flow velocity. [71, 38].

Much effort has been devoted to the study of the afterbody [14]. This region generates a significant drag contribution [102, 37] and features very intricate aerodynamic structures. The flow features for a flat-back model have been described in detail in Section 1.1.1. Passive efforts to decrease drag contribution have mainly come from modifying the wake structure. This aerodynamic modification has been approached by the addition of surfaces to the back of the trailer, such as splitter plates, base cavities, and boat tails [27, 7, 43, 95, 73]. These devices operate by moving the circulation region downstream, which increases base pressure on the trailer at the expense of vehicle length. One feature that sets apart the truncated boat tail is its capability of not only being able to push the recirculating region downstream, but to reduce its size by changing the receding angle of the plates. [32, 100, 17].

1.2.2 Active Systems

Active systems encompass all types of mechanisms that require energy input in order to change the aerodynamic behavior of the vehicle. These have the potential to generate flow field modifications without having to make serious physical changes in the geometry. Designing these types of systems has proven to be a challenge, as the system is required to minimize the overall power consumption while being able to operate.

The forebody has seen aerodynamic improvements by the use of active systems. Mechanisms aimed to improve the aerodynamic behavior of this section include rotating cylinders placed in the top leading edge of the trailer, which streamlines the flow from the tractor to the trailer [53]. This approach smooths out the aerodynamic signature of the vehicle and helps compensate for height differences between these sections. The same effect can be achieved by placing an air jet instead of the rotating cylinder in this location, and similar results have been found for this approach while reducing the system's complexity [23]. Another concept that has been studied is tractor base bleeding [68, 9], where the flow is injected in the base of the tractor and pushes the low pressure region

away from it, which has been shown to be more efficient than side extenders. Although the systems described here are effective in reducing drag, they all incur on operational and implementation costs that make them less attractive.

The afterbody resistance to motion caused by viscous pressure drag can be addressed by streamlining the vehicle, but due to the expected functionality of the trailer, a radical shape change in this area is not feasible. A non-intrusive approach for aerodynamic profile modification can be accomplished by the use of Active Flow Control (AFC) techniques, which operate by reducing the amount of separation behind the vehicle [23]. These aerodynamic changes can be designed to reduce the pressure imbalance between the front and rear of the vehicle and through this avenue decrease its drag [54]. Similar methods to the ones used in the forebody have been tested for this region. The mechanisms include counter rotating cylinders in the top edge of the trailer to reduce separation from the top [87]. Flaps and synthetic jet arrays to improve the efficiency of boat tail types of devices [21]. Base bleeding through a porous media in the back phase of the vehicle to push the low pressure region downstream [36, 49]. The use of steady suction and oscillatory blowing (SaOB) devices to change the wake behavior and increase wake pressure [86, 85]. Finally, Coanda jet-based AFC systems positioned at the trailing edge of the vehicle have been used to maintaining the flow attached longer [23, 54, 74]. Coanda jet systems work by injecting high momentum air in the region of interest, which helps the incoming flow negotiate sharp corners and reduce separation on the trailer. The introduction of these systems not only reduces the wake size and increases base pressure, but also restrains the wake and eliminates its unsteady behavior when used near its optimum configuration. These AFC systems have demonstrated not only drag reduction, resulting in a net power savings of more than 15%, but also an improvement in vehicle stability and safety through the use of flow injection to compensate for the effect of side forces [74].

1.3 Research Objective

1.3.1 Contributions

The research described in this dissertation has established a systematic computational procedure for designing drag reduction systems for heavy road vehicles based in the Coanda effect. First, the available state-of-the-art numerical methods were analyzed for the simulation of bluff body aerodynamics, and the combination of Jameson-Schmidt-Turkel (JST) [42] and Shear-Stress-Transport (SST) [62] was chosen due to its performance with square and circular cylinders. Second, each part of the Coanda jet-based AFC system was analyzed, and the flow changes in the aerodynamic behavior of the vehicle and structure of the wake were studied. Third, leveraging the stabilizing effect of jet injection in the back of the vehicle coupled with ground effect, time-integration has been decoupled from the simulation of the flow past the vehicle, which further reduces the computational resources required for the design of this system. Finally, the use of surrogate model optimization has

been introduced into the design process to significantly reduce the number of function evaluations required to properly explore the design space.

1.3.2 Dissertation Layout

This dissertation presents an introduction to heavy vehicle aerodynamics, the different simplified models used to study it, and methods used to reduce vehicle drag in Chapter 1. Chapter 2 introduces the equations that govern fluid flow, the numerical schemes and turbulence models evaluated, and the analysis used to select the final combination of numerical tools. Chapter 3 presents the two-dimensional simulations over the top-view representation of a GTS model with and without the AFC drag reduction system. This chapter introduces the use of surrogate model optimization, the thermodynamic representation of the compressor model used to energize the AFC system and an in-depth analysis of the flow changes induced by the use of the drag reduction system. Chapter 4 extends the study to three-dimensions, examines the physical changes in the wake structure due to jet injection, and through designs studies finds the optimum jet injection configuration to minimize drag and power consumption. Chapter 5 explores the use of higher mesh resolution and the effect this increase in fidelity has in the integrated forces acting on the vehicle. Chapter 6 outlines the main conclusions of the dissertation and discusses avenues of future research.

Chapter 2

Governing Equations

2.1 Navier-Stokes Equations

The aerodynamic performance of a vehicle is connected to its interaction with the flow around it. To study and analyze the effects of jet injection and virtual shape changes in the vehicle, it is important to look at its aerodynamic profile. The physical changes in flow patterns are modeled using the Navier-Stokes (NS) equations, which govern the motion of viscous fluids in a continuum.

The conservative form of the NS equations in Cartesian coordinates are presented below. Equation 2.1 is the continuity equation, Equations 2.2 are the momentum for each of the three dimensions, and Equation 2.3 is the energy equation.

$$\frac{\partial \rho}{\partial t} + \frac{\partial \rho U}{\partial x} + \frac{\partial \rho V}{\partial y} + \frac{\partial \rho W}{\partial z} = 0 \tag{2.1}$$

$$\begin{aligned}
\frac{\partial \rho U}{\partial t} + \frac{\partial (\rho UU + P - \tau_{xx})}{\partial x} + \frac{\partial (\rho UV - \tau_{xy})}{\partial y} + \frac{\partial (\rho UW - \tau_{xz})}{\partial z} = 0 \\
\frac{\partial \rho V}{\partial t} + \frac{\partial (\rho VU - \tau_{yx})}{\partial x} + \frac{\partial (\rho VV + P - \tau_{yy})}{\partial y} + \frac{\partial (\rho VW - \tau_{yz})}{\partial z} = 0 \\
\frac{\partial \rho W}{\partial t} + \frac{\partial (\rho WU - \tau_{zx})}{\partial x} + \frac{\partial (\rho WV - \tau_{zy})}{\partial y} + \frac{\partial (\rho WW + P - \tau_{zz})}{\partial z} = 0
\end{aligned} \tag{2.2}$$

$$\begin{aligned}
\frac{\partial \rho E}{\partial t} + \frac{\partial \rho EU}{\partial x} + \frac{\partial \rho EV}{\partial y} + \frac{\partial \rho EW}{\partial z} + \frac{\partial (PU - \tau_{xx}U - \tau_{xy}V - \tau_{xz}W)}{\partial x} + \\
\frac{\partial (PV - \tau_{yx}U - \tau_{yy}V - \tau_{yz}W)}{\partial y} + \frac{\partial (PW - \tau_{zx}U - \tau_{zy}V - \tau_{zz}W)}{\partial z} + \\
\frac{\partial Q_x}{\partial x} + \frac{\partial Q_y}{\partial y} + \frac{\partial Q_z}{\partial z} = 0
\end{aligned} \tag{2.3}$$

where the viscous stresses are:

$$\begin{aligned}
\tau_{xx} &= 2\mu\frac{\partial U}{\partial x} + \lambda\left(\frac{\partial U}{\partial x} + \frac{\partial V}{\partial y} + \frac{\partial W}{\partial z}\right), \\
\tau_{yy} &= 2\mu\frac{\partial V}{\partial y} + \lambda\left(\frac{\partial U}{\partial x} + \frac{\partial V}{\partial y} + \frac{\partial W}{\partial z}\right), \\
\tau_{zz} &= 2\mu\frac{\partial W}{\partial z} + \lambda\left(\frac{\partial U}{\partial x} + \frac{\partial V}{\partial y} + \frac{\partial W}{\partial z}\right), \\
\tau_{xy} &= \tau_{yx} = \mu\left(\frac{\partial U}{\partial y} + \frac{\partial V}{\partial x}\right), \\
\tau_{xz} &= \tau_{zx} = \mu\left(\frac{\partial U}{\partial z} + \frac{\partial W}{\partial x}\right), \\
\tau_{yz} &= \tau_{zy} = \mu\left(\frac{\partial V}{\partial z} + \frac{\partial W}{\partial y}\right),
\end{aligned} \tag{2.4}$$

and the heat fluxes are:

$$\begin{aligned}
Q_x &= k\frac{\partial T}{\partial x}, \\
Q_y &= k\frac{\partial T}{\partial y}, \\
Q_z &= k\frac{\partial T}{\partial z},
\end{aligned} \tag{2.5}$$

where ρ is the density; t is time; U, V, and W are the velocity components in the x, y, and z directions respectively; P is the static pressure; E is the total energy per unit mass and is defined as $E = e + \frac{1}{2}(U^2 + V^2 + W^2)$; e is the internal energy per unit mass; μ and λ (-2/3/μ for most ideal gases) are the first and second coefficients of viscosity; k is the heat transfer coefficient; and T is the temperature.

For an ideal gas:

$$P = (\gamma - 1)\rho e, \qquad T = \frac{P}{\rho R}, \qquad R = \frac{C_P}{C_v}, \qquad R = \frac{C_P(\gamma - 1)}{\gamma}, \qquad k = \frac{\mu}{Pr}C_P, \tag{2.6}$$

where γ is the ratio of specific heats, C_P is the specific heat at constant pressure, C_v is the specific heat at constant volume, R the gas constant, and Pr the Prandtl number.

2.2 Reynolds-Averaged Navier-Stokes Equations

Turbulent flow can be idealized as consisting of two components: a slowly varying mean flow and a rapidly fluctuating component related to turbulence. This idealization is known as Reynolds

decomposition [52]. For a typical flow variable z the the decomposition is:

$$z = \bar{z} + z', \tag{2.7}$$

and it is important to note that:

$$z(\bar{t}_0) = \frac{1}{T}\int_{t_0-T/2}^{t_0+T/2} z dt, \qquad \frac{1}{T}\int_{t_0-T/2}^{t_0+T/2} z' dt = 0, \tag{2.8}$$

were $\bar{z}$ is the mean flow quantity averaged over an interval T, which is assumed to be long with respect to the scales of turbulence and short with respect to those of the mean flow [52]. Using a density weighted averaging, also known as Favre averaging [52], the compressible Reynolds-Averaged Navier-Stokes (RANS) equations are:

$$\frac{\partial \bar{\rho}}{\partial t} + \frac{\partial \bar{\rho}\tilde{u}_j}{\partial x_j} = 0, \tag{2.9}$$

$$\frac{\partial \bar{\rho}\tilde{u}_i}{\partial t} + \frac{\partial \bar{\rho}\tilde{u}_i\tilde{u}_j}{\partial x_j} + \frac{\partial \bar{P}}{\partial x_i} + \frac{\partial}{\partial x_j}\left(\bar{\tau}_{ij} + \overline{\rho u_i'' u_j''}\right) = 0, \tag{2.10}$$

$$\frac{\partial \overline{\rho E}}{\partial t} + \frac{\partial \overline{\rho E}\tilde{u}_j}{\partial x_j} + \frac{\partial \bar{P}\tilde{u}_j}{\partial x_j} + \frac{\partial \overline{\rho u_j'' h''}}{\partial x_j} + \frac{\partial}{\partial x_j}\left[\tilde{u}_i\left(\bar{\tau}_{ij} + \overline{\rho u_i'' u_j''} + \overline{u_i''\left(\tau_{ij} - \frac{1}{2}\rho u_i'' u_j''\right)}\right)\right] = 0, \tag{2.11}$$

where:

$$\begin{gathered}
\rho = \bar{\rho} + \rho', \qquad \tilde{u}_i = \frac{\overline{\rho u_i}}{\bar{\rho}}, \qquad \rho u_i = \overline{\rho u_i} + (\rho u_i)', \qquad P = \bar{P} + P', \\
\tau_{ij} = \bar{\tau}_{ij} + \tau_{ij}', \qquad \rho u_i'' u_j'' = \overline{\rho u_i'' u_j''} + (\rho u_i'' u_j'')', \qquad u_i'' = u_i - \tilde{u}_i, \\
\rho E = \overline{\rho E} + (\rho E)', \qquad \rho u_j'' h'' = \overline{\rho u_j'' h''} + (\rho u_j'' h'')', \qquad h'' = h - \tilde{h}, \\
h = H - \frac{1}{2}u_i u_i, \qquad H = E + \frac{P}{\rho}, \qquad \tilde{h} = \frac{\overline{\rho h}}{\bar{\rho}}, \qquad \rho h = \overline{\rho h} + (\rho h)',
\end{gathered} \tag{2.12}$$

where h is the enthalpy per unit of mass, H is the combination of enthalpy and kinetic energy per unit of mass, $\overline{\rho u_i'' u_j''}$ are the Reynolds stress terms, $\frac{\partial \overline{\rho u_j'' h''}}{\partial x_j}$ are the Reynolds heat flux terms, and $\overline{u_i''\left(\tau_{ij} - \frac{1}{2}\rho u_i'' u_j''\right)}$ are the Reynolds dissipation terms. The Reynolds terms, which are the product of averaging, introduce variables that leave the system open. In order for this issue to be addressed, various modeling approaches have been used.

Using the RANS equations for problems involving turbulent flows reduces the amount of resources required. The main savings are a direct result of a decrease in mesh resolution, since this approach

allows for smaller scales to be modeled rather than resolved. The modeling approach used for the research presented in this dissertation is based upon the Boussinesq hypothesis [99] which states that the effect of additional mixing can be represented by the increase of viscosity [52, 20]. The total viscosity is divided into dynamic (μ_{dyn}) and turbulent (μ_{tur}). To close the system of equations the dynamic portion is computed using Sutherland's law [92], shown in Equation 2.13, and the turbulent viscosity through a model involving the flow state and a set of new variables.

$$\mu_{dyn} = 1.716 * 10^{-5} \left[\frac{T}{273.15}\right]^{\frac{3}{2}} \left[\frac{273.15 + 110.4}{T + 110.4}\right] \tag{2.13}$$

The modeling approaches explored in this dissertation are Spalart-Allmaras (SA) model [88] and the Shear-Stress-Transport (SST) model [62], which are the most widely used in engineering applications. To provide a concise definition of the turbulence models the NS equations have been re-written as:

$$\frac{\partial \mathcal{U}}{\partial t} + \nabla \cdot \vec{F}^c - \nabla \cdot (\mu^1_{tot}\vec{F}^{v1} + \mu^2_{tot}\vec{F}^{v2}) - \mathcal{Q} = 0 \tag{2.14}$$

where the conservative variables are given by:

$$\mathcal{U} = \left\{ \begin{array}{c} \rho \\ \rho\vec{v} \\ \rho E \end{array} \right\}, \tag{2.15}$$

and the convective fluxes, viscous fluxes, and source term are:

$$\vec{F}^c = \left\{ \begin{array}{c} \rho\vec{v} \\ \rho\vec{v}\otimes\vec{v} + \bar{\bar{I}}P \\ \rho E\vec{v} + P\vec{v} \end{array} \right\}, \quad \vec{F}^{v1} = \left\{ \begin{array}{c} \cdot \\ \bar{\bar{\tau}} \\ \bar{\bar{\tau}}\cdot\vec{v} \end{array} \right\}, \quad \vec{F}^{v2} = \left\{ \begin{array}{c} \cdot \\ \cdot \\ C_P\nabla T \end{array} \right\}, \quad \mathcal{Q} = \left\{ \begin{array}{c} q_\rho \\ \vec{q}_{\rho\vec{v}} \\ q_{\rho E} \end{array} \right\}, \tag{2.16}$$

where $\vec{v} = \{v_1, v_2, v_3\}^\mathsf{T} \in \mathbb{R}^3$ is the flow speed in a Cartesian system of reference, the viscous stress tensor can be written in vector notation as:

$$\bar{\bar{\tau}} = \nabla\vec{v} + \nabla\vec{v}^\mathsf{T} - \frac{2}{3}\bar{\bar{I}}(\nabla\cdot\vec{v}), \tag{2.17}$$

and

$$\mu^1_{tot} = \mu_{dyn} + \mu_{tur}, \qquad \mu^2_{tot} = \frac{\mu_{dyn}}{Pr_d} + \frac{\mu_{tur}}{Pr_t} \tag{2.18}$$

where Pr_d and Pr_t are the dynamic and turbulent Prandtl numbers.

2.2.1 Spalart-Allmaras Model

The Spalart-Allmaras (SA) model [88] is a one equation model on which the turbulent viscosity is computed as:

$$\mu_{tur} = \rho\hat{\nu} f_{v1}, \quad f_{v1} = \frac{\chi^3}{\chi^3 + c_{v1}^3}, \quad \chi = \frac{\hat{\nu}}{\nu}, \quad \nu = \frac{\mu_{dyn}}{\rho}. \tag{2.19}$$

The new variable $\hat{\nu}$ is obtained by solving one extra transport equation in conjunction with the mean flow equations, where the conservative, convective, viscous, and source terms are given by:

$$\mathcal{U} = \hat{\nu}, \quad \vec{F}^c = \vec{v}\hat{\nu}, \quad \vec{F}^v = -\frac{\nu + \hat{\nu}}{\sigma}\nabla\hat{\nu}, \quad \vec{Q} = c_{b1}\hat{S}\hat{\nu} - c_{w1} f_w \left(\frac{\hat{\nu}}{d_S}\right)^2 + \frac{c_{b2}}{\sigma}|\nabla\hat{\nu}|^2, \tag{2.20}$$

where

$$\begin{aligned} \hat{S} &= |\vec{\omega}| + \frac{\hat{\nu}}{\kappa^2 d_S^2} f_{v2}, \qquad \vec{\omega} = \nabla \times \vec{v}, \qquad f_{v2} = 1 - \frac{\chi}{1 + \chi f_{v1}}, \\ f_w &= g\left[\frac{1 + c_{w3}^6}{g^6 + c_{w3}^6}\right]^{1/6}, \qquad g = r + c_{w2}(r^6 - r), \qquad r = \frac{\hat{\nu}}{\hat{S}\kappa^2 d_S^2} \end{aligned} \tag{2.21}$$

$\hat{S}$ is the production term, $\vec{\omega}$ is the fluid vorticity, d_S is the distance to the nearest wall. The closure constants for the model are:

$$\begin{aligned} \sigma &= 2/3, \qquad c_{b1} = 0.1355, \qquad c_{b2} = 0.622, \qquad \kappa = 0.41, \\ c_{w1} &= \frac{c_{b1}}{\kappa^2} + \frac{1 + c_{b2}}{\sigma}, \qquad c_{w2} = 0.3, \qquad c_{w3} = 2, \qquad c_{v1} = 7.1 \end{aligned} \tag{2.22}$$

On viscous walls, $\hat{\nu}$ is set to zero, corresponding to the absence of turbulent eddies very near to the wall.

2.2.2 Menter Shear-Stress-Transport Model

The Shear-Stress-Transport (SST) model [62] uses two equations to develop a turbulent viscosity value that will model the smaller eddies that are not being resolved through the use of the kinetic energy (k) and the specific dissipation (ω). This model is effectively a blend of the $k - \omega$ and the $k - \epsilon$ models, and the turbulent viscosity is defined as:

$$\mu_{tur} = \frac{\rho a_1 k}{max(a_1\omega, SF_2)} \tag{2.23}$$

where $S = \sqrt{2S_{ij}S_{ij}}$, and F_2 is the second blending function which is one for boundary layer flows and zero for free shear layers.

The new variables are obtained by solving two extra transport equations in conjunction with the mean flow equations. The conservative, convective, viscous, and source terms for the kinetic energy

portion of this model are:

$$\mathcal{U} = \rho k, \quad \vec{F}^c = \rho k \vec{v}, \quad \vec{F}^v = -(\mu_{dyn} + \sigma_k \mu_{tur})\nabla k, \\ \vec{Q} = \mathcal{P} - \beta^* \rho \omega k, \tag{2.24}$$

where $\mathcal{P}$ is the production term for the turbulent kinetic energy.

The conservative, convective, viscous, and source terms for the specific dissipation portion of this model are:

$$\mathcal{U} = \rho\omega, \quad \vec{F}^c = \rho k\vec{v}, \vec{F}^v = -(\mu_{dyn}+\sigma_\omega \mu_{tur})\nabla\omega, \quad \vec{Q} = \frac{\gamma}{\nu_t}\mathcal{P} - \beta^*\rho\omega^2 + 2(1-F_1)\frac{\rho\sigma_{\omega_2}}{\omega}\nabla k \nabla\omega \tag{2.25}$$

where F_1 is the first blending function which is one in the boundary layer flows and zero for free shear layers. The closure constants and the blending function model are detailed in the paper by Menter [62].

2.3 Selection of Numerical Tools

The numerical solution of the NS equations was performed using SU2. The SU2 suite is an open source compilation of C++ and Python based software for multi-physics simulation and design using unstructured meshes. This software solves the NS equations using a second-order finite volume approach[8, 41, 48, 97]. SU2 features a variety of numerical schemes which include Jameson-Schmidt-Turkel (JST), Roe, Advection Upstream Splitting Method (AUSM), and Lax-Friedrich; as well as turbulence models such as various version of SA, SST and Detached Eddy Simulation (DES) [69, 70, 19]. This suite's development started at the Aerospace Design Laboratory in the Aeronautics & Astronautics department at Stanford University. The technical capabilities, open source philosophy, geographical proximity, and the opportunity to join and interact with the development team made SU2 the ideal platform for this work.

To determine the capabilities of the available numerical schemes and turbulence models in SU2, a case study using circular and square cylinders was performed. These geometries where selected due to the geometrical and aerodynamic similarities that they have with respect to each other, as well as with the Ground Transportation System (GTS) model. The main reason for having both, square and circular cylinders, is to understand the strengths and weaknesses of the computational tools when dealing with separation from smooth surfaces, as in the circular cylinder, as well as with sharp corners, which are present in the square cylinder. The flow around both geometries at well studied conditions have been simulated and properties including the drag coefficient, separation angle, recirculation region, and Strouhal number have been computed. A comparison with experimental data and other numerical results is used to determine the best combination of computational tools for highly separated flows.

2.3.1 Circular Cylinder

The computational grid for the circular cylinder is composed of 45,766 elements and 25,869 points. The cylinder diameter (D) is one and is used as the characteristic length. The grid is 40D x 20D in the stream-wise and span-wise directions respectively, and the cylinder is positioned at x = 10D. The dimensions of the far-field and the positioning of the cylinder are a modification of the computational domain used by Catalano *et al.* [12] in 2003. The computational grid is hybrid in nature with a mixture of structured elements near the walls, to better resolve the boundary layer, and unstructured elements to generate a fast growing mesh to the far-field. Figure 2.1 shows the mesh.

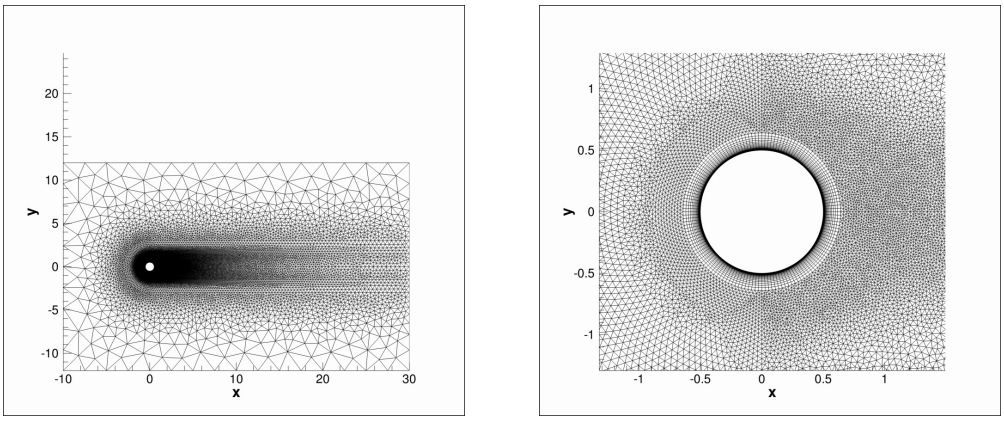

(a) Full domain. (b) Near-field.

Figure 2.1: Computational grid for the circular cylinder.

For the analysis of this geometry, two second-order numerical schemes have been used for computing the convective fluxes: the JST [42] scheme, and the Roe [78] scheme in conjunction with the Venkatakrishnan limiter [94]. These numerical schemes have been used in combination with the SA [88] and SST [62] turbulence models. These simulations have been run at a Reynolds number of 100,000 and at a Mach number of 0.1, using a second order numerical scheme and an upwind first-order turbulence model. A dual time stepping scheme has been used for time integration [40], using a $dt = 0.0015s$. This time step was selected to guarantee vortex shedding when using the SA model, as this requires a finer time stencil in order to simulate the flow past a bluff body without a clearly specified separation point.

The results presented in Tables 2.1 and 2.2 are obtained by averaging the flow behavior over 5 periods. The flow visualizations for both the circular and square cylinders shown in Figures 2.2 and 2.4 are in good agreement with the experimental and computational results which have been compared.

Contribution	***Model***	***Re***	$\overline{C_d}$	S_t	θ_s	C_b
Gowen et al., 1953	*Experiments* $M = 0.4$	$100,000$	$1.18 - 1.27$	–	$94°$	-1.25
Roshko, 1961	*Experiments* $M = 0.25$	$100,000$	1.2	$0.19 - 0.23$	$85°$	-1.13
Achenbach, 1968	*Experiments* $M = 0.1$	$100,000$	$1.0 - 1.2$	–	$78°$	-1.17
Present JST	$URANS - SA$	$100,000$	0.7912	0.2708	$86.85°$	-0.8705
Present JST	$\boldsymbol{URANS - SST}$	$\mathbf{100,000}$	$\mathbf{0.9827}$	$\mathbf{0.2576}$	$\mathbf{84.84°}$	$\mathbf{-1.0729}$
Present ROE	$URANS - SA$	$100,000$	0.8418	0.2760	$90.23°$	-0.9073
Present ROE	$URANS - SST$	$100,000$	0.8807	0.2616	$90.64°$	-1.0208

Table 2.1: Results for the circular cylinder M = 0.1. $\overline{C_d}$ is the time-averaged drag coefficient, Re is the Reynolds number, S_t is the Strouhal number, θ_s is the average angle at which it separates, and C_b is the pressure coefficient inside the wake of the cylinder.

The obtained results for the circular cylinder from the various cases examined have been summarized in Table 2.1 alongside the experimental results from Gowen *et al.* [29] in 1953, Roshko [80] in 1961, and Achenbach [1] in 1968.

As expected, the flow past a circular cylinder exhibits separation and periodic vortex shedding. The frequency at which the vortices are being shed is represented by the Strouhal number, which is in good agreement between the combination of computational tools. The computationally obtained Strouhal number is higher than the experimental results by Roshko [80], and this is in part due to the difference in Mach numbers. The numerical simulations are at the same Reynolds numbers as the results published by Roshko [80] and Gowen *et al.* [29] but a lower Mach number was selected to better represent the flow past a heavy vehicle. These results are included in Table 2.1 since they provide good insight on the results obtained, and are a good metric for quantifying the effect that Mach number has on the flow past bluff bodies.

The average drag coefficient obtained by the combination of JST [42] and SST [62] is in good agreement with the experimental data presented by Achenbach in 1968 [1], which is particularly relevant to this study since the experiments were performed at the same Reynolds and Mach numbers. All other combinations of numerical schemes and turbulence models underpredict the drag coefficient. The separation point and base pressure coefficient are not well predicted by numerical simulations in general. This is to be expected since the available RANS models have not been generated with separated flow applications in mind and have difficulty predicting separation. Even-though the results are not in full agreement with the experimental data, it can be seen that the combination of JST [42] and SST [62] most closely agree with the experimental values. The results obtained for the simulation of the flow past a circular cylinder using this combination are presented in Figure 2.2.

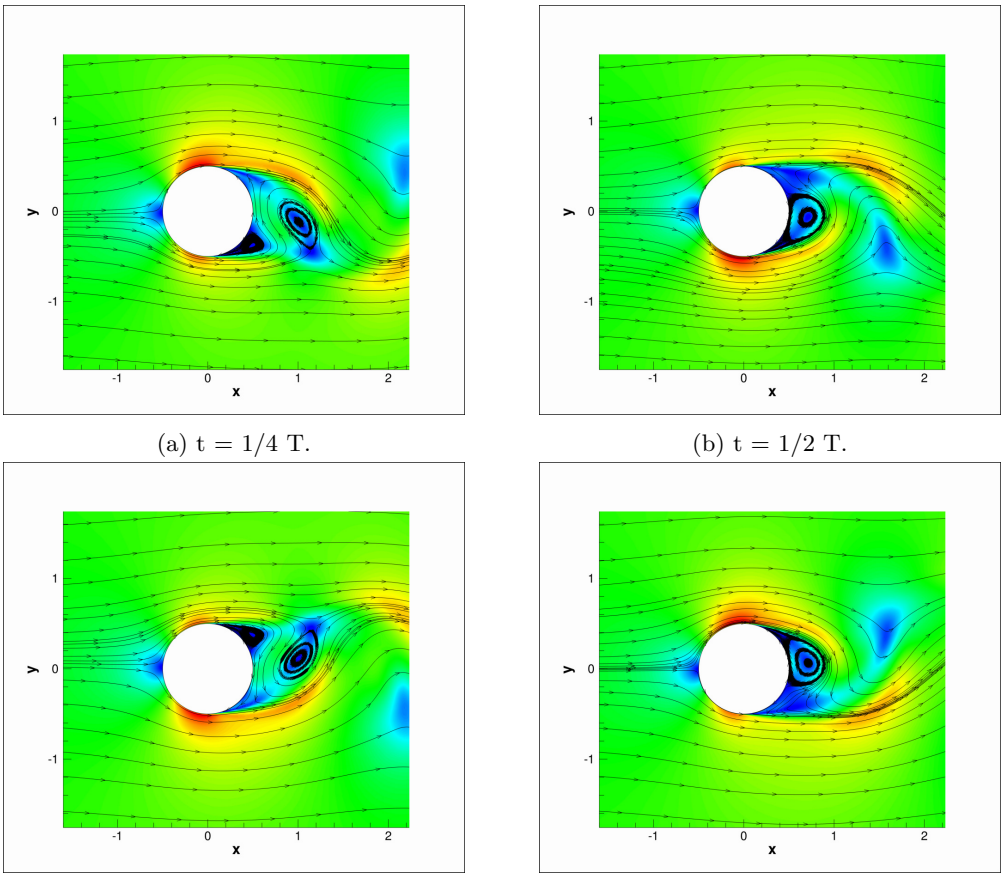

(a) t = 1/4 T.

(b) t = 1/2 T.

(c) t = 3/4 T.

(d) t = T.

Figure 2.2: Mach number contours of the time history of the streamlines past a circular cylinder. T represents one shedding period.

2.3.2 Square Cylinder

The computational grid used to simulate the flow over a square cylinder is composed of 44,261 elements and 25,226 points. The height (h) is one, and it is used as the characteristic length of the square cylinder. The size of the mesh is 20h x 14h in the stream-wise and span-wise directions respectively, as recommended by Rodi *et al.* [77] in 1997 and Iaccarino *et al.* [39] in 2003. The square cylinder is located at x = 5h. The computational grid is hybrid in nature with a mixture of structured elements near the walls, to better resolve the boundary layer, and unstructured elements, to generate a fast growing mesh to the far-field. Figure 2.3 shows the mesh.

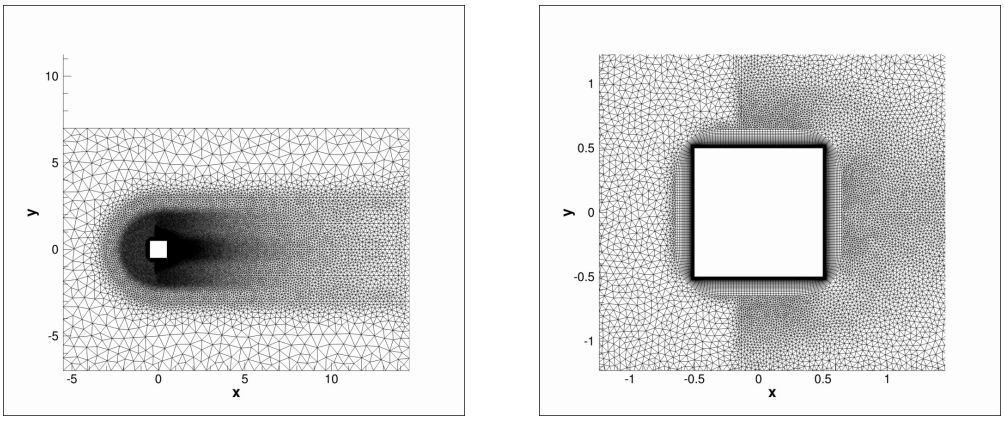

(a) Full domain. (b) Near-field.

Figure 2.3: Computational grid for the square cylinder.

The numerical schemes used for the simulation of the flow over the square cylinder are, once again, JST [42] and Roe [78] combined with the SA [88] and SST [62] turbulence models, as previously described. The square cylinder has been simulated at a Reynolds number of 22,000 and a Mach number of 0.1. A dual time stepping scheme has been used for the time integration [40], using a $dt = 0.0015s$.

The simulation results for the square cylinder have been compared with experimental data from Lyn *et al.* [51], Lee [46], and Vickery [96], as well as with computational results obtained from Rodi *et al.* [77], and Iaccarino *et al.* [39]. The results can be seen in Table 2.2.

As expected, the flow past the square cylinder exhibits periodic vortex shedding in its wake. The frequency at which the cylinder's wake is oscillating is represented by the Strouhal number, which overall is in good agreement with the experimental and computational results found in the literature. This is believed to be the result of the separation point being located at the sharp corners of the square cylinder, which is a major difference from the circular cylinder case.

Looking carefully at all the cases, it can be seen that, just as in the circular cylinder case, the combination of computational tools that agrees most closely with the experimental and Large

Contribution	***Model***	x_r/h	$\overline{C_d}$	$\widetilde{c_d}$	$\widetilde{c_l}$	S_t
Lyn et al., 1995	*Experiments*	1.38	2.1	–	–	0.132
Lee et al., 1975	*Experiments*	–	2.05	$0.16 - 0.23$	–	–
Vickery, 1966	*Experiments*	–	2.05	$0.1 - 0.2$	$0.68 - 1.32$	–
Rodi et al., 1997	*LES*	1.32	2.2	0.14	1.01	0.13
Rodi et al., 1997	*RANS* $k-\omega$	1.25	2.004	–	–	0.143
Iaccarino et al., 2003	*URANS* v^2-f	1.45	2.22	0.056	1.83	0.141
Present JST	$URANS - SA$	1.30	2.3760	0.04679	2.4907	0.1382
Present JST	$\boldsymbol{URANS - SST}$	**1.31**	**2.2096**	**0.005471**	**1.6835**	**0.1315**
Present ROE	$URANS - SA$	0.89	2.4609	0.04979	2.4680	0.1419
Present ROE	$URANS - SST$	1.03	2.2759	0.01934	1.9473	0.1467

Table 2.2: Results for the square cylinder at Re = 22,000 and M = 0.1. x_r/h is the recirculation length, $\overline{C_d}$ is the time averaged drag coefficient, $\widetilde{c_d}$ is the drag coefficient variance, $\widetilde{c_l}$ is the lift coefficient variance, and S_t is the Strouhal number.

Eddy Simulation (LES) results is the combination of JST [42] and SST [62]. One of the most important features that has to be analyzed for a square cylinder is the recirculation region behind the cylinder. The recirculation region is formed due to separation, and the value measured ranges widely depending on the selection of computational tools. The general trend with the computational results is to underpredict the length of the recirculation region. The combination of JST [42] and SST [62] simulates the recirculation region with comparable accuracy to the LES results presented by Rodi *et al.* in 1997 [77], and the results are not far from the experimental values presented by Lyn *et al.* in 1995 [51]. The drag coefficient and lift coefficient variance are overestimated by these simulations, while the drag coefficient fluctuations are underestimated with respect to the experimental data. A plausible explanation for this disagreement is the lack of three-dimensional effects that are believed to have a great influence in the lift coefficient fluctuations [39]. The results obtained for the simulation of the flow past a square cylinder using the combination of JST [42] - SST [62] are presented in Figure 2.4.

The results obtained from the circular and square cylinders show that, although there are some limitations on the accuracy to which these computational tools are able to simulate separated flows, the general trends for bluff body aerodynamics are captured, and the results are within an acceptable range for design purposes. The flow features that proved to be the most challenging for the computational tools were: separation angle on the circular cylinder and the recirculation region behind the square cylinder. Based on the overall behavior of the numerical solutions, the combination of JST [42] and SST [62] has proven the most capable for predicting the flow past bluff bodies, and therefore it is the chosen combination for studying the aerodynamic profile of the GTS model.

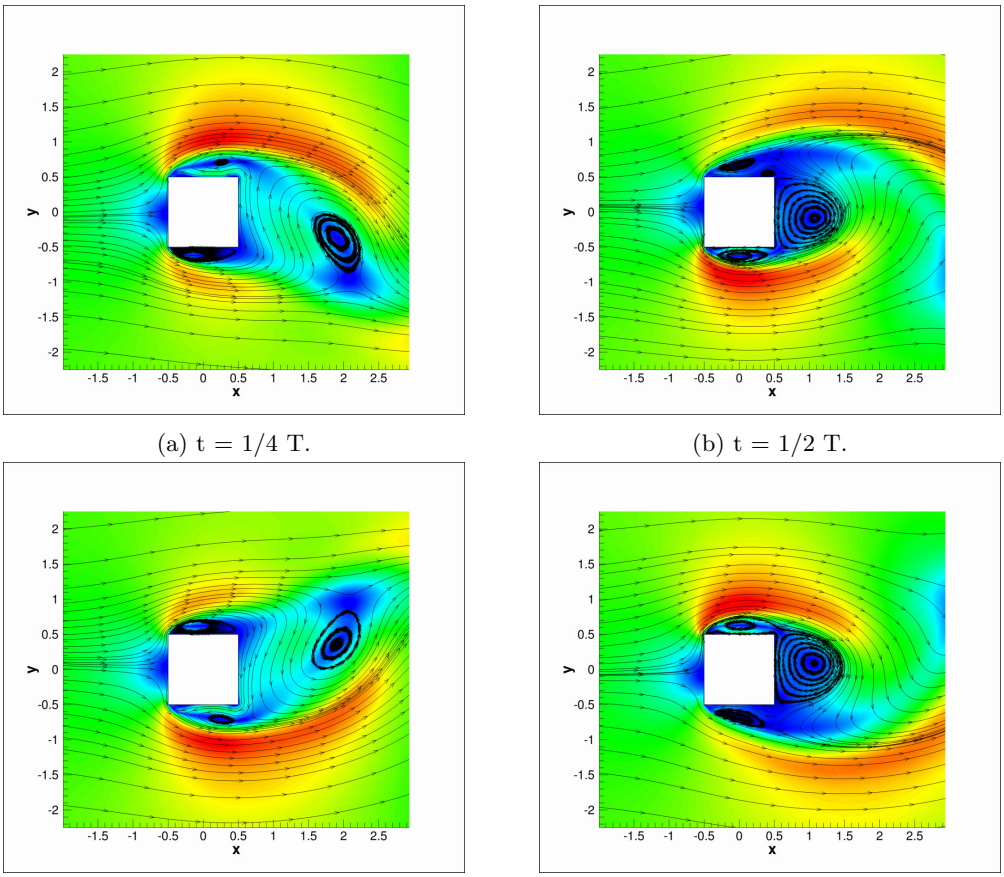

(a) t = 1/4 T.

(b) t = 1/2 T.

(c) t = 3/4 T.

(d) t = T.

Figure 2.4: Mach number contours of the time history of the streamlines past a square cylinder. T represents one shedding period.

Chapter 3

Two-Dimensional Studies of Active Flow Control for Drag Reduction

3.1 Physical Model

3.1.1 Geometrical Model

In order to identify the dominant aerodynamic features that characterize separated flows, and the influence Active Flow Control (AFC) has on the presence of viscous pressure drag, a clean model of a heavy vehicle is required [93]. Heavy vehicles have a variety of features that contribute towards flow separation, such as mirrors, antennas, gaps, mud flaps, etc. and to eliminate the effect that these have, a customized version of the Ground Transportation System (GTS) model was used. The Customized Ground Transportation System (CGTS) model removes all the detailed features including the tractor-trailer gap, and the height difference. This geometrical model effectively combines both the tractor and the trailer into a single simplified bluff body that has a semicircular leading shape and ends in a sharp straight cut in the back. A 6.5% scale vehicle, similar to the one used by Englar [22, 23], was used for this analysis. In addition to the base model in Figure 3.1, a model which includes Coanda jets in all four corners of the trailing edge was generated and is shown in Figure 3.2.

In order to reduce the computational cost of exploring the effects of manipulating the Coanda surface geometry and jet blowing strength, a two-dimensional model capable of representing the prominent flow features was introduced. The principal effects of AFC that this section aims to analyze are drag reduction, which leads to reduced power consumption, as well as lateral stability, which is a consequence of wake stabilization and vortex shedding reduction. For this purpose, the top-view of the CGTS model was chosen. The two-dimensional geometries are shown in Figure 3.3.

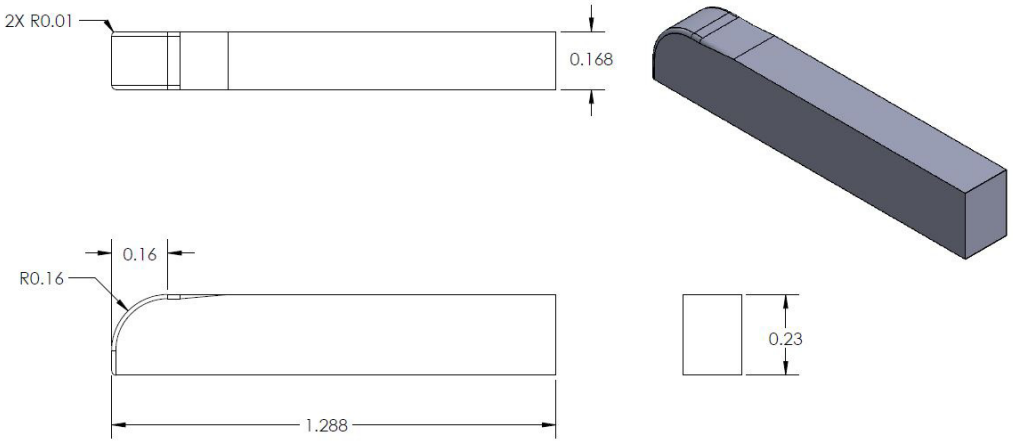

Figure 3.1: Baseline three-dimensional CGTS model - Scale 6.5%. All dimensions in meters.

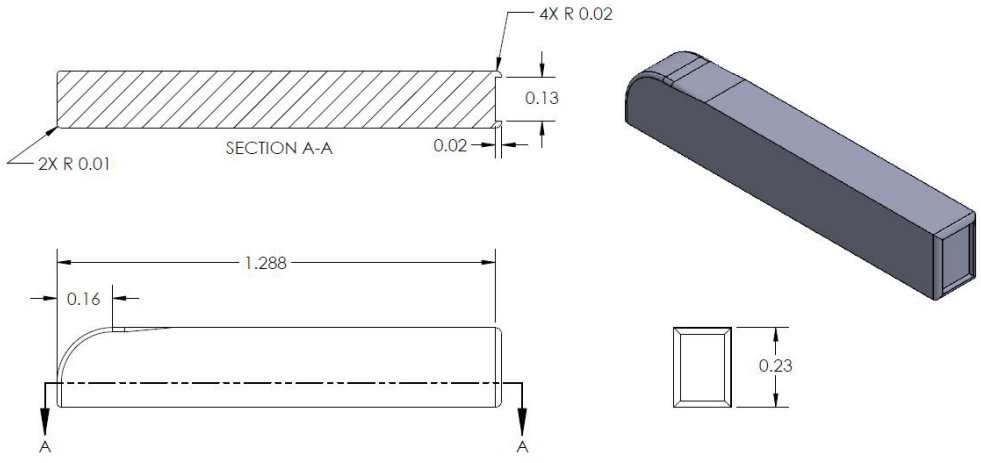

Figure 3.2: Three-dimensional CGTS model with Coanda Jets in the trailing edge - Scale 6.5%. All dimensions in meters.

(a) Top view of the base CGTS model.

(b) Top view of the CGTS model with Coanda jets at the trailing edge.

Figure 3.3: Two-dimensional CGTS models - Scale 6.5%. All dimensions in meters.

Although the flow around a ground vehicle has a variety of three-dimensional effects, this two-dimensional approach provides an avenue for the study and understanding of the aerodynamic changes produced by the flow control system. To simulate jet flow injection, a plenum-jet design was included as part of the geometrical model. The geometry representing the plenum-jet was developed from the Englar airfoil [25]. In general, the chosen plenum shape enhances the strain behavior of the flow, which is achieved by generating two standing vortices that guide the flow towards the Coanda surface. The path taken by the flow, and its interaction with the internal vortices, reduce the wall effect and allows for a cleaner flow, which helps prevent premature boundary layer separation. Figure 3.4 shows the Coanda jet geometry and the described flow features.

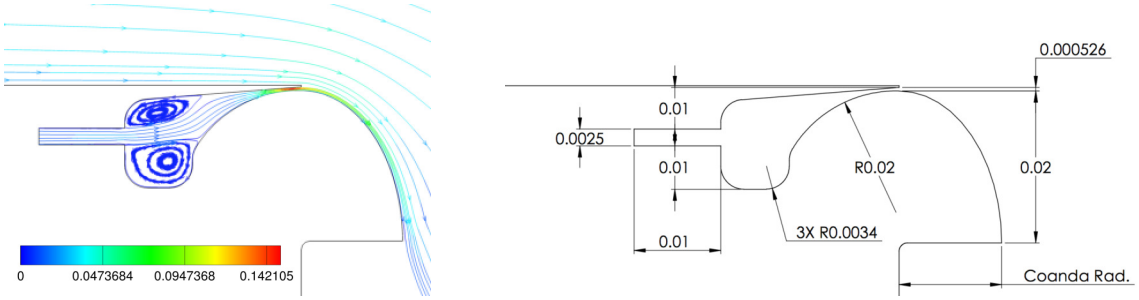

(a) Flow inside the Coanda jet plenum, streamlines colored by Mach number.

(b) Plenum-jet geometry - Scale 6.5%. All dimensions in meters.

Figure 3.4: Coanda jet model and flow features.

3.1.2 Flow Conditions

The CGTS model was analyzed using standard air threated as a calorically perfect ideal gas at Standard Temperature and Pressure (STP) conditions. The free-stream velocity was chosen to match the vehicle's highway cruise speed of 31.3 m/s (70 mph), which translates to a Mach number of 0.09195 and Reynolds numbers, as a function of the GTS model length (Lc) and width (W), of 2.759 million and 359,900 respectively. The power required to overcome the aerodynamic drag is:

$$P_{aero} = D * U_{\infty} \tag{3.1}$$

where D is the aerodynamic drag and U_∞ is the free-stream velocity. The power required to energize each Coanda jet is the compressor power:

$$P_{comp} = \frac{\dot{m}_e * c_p * (T_f - T_i)}{\eta} \tag{3.2}$$

which has been calculated using a thermodynamic compressor model. The mass flow rate through the jet is $\dot{m}_e$, c_p is the constant pressure specific heat, T_f is the plenum fluid temperature which was set to 477.594 K to maximize the jet momentum [22, 23], T_i is the fluid temperature before entering the compressor and η is the compressor's isentropic efficiency which has been set to 90%.

To better characterize the jet strength, vehicle drag, power consumption, lateral forces, and vortex shedding frequency for this two-dimensional system; non-dimensional coefficients have been defined as follows:

$$C_{Pow} = \frac{P_{aero} + 2 * P_{comp}}{q * U_\infty * W}, \qquad C_\mu = \frac{\dot{m}_e * V_e}{q * W}, \qquad St = \frac{f * W}{U_\infty} \tag{3.3}$$

$$C_D = \frac{D}{q * W}, \qquad C_{LF} = \frac{LF}{q * W} \tag{3.4}$$

where C_{Pow} is the power coefficient, q is the dynamic pressure calculated as $\frac{1}{2}\rho_\infty U_\infty^2$, ρ_∞ is the free stream density, W is the width of the base CGTS model, C_μ is the momentum coefficient, V_e is the flow velocity at the jet's exit, St is the Strouhal number, f is the vortex shedding frequency, C_D is the drag coefficient, C_{LF} is the lateral force coefficient, and LF is the lateral force.

3.2 Computational Model

To simulate the flow around the two-dimensional base and enhanced vehicle models, the compressible solver in SU2 [69, 70, 19] was selected. The numerical scheme and turbulence model chosen for these simulations, through the process described in Chapter 2, were the second-order Jameson-Schmidt-Turkel (JST) [42] numerical scheme combined with the Shear-Stress-Transport (SST) [62] turbulence model [55]. The viscous terms were computed using the weighted least squares method and time accurate integration was achieved with a second-order backward difference dual time stepping approach [40]. To better model the periodicity of the flow, a physical time step of 500 μs was chosen, representing each period by using between 60 to 120 points, depending on the shedding frequency of the wake. To maintain the required time integration accuracy, three orders of magnitude of pseudo-time convergence were used at each physical time step.

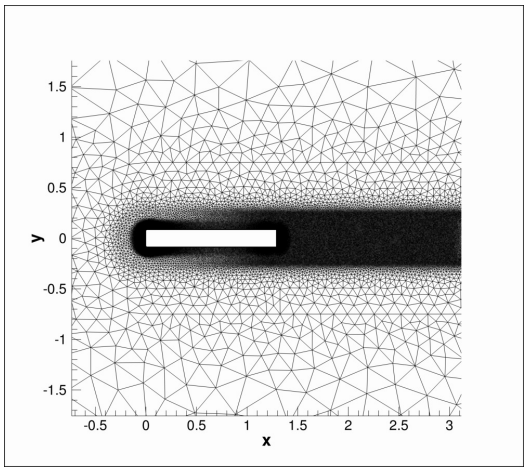

(a) Base CGTS mesh including a wake refinement region.

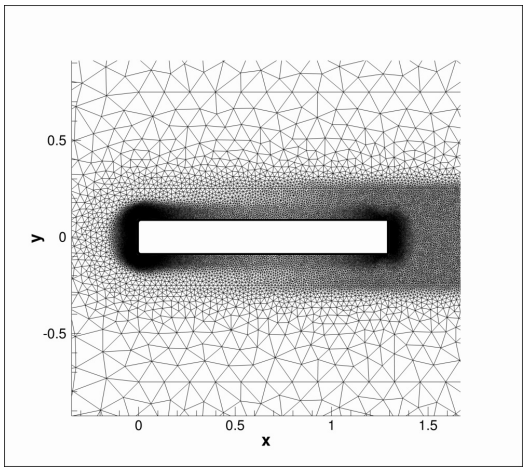

(b) Base CGTS mesh near-field.

Figure 3.5: Computational grid for the two-dimensional base CGTS model.

The geometry was represented by the use of two-dimensional domains which were discretized using a hybrid mesh, which consists of a structured mesh near the walls, to better capture the boundary layer behavior, and an unstructured mesh towards the far-field, for a more aggressive growth rate while keeping a healthy aspect ratio of the elements. To properly resolve the boundary layer a $y+$ of 0.8 was used. The meshes used, shown in Figures 3.5 and 3.6, are $15L_c$ in length and $11L_c$ in width which, in addition to the use of characteristic far-field boundary conditions, has been used to prevent pressure wave reflections.

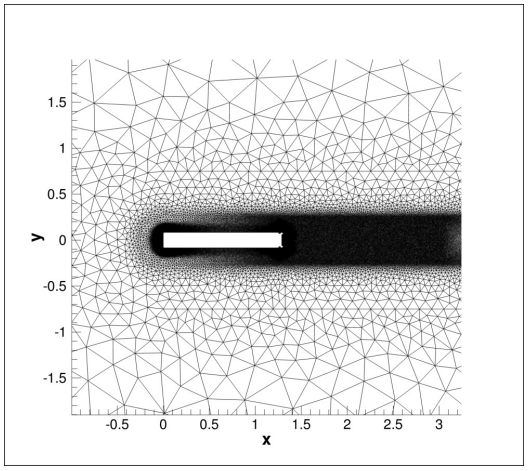

(a) Enhanced CGTS mesh including a wake refinement region.

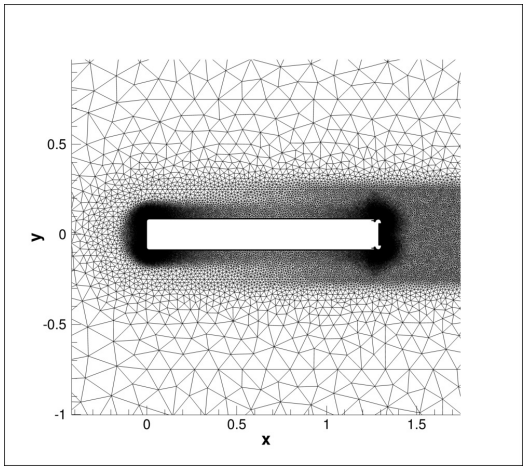

(b) Enhanced CGTS mesh near-field.

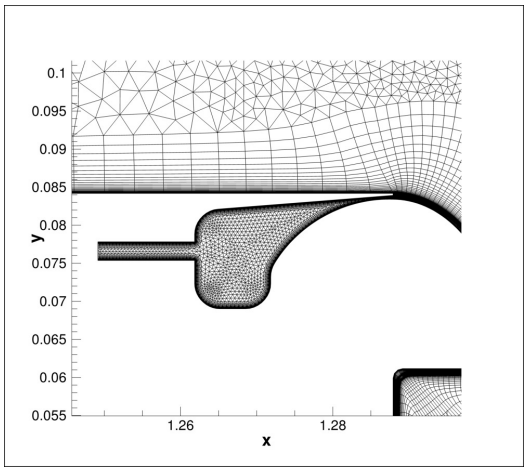

(c) Computational grid of the plenum-jet region.

Figure 3.6: Computational grid for the two-dimensional enhanced CGTS model.

The mesh used to represent the base CGTS model has $88,275$ cells and $52,915$ points. The one used to represent the enhanced CGTS model, which includes the Coanda jets at the trailing edge, has $140,259$ cells and $89,572$ points. The radical increase in mesh size is due to the addition of the jets and the resolution required to model the plenum.

3.3 Design Optimization

In order to properly design AFC systems capable of significantly reducing harmful emissions and vehicle energy consumption, its important to understand the variables that control the system. In this case the jet injection strength and Coanda geometry were identified as the relevant design parameters. Through the use of surrogate models, the effects induced by changing these variables were studied. This approach afforded the opportunity to study its design space, while maintaining computational cost to a minimum.

The strategy used for this design space exploration was focused on two stages. The first stage used only the jet strength to modify the aerodynamic profile of the CGTS, and determined the momentum coefficient (C_μ) working range, which represents the jet strength. The second stage took into consideration this range and integrated Coanda geometry changes into the optimization process to find an optimum AFC system.

3.3.1 Jet Strength Optimization

This stage focuses on the amount of flow delivered by the Coanda jets, and the energy that these carry, to minimize the drag of the GTS model. The flow delivered by the jets is quantified by the

momentum coefficient (C_μ), and the aerodynamic drag on the GTS model is described by the drag coefficient (C_D).

To optimize the sampling of C_μ, a Gaussian Process Regression (GPR) model [26] was used. This approach is used to generate a surrogate model of the system by probabilistically fitting a curve through the points evaluated. Additionally, this technique provides an uncertainty metric, represented by a covariance function [26] which is used to guide the selection of future function evaluations. For this study, a squared-exponential kernel was used as the covariance function, which is a representation of the standard deviation.

To better guide the prediction, an "expected improvement" [26] function was implemented. This prediction algorithm works by generating a modified standard deviation distribution. This metric was computed by biasing the general standard deviation distribution towards the local minimum of the surrogate model, providing the location at which the minimum is most likely to be found. Each function evaluation brings information to the optimization and modifies the surrogate model increasing it's accuracy. Once the surrogate model's uncertainty has reduced significantly, due to the insertion of function evaluations, the surrogate model is used to determine the minimum and the function is evaluated at that location one last time for validation.

The maximum and minimum blowing coefficient for this study were selected to be C_μ=0.0 and C_μ=0.0501, by examining Englar's work in 2001 [23]. The approach chosen to maximize the use of the available computational time was to start by evaluating the cost function at the bounds and at the center ($C_\mu = 0.0251$). Additional sampling of the domain took place and a minimum was found and confirmed after six function evaluations. The outlined process used to create the surrogate model, and find the minimum drag coefficient is show in Figure 3.7.

Results

To quantify the aerodynamic improvements obtained by using Coanda jets in the back of the GTS, it was necessary to generate a baseline by simulating the flow over the two-dimensional GTS base model. As expected, the flow over the base GTS model exhibits separation, vortex shedding and a periodic turbulent wake. The flow features can be seen in Figure 3.8. After introducing the Coanda geometry in the tailing edge of the GTS model, a reduction in drag is achieved. This improvement is due exclusively to the geometrical change in the trailing edge of the GTS model. The addition of the Coanda surfaces to the back of the model allows the flow to better negotiate the sharp corners and stay attached longer. This effect can be seen by comparing the flow features in Figures 3.8 and 3.9.

Although the flow stays attached longer with the introduction of the Coanda surfaces alone, it can be seen that it continues to separate prematurely. Air injection through this AFC system introduces high-momentum air to the Coanda surfaces and helps the incoming air negotiate the back corners and stay attached longer. The function evaluations used to sample the design space and

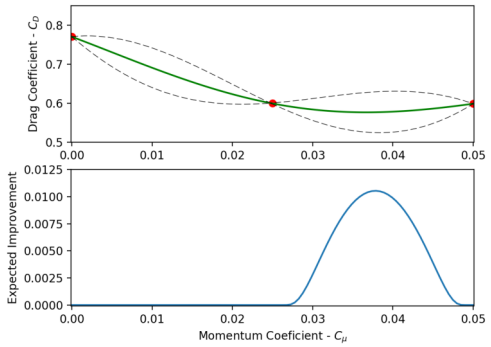

(a) Three function evaluations.

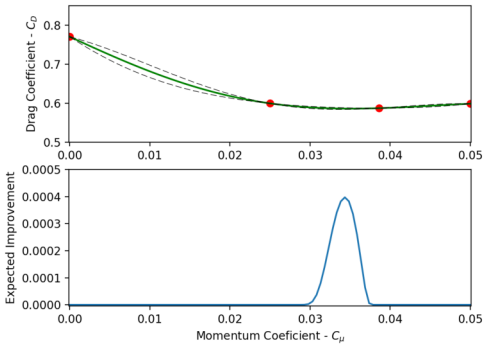

(b) Four function evaluations.

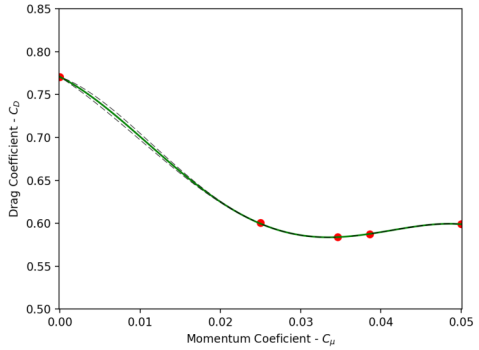

(c) Five function evaluations.

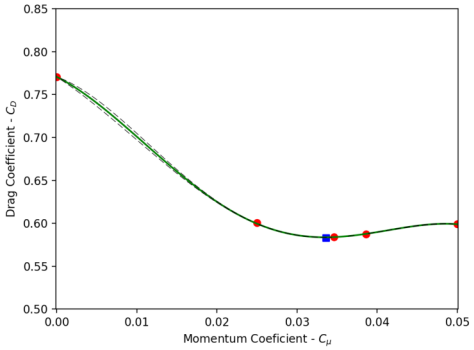

(d) Six function evaluations, including the minimum depicted with a square marker.

Figure 3.7: Process used to refine the surrogate model for the drag coefficient C_D. The dashed lines represent the 95% certainty limits. (a) shows the surrogate model developed by using only three function evaluations and the suggested location for the next function evaluation by the expected improvement function. (b) shows the improved model obtained by using four function evaluations and the suggested next function evaluation location. (c) shows the surrogate model generated using five function evaluations. (d) Shows the surrogate model generated after evaluating the predicted minimum using the surrogate model shown in (c).

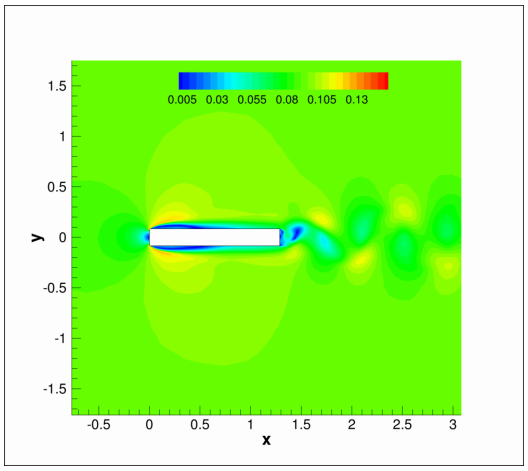

(a) Base GTS model.

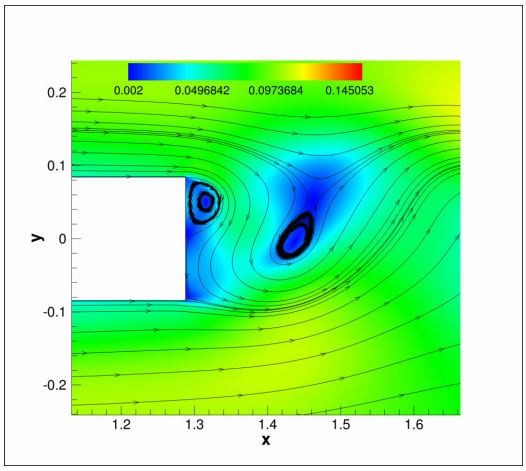

(b) Trailing edge of the base GTS model.

Figure 3.8: Mach number contours of the base GTS model.

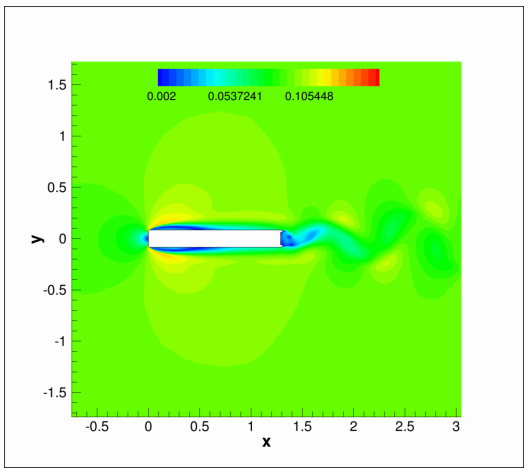

(a) Enhanced GTS model.

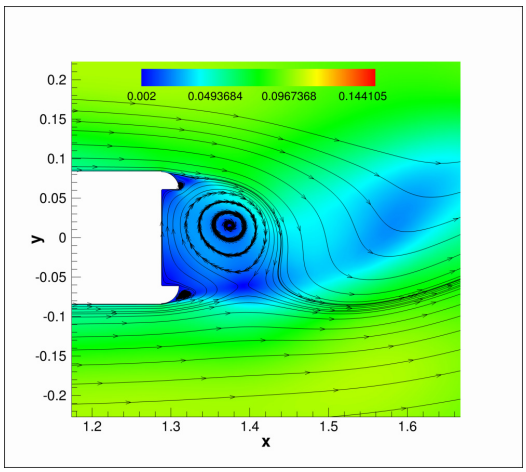

(b) Trailing edge of the enhanced GTS model.

Figure 3.9: Mach number contours of the enhanced GTS model without jet injection.

build the surrogate model have been summarized in Table 3.1.

C_μ	*Plenum Pressure (Pa)*	$\overline{C_D}$	$\overline{C_{Pow}}$	$\widetilde{c_D}$	$\widetilde{c_{LF}}$	S_t
–	–	1.0324	1.0324	$9.310E-05$	$6.97E-02$	0.1801
0.0000	101325	0.7707	0.7707	$2.860E-05$	$2.86E-02$	0.1737
0.0251	104070	0.6005	0.6269	$1.190E-07$	$1.13E-03$	0.1823
0.0336	**105022**	**0.5830**	**0.6276**	$\mathbf{4.31E-08}$	$\mathbf{6.65E-04}$	**0.1354**
0.0346	105134	0.5838	0.6300	$5.80E-08$	$7.10E-04$	0.1337
0.0386	105582	0.5874	0.6430	$1.480E-07$	$9.36E-04$	0.1309
0.0501	106870	0.5989	0.6841	$7.940E-07$	$2.10E-03$	0.1345

Table 3.1: Results for the GTS model and the enhanced GTS model injecting flow through Coanda jets in the trailing end at momentum coefficients ranging from 0.0 to 0.0501. C_μ is the jet momentum coefficient, $\overline{C_D}$ is the time averaged drag coefficient, $\overline{C_{Pow}}$ is the time averaged power coefficient, $\widetilde{c_D}$ is the drag coefficient variance, $\widetilde{c_{LF}}$ is the lateral force coefficient variance, and S_t is the Strouhal number.

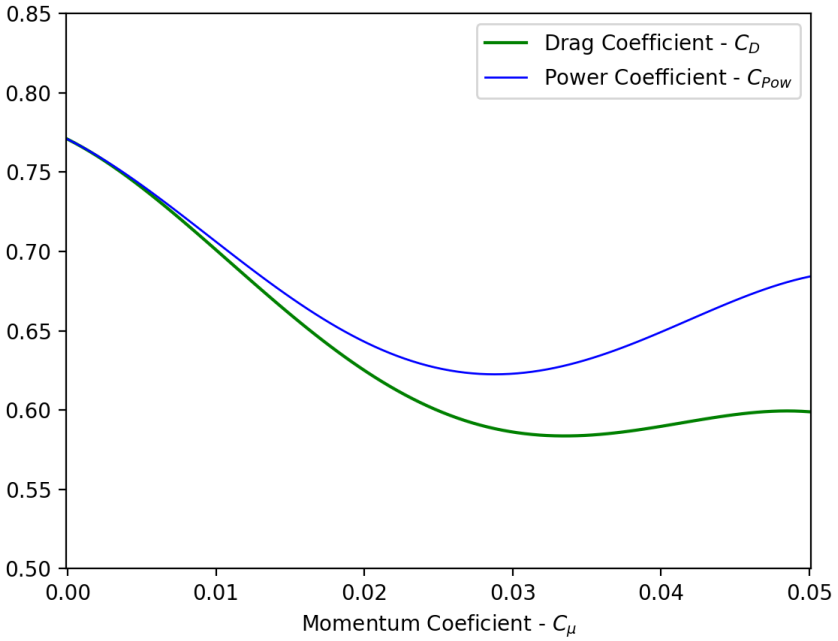

Figure 3.10: Surrogate models for the drag and power coefficients as a function of momentum coefficient.

In addition to a surrogate model to represent the drag as a function of the jet injection strength,

a surrogate model for power consumption was generated using a simple thermodynamic compressor model with an isotropic efficiency of 90%, as presented in Equation 3.3. This approach allowed for the quantification of the required energy to operate the jets. Figure 3.10 shows both the drag and power coefficients, where the required power is defined as the energy required to overcome the drag of the GTS model plus the energy to power the jets.

Using a surrogate model to guide the design space exploration, and function evaluations to increase its accuracy when required, the minimum drag configuration for this system was found to be $C_D = 0.5830$ when $C_\mu = 0.0336$. The flow characteristics can be seen in Figure 3.11.

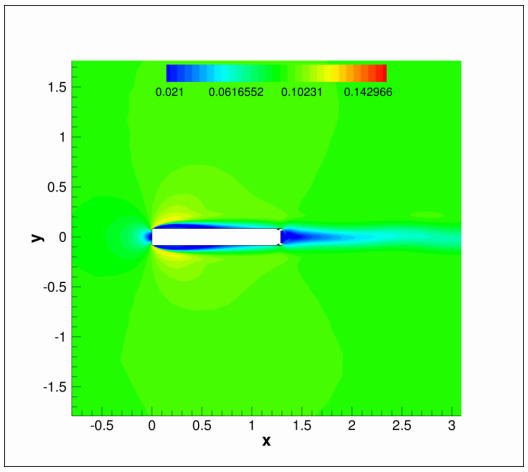

(a) Enhanced GTS model with activated jets.

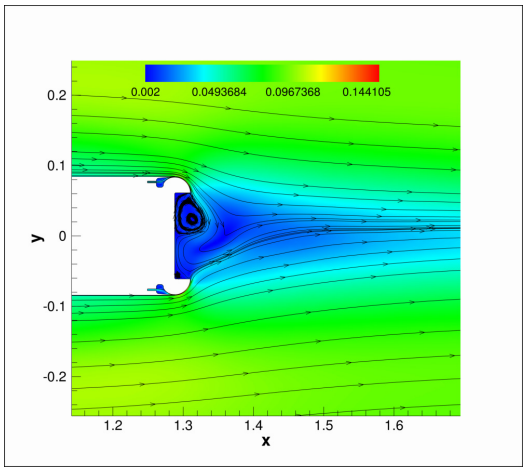

(b) Trailing edge of the enhanced GTS model with activated jets.

Figure 3.11: Mach number contours of the enhanced GTS model injecting air through the AFC system with $C_\mu = 0.0336$.

At this jet strength, not only is the drag coefficient minimized, but also the drag and lateral force coefficient variances. This reduction in the variance comes from a decrease in separation, which in turn dampens the oscillatory behavior of the wake. The Strouhal number(S_t), which in the case of the GTS model is a function of the vehicle's width, is significantly reduced from the base GTS to the enhanced GTS model operating at the optimum blowing configuration. As the momentum coefficient increases from the optimum position, the Strouhal number remains relatively unchanged– a phenomenon which can be attributed to the amount of separation allowed by the geometry of the Coanda surface and the location at which it is placed on the GTS model. The flow injection at the optimum configurations allows the flow to stay attached until the end of the Coanda surfaces, and any further increase in the momentum coefficient has adverse effects on the aerodynamics of the GTS model. The consequences of excess flow injected through the Coanda jet are an increase in the drag coefficient, as well as in the variance of drag and lateral force coefficients. These effects are to be expected, since the excess energy that the jet carries will start to disturb the flow in the wake.

The power coefficient, on the other hand, reaches its minimum ahead of the drag, as this takes into consideration the energy required to inject air. As the jet strength increases, the energy required for the system increases simultaneously, until it surpasses the energy savings from the aerodynamic improvements. In this study, the power response was generated to validate power saving capabilities of this AFC system, for which a minimum $C_{Pow} = 0.6225$ was achieved at $C_\mu = 0.02879$, validating the use of AFC systems for drag and power optimization.

3.3.2 Full System Optimization

The second stage of this two-dimensional study introduces the variation of the Coanda geometry in addition to the jet strength. Although the drag is monitored in this section, particular emphasis is placed in optimizing for power consumption, represented by the power coefficient (C_{Pow}). This metric was selected as a surrogate for fuel consumption, as fuel efficiency improvement is a more tangible objective for the trucking industry, and drag is just a part of the calculation.

The momentum coefficient(C_μ) was bounded between 0.00 and 0.05, as it was shown in the first stage of this study, shown in Section 3.3.1. This C_μ range provides the sufficient bandwidth to study the changes in drag and power consumption caused by the use of the AFC system. The momentum coefficient was controlled by varying the plenum pressure between $101,325$ and $106,029$ Pa. The Coanda radius has been modified through the use of Free Form Deformation (FFD) boxes, and the Coanda radius constraints were determined by visual inspection of the surrounding mesh quality after deformation. This technique maintains the overall mesh count and distribution constant making it ideal for design studies. The selected values for the Coanda radius ranged from 0.01 to 0.0286 m, which were controlled by varying the rightmost side of the FFD box from 0.00 to 0.05. The Coanda radius variation and FFD boxes are shown in Figure 3.12.

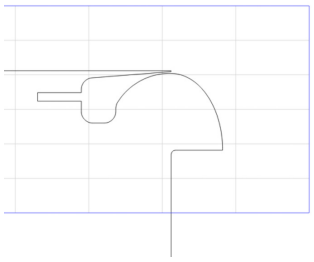

(a) Original Coanda jet geometry and FFD bounding box with control points at the intersection of the gray lines. Coanda Radius is 0.01 m.

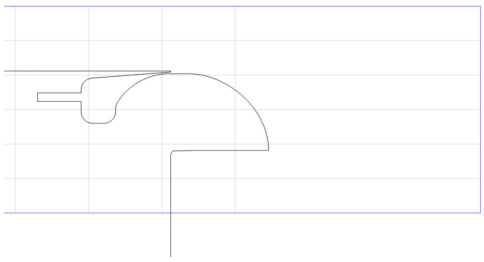

(b) Deformed Coanda jet geometry after displacement of the FFD control points. Coanda radius is 0.0283 m.

Figure 3.12: Coanda jet geometry deformation.

A FFD strategy has become a popular geometry parameterization technique for aerodynamic

shape design [84]. In FFD, an initial box encapsulating the object (rotor blade, wing, fuselage, Coanda surface, etc.) to be redesigned is parameterized as a Bézier solid. A set of control points are defined on the surface of the box, the number of which depends on the order of the chosen Bernstein polynomials. The solid box is parameterized by the following expression:

$$X(u,v,w) = \sum_{i,j,k=0}^{l,m,n} P_{i,j,k} B_i^l(u) B_j^m(v) B_k^n(w), \tag{3.5}$$

where u, v, $w \in [0, 1]$, and B^i is the Bernstein polynomial of order i. The Cartesian coordinates of the points on the surface of the object are then transformed into parametric coordinates within the Bézier box.

The control points of the box become design variables, as they control the shape of the solid, and thus the shape of the surface grid inside. The box enclosing the geometry is then deformed by modifying its control points, with all the points inside the box inheriting a smooth deformation. Once the deformation has been applied, the new Cartesian coordinates of the object of interest can be recovered by simply evaluating the mapping inherent in Equation 3.5. After the surface has been deformed, the geometry change propagates through the mesh which is deformed by solving the linear elasticity equations [18].

The design space was sampled 14 times with the use of a Latin-Hypercube [26] and the results obtained from these simulations were used to compute the length scales and surface fitting coefficient required for the proper generation of the C_{Pow} surrogate model using GPR [26]. To better match the expected behavior, the boundary values used to generate the C_{Pow} surrogate model were set to 0.82, which was determined based on the author's previous work [55] and verified by the simulations representing low momentum coefficient conditions. The GPR model and machine-learning toolbox used for this study were implemented by Lukaczyk [50].

Results

The surrogate model representing the power coefficient (C_{Pow}) can be seen in Figure 3.13. This surface is a low-resolution representation of the power required by the enhanced GTS model to maintain a constant speed while powering the Coanda jets. The data used to generate the surrogate model can be seen in Table 3.2. The generation of this response surface allows for a better understanding of the overall behavior of the vehicle under the effect of various Coanda radius and momentum coefficient (C_μ) values.

To understand the improvements brought by the introduction of AFC in the two-dimensional GTS model, the flow past the base GTS model has been simulated. The integrated forces and statistics have been added to Table 3.2 for comparison.

Case #	C_μ	*Coanda radius*	$\overline{C_D}$	$\widetilde{c_D}$	$\widetilde{c_{LF}}$	C_P	*St*
1	–	–	1.0235	$4.988e-04$	$4.342e-01$	1.0235	0.1743
2	0.0198	0.0277	0.7079	$1.289e-05$	$2.668e-02$	0.7583	0.1766
3	0.0136	0.0240	0.7322	$2.488e-05$	$4.242e-02$	0.7608	0.1743
4	0.0442	0.0259	0.6072	$1.968e-07$	$7.820e-04$	0.7744	0.0919
5	0.0096	0.0162	0.7431	$2.112e-05$	$5.951e-02$	0.7602	0.1721
6	0.0353	0.0202	0.6056	$1.979e-07$	$1.044e-03$	0.7251	0.0971
7	**0.0253**	**0.0160**	**0.5988**	$\mathbf{4.193e-08}$	$\mathbf{6.264e-04}$	**0.6713**	**0.1051**
8	0.0483	0.0208	0.6129	$2.284e-06$	$2.892e-03$	0.8037	0.1023
9	0.0289	0.0100	0.7162	$4.252e-07$	$2.250e-03$	0.8049	0.1013
10	0.0280	0.0240	0.7662	$2.155e-06$	$1.105e-02$	0.8506	0.1772
11	0.0430	0.0155	0.7774	$3.102e-06$	$4.815e-03$	0.9377	0.1123
12	0.0315	0.0248	0.7677	$1.371e-06$	$8.158e-03$	0.8683	0.1760
13	0.0010	0.0202	0.8243	$1.529e-04$	$1.428e-01$	0.8249	0.1694
14	0.0020	0.0257	0.8156	$1.054e-04$	$1.097e-01$	0.8172	0.1683
15	0.0220	0.0160	0.6492	$3.915e-06$	$1.766e-02$	0.7081	0.1732

Table 3.2: Results for the GTS model and the enhanced GTS model injecting flow through the Coanda jets in the trailing end at momentum coefficients ranging from 0.00 to 0.05 and Coanda radius from 0.01 to 0.0286 m. C_μ is the jet momentum coefficient, $\overline{C_D}$ is the time averaged drag coefficient, $\widetilde{c_D}$ is the drag coefficient variance, $\widetilde{c_{LF}}$ is the lateral force coefficient variance, C_P is the power coefficient, and St is the Strouhal number.

As expected, the aerodynamic profile of this geometry is characterized by a high level of separation, vortex shedding, and a large turbulent wake that generates a low-pressure region behind the vehicle. These flow features can be seen in Figures 3.14, 3.15 and 3.19.

The power coefficient required for the base GTS model to maintain a constant 31.3 m/s is 1.0235 and its vortex shedding occurs with a Strouhal number of 0.1743. Based on the results obtained from case seven, which is the lowest power consumption configuration found in this study, the drag generated by the presence of a turbulent wake in the two-dimensional GTS model represents over 40% of the total drag, and the effect of using Coanda jets translates into savings of over 30% in energy consumption.

The introduction of a surrogate model allows for the understanding and visualization of trends driven by the used variables, and will aid in the design of AFC drag reduction systems. Using the surrogate as a guide, it can be seen that as the momentum coefficient increases, the incoming flow is better able to negotiate the back corners of the vehicle. This aerodynamic enhancement results in wake size reduction, a decrease in shedding frequency, and an increase in pressure inside the wake, which in turn decreases drag. Since this drag reduction is a consequence of flow being injected through the Coanda jets, it is necessary to account not only for the reduction of power due to drag

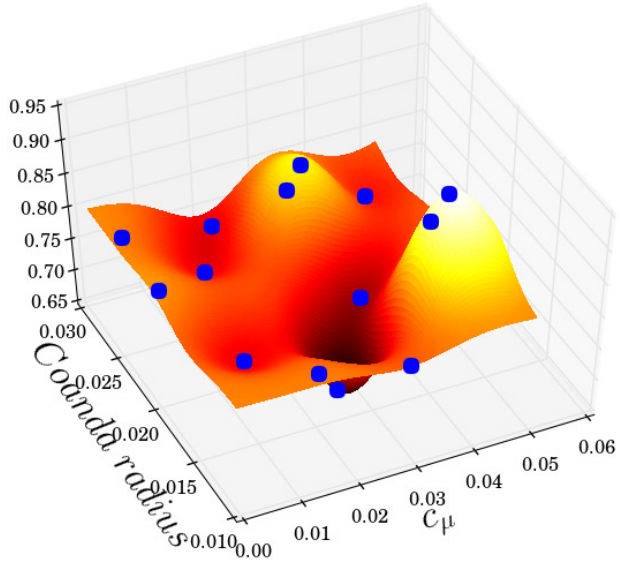

(a) Surrogate surface.

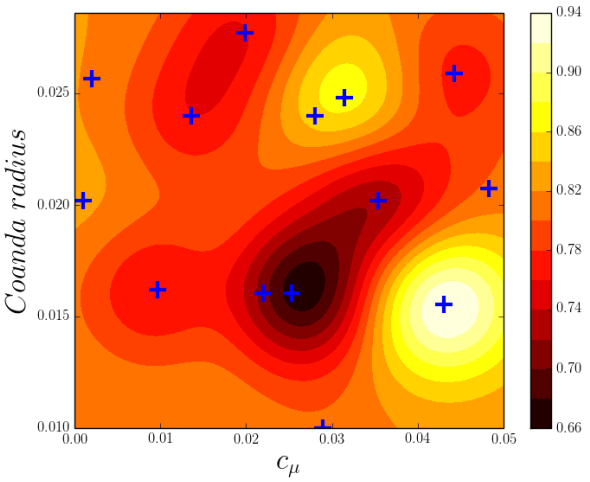

(b) Surrogate contour plot.

Figure 3.13: Surrogate model of the power coefficient (C_{Pow}) as a function of momentum coefficient (C_μ) and Coanda radius. The blue markers are the sampling locations used to generate the response surface.

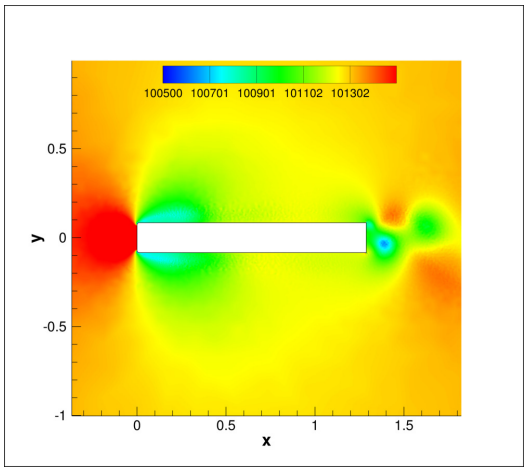

(a) Base GTS model.

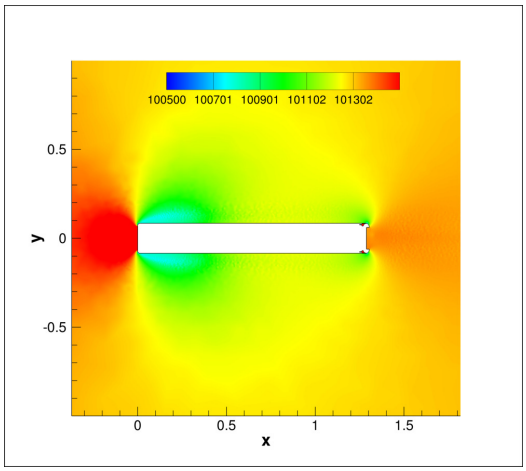

(b) Enhanced GTS model with a Coanda radius of 0.0160 m and C_μ of 0.0253. (Case 7)

Figure 3.14: Pressure contours of the GTS model. Pressure in Pascals.

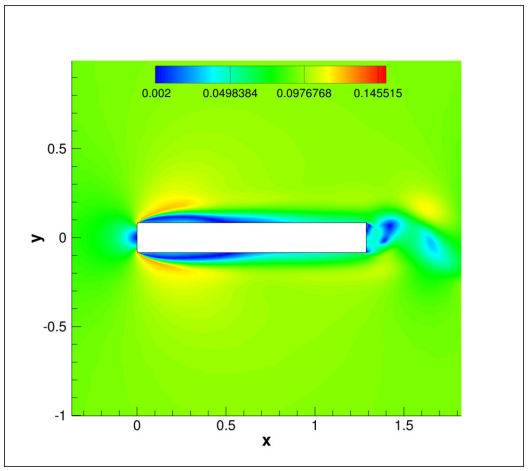

(a) Base GTS model.

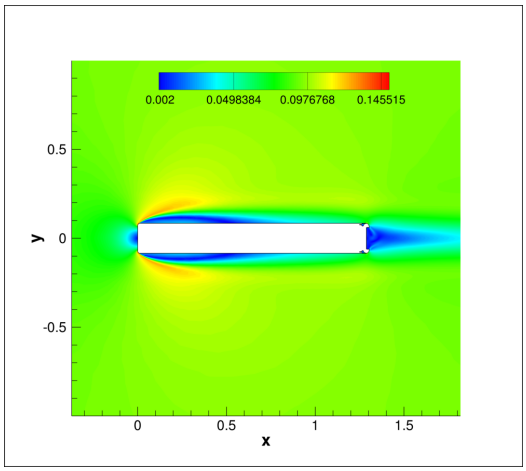

(b) Enhanced GTS model with a Coanda radius of 0.0160 m and C_μ of 0.0253. (Case 7)

Figure 3.15: Mach number contours of the GTS model.

reduction, but also by the power required to energize the jets. Equations 3.1, 3.2, and the power coefficient definition from Equation 3.3 show the mathematical model representing this trade-off. The power consumption behavior clearly shows that there is an ideal combination that will reduce the power requirements. This response surface. Although a higher resolution representation of the design space is required to find the ideal Coanda jet design, the obtained response surface can be used as a guide to understand the aerodynamic changes of each configuration.

The main effect that active flow control is seeking to achieve is a reduction in viscous pressure drag which can be attained by reducing the wake size. From Figure 3.13, is clear that as the momentum coefficient starts to increase, the vehicle power requirements drop. This phenomenon occurs due to the injection of high momentum flow into the Coanda surface, located at the trailing end of the vehicle, which allows the incoming flow to better negotiate the corners. This trend will continue until the point where the required power to energize the Coanda jets overcomes the power savings by drag reduction. An example of this condition can be seen in Figure 3.16, which is case seven from Table 3.2.

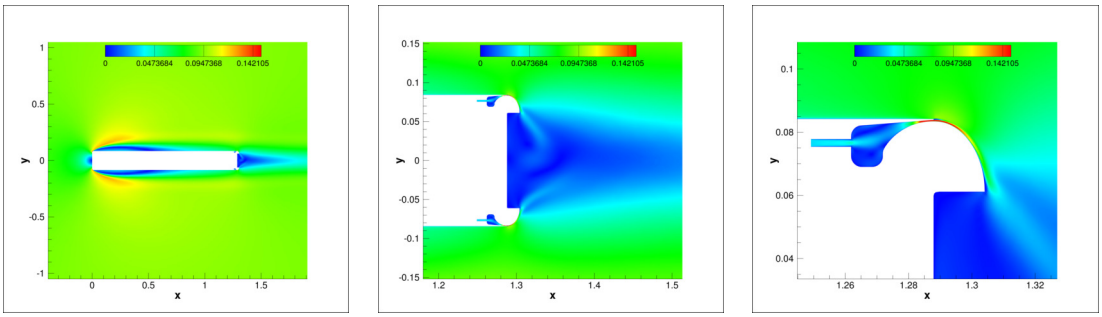

(a) Full view. (b) Zoomed in the trailing end. (c) Zoomed in the Coanda jet.

Figure 3.16: Snapshot of the Enhanced GTS Mach number contour with a Coanda radius = 0.0160 m and $C_\mu = 0.0253$. (Case 7)

As the momentum coefficient continues to increase, it will alter the behavior of the newly constrained wake by injecting flow that has stayed attached through the entire Coanda surface and has enough momentum to impinge on the recirculating area of the wake. The momentum injected into the wake increases the oscillation frequency of this, which leads to a small increase in drag. The dominant contribution of this configuration is the excessive use of power in the Coanda jets, which leads to an overall power requirement increase. Case eleven is an example and its aerodynamic behavior can be seen in Figure 3.17.

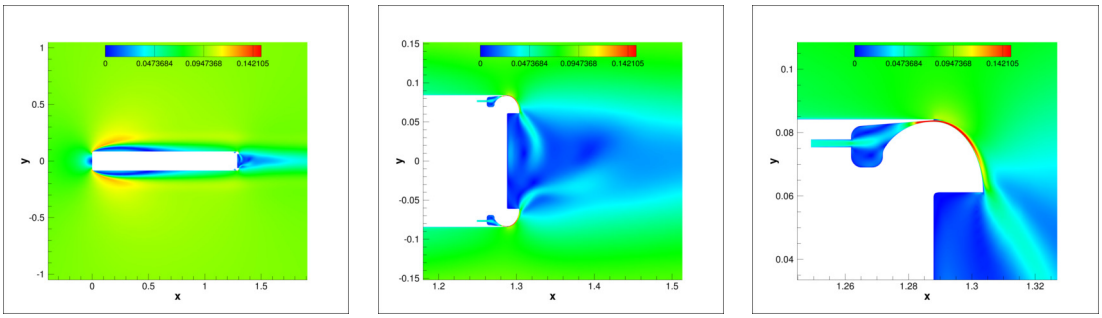

(a) Full view. (b) Zoomed in the trailing end. (c) Zoomed in the Coanda jet.

Figure 3.17: Snapshot of the Enhanced GTS Mach number contour with a Coanda radius = 0.0155 m and $C_\mu = 0.043$. (Case 11)

A second parameter analyzed in this study is the Coanda radius, which has a highly non-linear effect on C_{Pow}. Since the flow injected follows the Coanda surface, this parameter has a direct effect on wake size. Due to the high curvature in the Coanda surface at the lower bound of the Coanda radius, the energy required to maintain the flow attached quickly overwhelms the energy saved through drag reduction. As the radius increases, there is an optimum combination of parameters for which the Coanda radius is ideal to maintain the jet flow attached through the entire circumference while still constraining the wake size. As the Coanda radius continues to grow, the power required to maintain the flow attached follows the same trend driving the system to a condition of high-power usage where the incoming flow separates prematurely from the Coanda surface maintaining a low-pressure region in the wake. Case twelve represents a relatively high C_μ configuration that lacks wake control and leads to high-power requirements and the aerodynamic behavior of this configuration can be seen in Figure 3.18. To control the wake in a high Coanda radius configuration a higher momentum coefficient is required and, although improvements can be seen, the drag reduction is not enough to compensate for the excess energy needed to operate the jets.

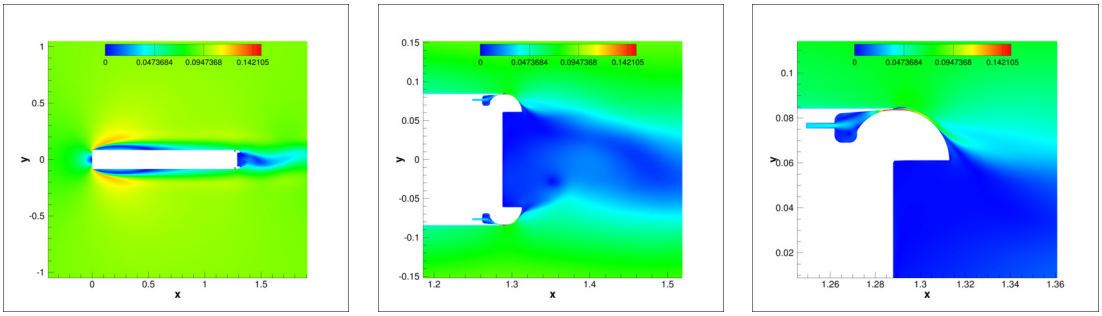

(a) Full view. (b) Zoomed in the trailing end. (c) Zoomed in the Coanda jet.

Figure 3.18: Snapshot of the Enhanced GTS Mach number contour with a Coanda radius = 0.0248 m and $C_\mu = 0.0315$. (Case 12)

The lowest simulated power configuration is case seven and has been highlighted in Table 3.2. The combination of a Coanda radius of 0.0160 m and C_μ of 0.0253 have resulted in a C_{Pow} of 0.6713 and Strouhal number of 0.1051. As expected, the flow in the front portion of both models are identical, but with the addition of the Coanda jets and the injection of flow, the wake size and vortex shedding frequency have been significantly reduced. The Mach number contours shown in Figure 3.15 clearly portray the reduction in the oscillatory behavior of the wake and Figure 3.14 clearly depicts the pressure increase in the back. To better understand the effect of the Coanda jets in the back of the GTS model, a full cycle flow representation of both the base and enhance cases, at the power optimum configuration, have been shown in Figure 3.19.

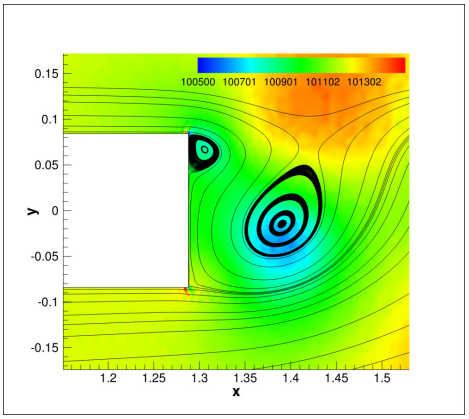

(a) Base - t = 1/4 Tb.

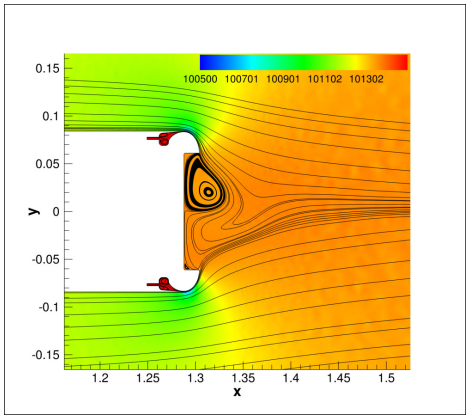

(b) Coanda Jets - t = 1/4 Tj.

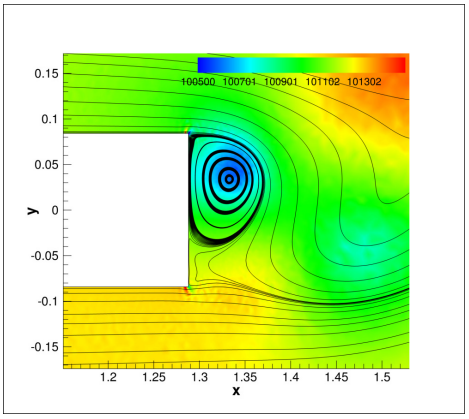

(c) Base - t = 1/2 Tb.

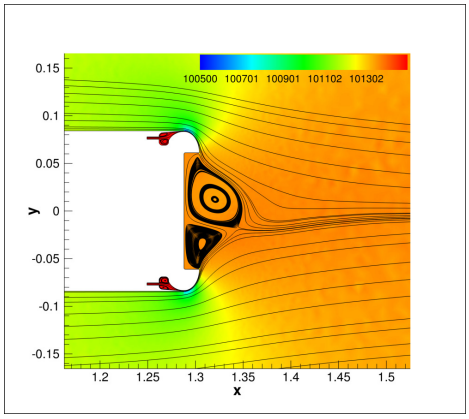

(d) Coanda Jets - t = 1/2 Tj.

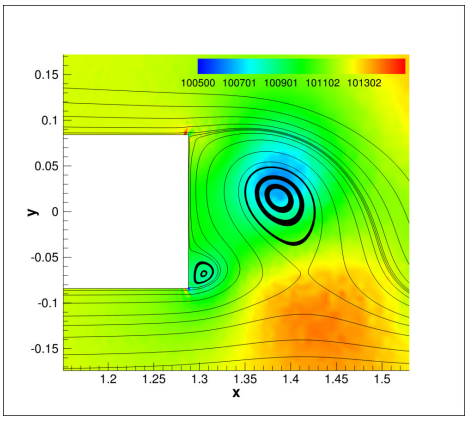

(e) Base - t = 3/4 Tb.

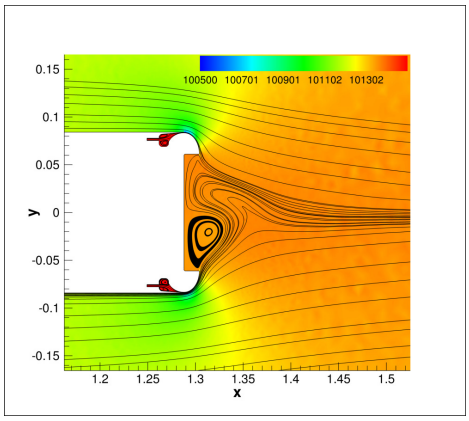

(f) Coanda Jets - t = 3/4 Tj.

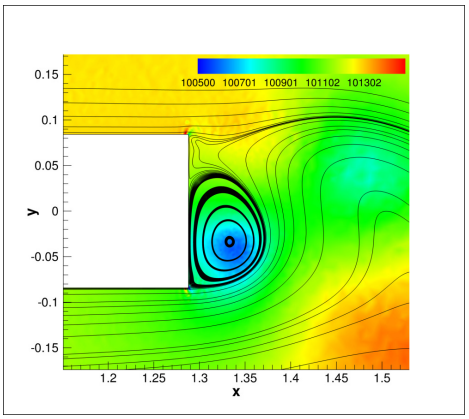

(g) Base - t = Tb.

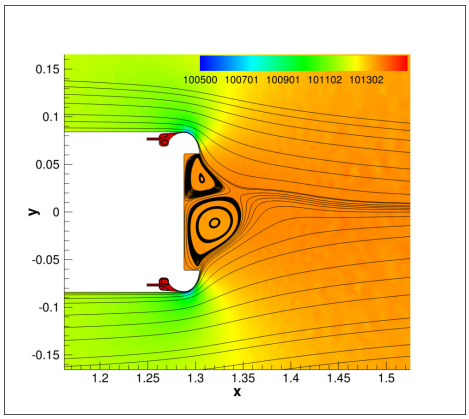

(h) Coanda Jets - t = Tj.

Figure 3.19: Pressure contours of the time history of the streamlines past the base and enhanced GTS model with a Coanda radius of 0.0160 m and C_μ of 0.0253 (Case 7). Tb and Tj represent one shedding period for each the base case and the enhanced case respectively. Pressure in Pascals.

3.3.3 Conclusion

The flow over a two-dimensional representation of the GTS model was simulated and the effects of adding a Coanda jet-based drag reduction system analyzed. To better understand the effects caused by the introduction of this type of AFC system in the aerodynamic profile and power performance of the vehicle, two studies were performed. First the effect of changing the jet strength alone were analyzed, followed by a combined study where both the jet strength and the Coanda geometry shape were changed simultaneously. The effectiveness of this device was first defined as its ability of modify the aerodynamic behavior of the vehicle. Later the notion of energy consumption was introduced and the power required to overcome aerodynamic drag as well as to energize the jets was used as a metric of performance. To minimize the required computational cost to perform these studies, various surrogate models were generated, and the design space represented through them was used

to better understand the system's behavior.

In this chapter I have shown that as the Coanda jets start to inject air into the trailing end of the vehicle the aerodynamic drag is reduced due to an increase in the wake pressure as well as a reduction of wake size and vortex shedding frequency. As the jet strength continues to increase, the power required to energize the jets overruns the power savings due to drag reduction. Furthermore, as the jet strength is further increased, the fluid impinges on the wake introducing energy in the flow which is reflected as a slight increase in drag and vortex shedding. The prevalent effect of this configuration is the unnecessary use of power to energize the jet without the benefit of drag reduction.

In addition to the momentum coefficient, the Coanda surface shape has also been studied and its effects have been shown to play a significant role on the design of this AFC system. At its lower bound, the Coanda surface exhibits a tight curvature radius which requires high momentum flow to prevent premature separation, which translates into a high power requirement. As the Coanda radius increases, the curvature becomes more favorable and a diminished amount of power is required for optimal performance. As the radius approaches the upper boundary, the Coanda surface length and the momentum requirements for the system to control the wake behavior increases, causing an increase in required power.

The main objective of this chapter was to understand the effects of jet momentum coefficient and Coanda surface geometry on the aerodynamic behavior and energy consumption of the vehicle. Although it is well understood that the flow over the GTS model is highly three-dimensional, this studies were designed to gain insight into the effects each of the components forming the Coanda jet-based AFC system have.

Chapter 4

Three-Dimensional Studies of Active Flow Control for Drag Reduction

4.1 Physical Model

4.1.1 Geometrical Model

Starting from the results presented in Chapter 3, its clear that to better understand the aerodynamics of heavy vehicles and the real effect that Active Flow Control (AFC) systems have in both drag and power consumption of these, a three-dimensional model needs to be studied. The aerodynamic features that characterize separated flows, and the quantification of the effects that add-on drag reduction devices have on the presence of viscous pressure drag, a streamlined model of a heavy vehicle is sufficient [93, 30]. Heavy vehicles have a variety of features that contribute towards flow separation, such as mirrors, antennas, gaps, mud flaps, etc., and to eliminate the effect that these have, the Ground Transportation System (GTS) [30] model was used.

This geometrical model was developed by a United States Department of Energy consortium to focus on the study of viscous pressure drag. The GTS effectively combines both the tractor and the trailer into a single simplified bluff body that has an elliptical leading shape and ends in a sharp straight cut in the back [30]. To maintain consistency with the two-dimensional studies, the scale of the GTS model used remained at 6.5%, but the actual shape of the model was modified to meet the Department of Energy specification. The GTS geometry both with and without the AFC system outfitted on the back of the vehicle can be seen in Figures 4.1 and 4.2.

The location of all four jets in the back of the GTS was selected to increase reattachment while

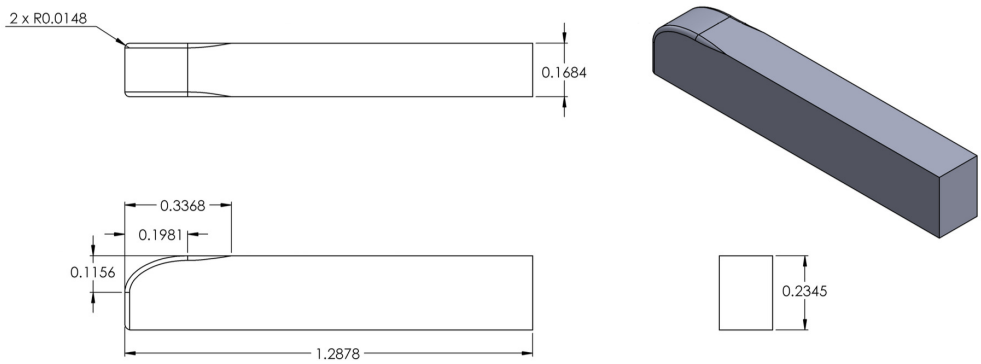

Figure 4.1: Baseline three-dimensional GTS model - Scale 6.5%. All dimensions in meters.

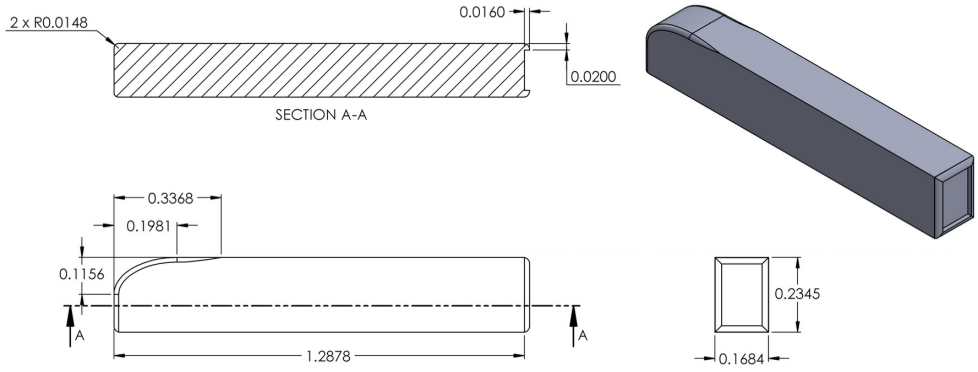

Figure 4.2: Three-dimensional GTS model with Coanda Jets in the trailing edge - Scale 6.5%. All dimensions in meters.

limiting the interaction between jets. The size and spatial distribution of the jets were chosen based on the two-dimensional studies performed by the author [55, 56], which have been compiled in Chapter 3. For this study, spacing between the top of the jet and the roof of the GTS was eliminated, in an attempt to reduce grid complexity, allowing the jet to begin at the edge and have a thickness of 0.77978 mm. This approach enforces consistency on the Coanda surface location between the two- and three-dimensional geometries. The jet position can be seen in Figure 4.3. This jet design selection maximizes the effect of the jets, since the high-momentum air helps the majority of the flow coming from the vehicle's rooftop negotiate the sharp corners and reduces the recirculation region length.

4.1.2 Flow Conditions

The flow around the GTS model was simulated assuming standard air at sea-level treated as a calorically perfect ideal gas. The velocity was chosen to match the average highway speed, which is 31.3 m/s (70 mph) which translates to a Mach number of 0.09195 and Reynolds number, using the GTS model width as the length scale, of $359,900$. Computing the Reynolds number as a function of the vehicle width is standard in this field, and allows for the direct comparison of the integrated force coefficients with the experimental data reported by Storms *et al.* [89] and Englar [23], as well as the computational results by Roy *et al.* [82]. Furthermore, the information provided by Englar [23] and Pfeiffer *et al.* [74] concerning AFC for ground vehicles were used to guide the design space exploration.

In this study the drag was monitored and the physical flow changes surrounding the vehicle analyzed, but the total power consumption of the vehicle was used as the objective function. This metric is composed by the power required to overcome aerodynamic drag combined with the power used to energize the AFC system. The power used to overcome drag was defined as

$$P_{aero} = D * U_{\infty}, \tag{4.1}$$

where D is the aerodynamic drag and U_{∞} is the free-stream velocity. In addition, the power required to energize each Coanda jet in the AFC system is quantified by the change in kinetic energy of the injected fluid scaled by an efficiency factor to account for system irreversibilities:

$$P_{comp} = \frac{\frac{1}{2} * \dot{m}_e * V_e^2}{\eta}, \tag{4.2}$$

where the mass flow rate through the jet is $\dot{m}_e$, V_e is the area-averaged jet velocity, and η is the efficiency factor, which was set to be 90% based on compressor isentropic efficiency values. For this study, the jets were modeled by imposing a velocity profile that was extracted from the two-dimensional results shown in previous work by the author [56].

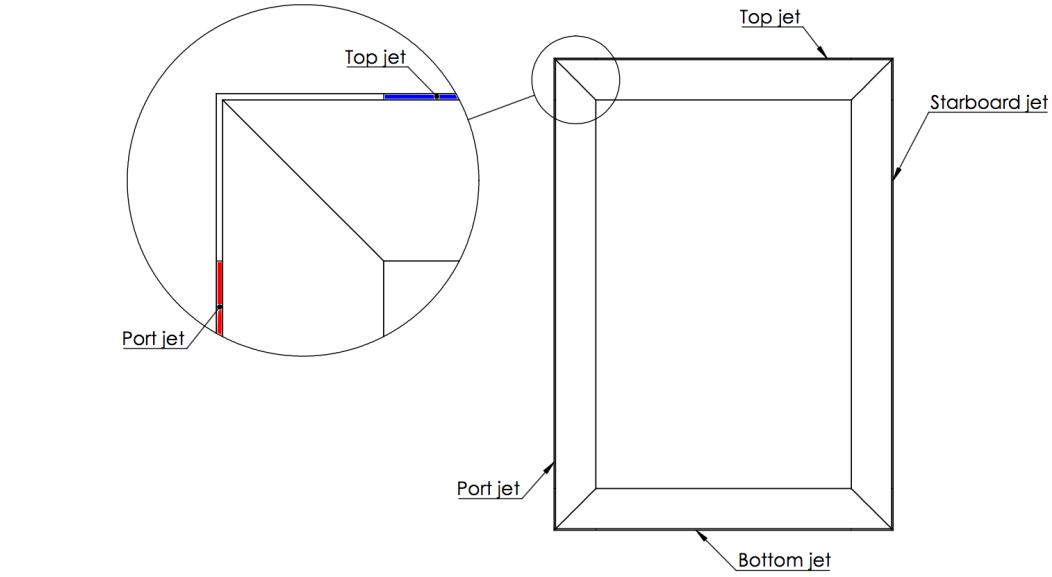

(a) Jet configuration.

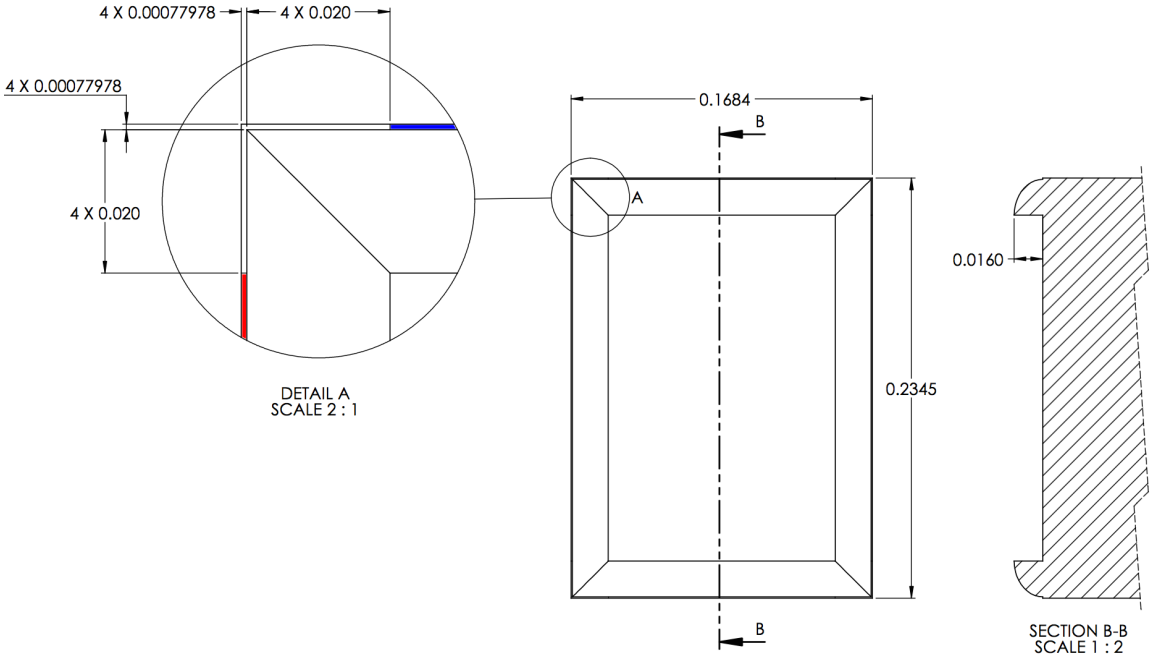

(b) Jet dimensions.

Figure 4.3: Coanda jets in the back of the enhanced GTS model. In the detailed view the top jet is shown in red and the port jet in blue.

Non-dimensional coefficients for the drag, lateral forces, and lift have been defined as follows:

$$C_D = \frac{D}{q * A}, \qquad C_{LF} = \frac{LF}{q * A}, \qquad C_L = \frac{L}{q * A}, \tag{4.3}$$

where C_D is the drag coefficient, q is the dynamic pressure calculated as $\frac{1}{2}\rho_\infty U_\infty^2$, ρ_∞ is the free-stream density, A is the cross-sectional area calculated as $W * H$, W is the width and H the height of the base GTS model, C_{LF} is the lateral force coefficient, LF is the dimensional lateral force, C_L is the lift coefficient, and L is the dimensional lift force. To characterize the jet strength and power consumption similar definitions are used:

$$C_\mu = \frac{\dot{m}_e * V_e}{q * A}, \qquad C_{Pow} = \frac{P_{aero} + P_{comp}}{q * U_\infty * A}, \tag{4.4}$$

where C_μ is the momentum coefficient and C_{Pow} is the power coefficient.

4.2 Computational Model

The use of Computational Fluid Dynamics (CFD) for the design of heavy vehicle drag reduction systems requires a balance between accuracy and computational cost, and a compromise was reached by using the second-order accurate Jameson-Schmidt-Turkel (JST) [42] convective scheme and a corrected average of gradients viscous scheme [98] for the mean flow, in combination with the Shear-Stress-Transport (SST) [62] turbulence model. In the previous two-dimensional studies, these tools were applied in a time-accurate setting with Unsteady Reynolds-Averaged Navier-Stokes (URANS) to resolve the periodic nature of the flow. The introduction of AFC systems at the trailing end of the two-dimensional GTS model reduced the frequency of vortex shedding. The optimal configuration for these types of systems occurred when the wake was fully enclosed and, for all practical purposes, resulted in a steady flow field around the vehicle [56]. The influence of the AFC system on the flow field can be seen in Figure 4.4.

To verify this assumption, a two-dimensional GTS model equipped with the AFC system was studied using Reynolds-Averaged Navier-Stokes (RANS) and URANS, were both simulations used the AFC system configuration optimized for power. This configuration used a 0.0253 jet momentum coefficient and Coanda radius of 0.0160 m. The time-averaged C_D obtained using a URANS approach for the model shown in Figure 4.4b is 0.5988 [56] and its RANS counterpart is 0.5984, which is 0.067% lower. This result contributes towards the hypothesis that introducing AFC drag reduction systems in the two-dimensional model stabilizes the wake and transforms it into a problem that can be treated accurately by a steady-state solver.

A significant factor that needs to be addressed when looking into the aerodynamic simulation of ground vehicles is ground effect. Studies by Kim *et al.* [44] and Agarwal [2] show that ground effect has a stabilizing influence on the wake with respect to the ground normal component. The added

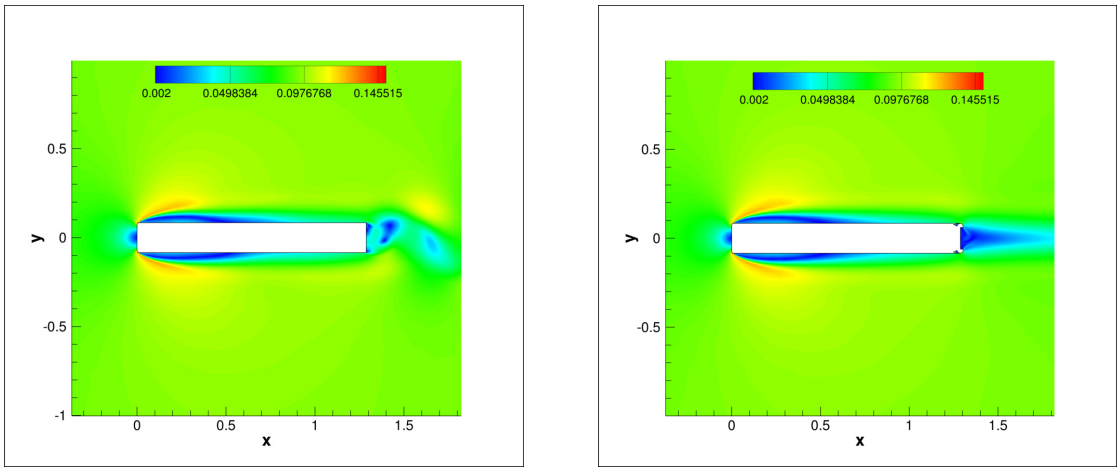

(a) Base GTS model.

(b) Enhanced GTS model with a Coanda radius of 0.0160 m and C_μ of 0.0253.

Figure 4.4: Mach number contours of the two-dimensional GTS model.

stabilization effect provided by the ground combined with the flow stabilization capabilities of the Coanda jets in the vehicle opens the door for the use of steady-state solvers to design AFC drag reduction systems. Basing our approach on this hypothesis, we perform the design and optimization of this AFC system using the steady-state solver built into the open-source SU2 suite for CFD analysis and design [20, 69, 70].

The computational mesh that was used to represent the GTS geometry is fully unstructured with mixed element types. The boundary layer region is represented by prisms while the rest of the mesh is composed of tetrahedra. The base GTS model mesh has $2,147,204$ points, corresponding to $10,616,539$ cells, and the Coanda jet-equipped GTS has $2,586,690$ points, which corresponds to $11,112,620$ cells. These grids were constructed to guarantee that the y^+ remains below 1. In the development of these grids, special emphasis was placed on refining the wake region, since this is the area of interest for the design of AFC systems. The base GTS computational grid can be seen in Figure 4.5, and the grid for the model outfitted with the AFC system in Figure 4.6.

The GTS surface has been treated using an adiabatic no-slip condition. The far-field boundary of the domain is located in the axial direction at 5 truck lengths from the front and 9 truck lengths from the back. In the direction perpendicular to the flow, the vehicle is centered within 11 truck lengths, and in the direction normal to the ground, the domain spans 5 truck lengths. The outer domain boundaries are treated with the typical characteristic-based far-field condition for external aerodynamics. Finally, the ground plane is modeled using a slip condition, to avoid influencing the solution with the presence of a boundary layer.

To reduce the grid size and the computational resources required for this study, the jets were modeled through boundary conditions with specified velocity profiles, rather than modeling full

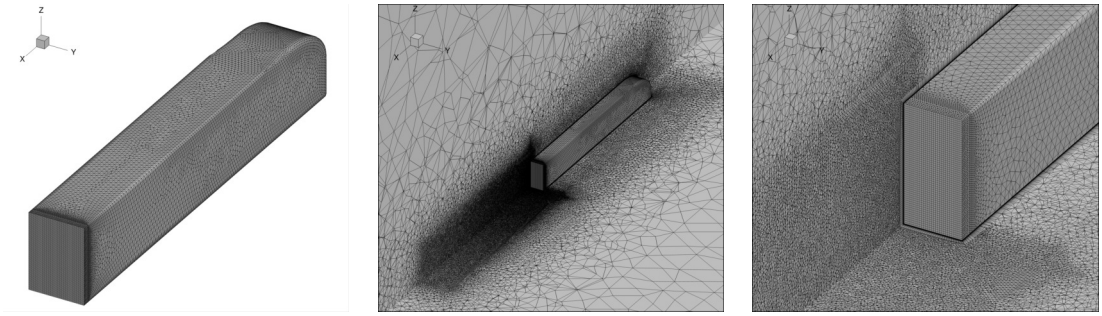

(a) Surface mesh.

(b) Volumetric mesh with planes at y/W = 0 and at z/W = 0.35 .

(c) Back of the GTS with planes in y/W = 0 and z/W = 0.35 .

Figure 4.5: Grid for the GTS base model.

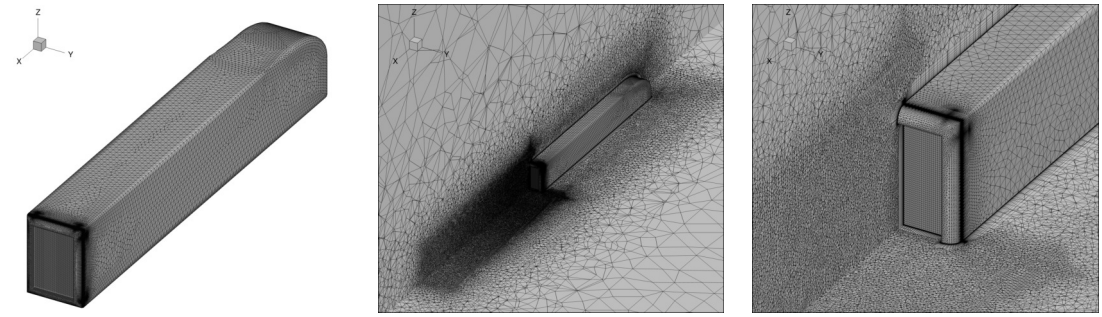

(a) Surface mesh.

(b) Volumetric mesh with planes at y/W = 0 and at z/W = 0.35 .

(c) Back of the GTS with planes in y/W = 0 and z/W = 0.35 .

Figure 4.6: Grid for the GTS model with Coanda jets .

plenums and nozzles internal to the vehicle. To recover proper behavior, these boundary conditions were implemented in SU2 as characteristic-based inlet conditions [35] with both the velocity and density being specified on the jet face.

4.2.1 Velocity Profile

In order to accurately represent the velocity profile of the jet without modeling the plenum and nozzle, velocity profiles were extracted from the two-dimensional optimization results published by the author [56], and a polynomial was fitted to the data. Once the polynomial was obtained, this was normalized with respect to the peak velocity and, for ease of handling inside SU2, the independent variables were mapped to span from -1 to 1. The polynomial used to represent the jet velocity profile is shown in Equation 4.5, and the function used to map it to the actual geometrical coordinates is Equation 4.6.

$$\begin{aligned} P_{bottom}^{top} = -0.7085458261471165\ \tilde{z}^4 \pm 0.0082692314282440\ \tilde{z}^3 \\ -0.2913746290723793\ \tilde{z}^2 \mp 0.008259922266006\ \tilde{z} + 0.9999361038208008, \end{aligned} \tag{4.5}$$

$$\tilde{z} = \frac{z - z_{min}}{z_{max} - z_{min}} * 2 - 1, \tag{4.6}$$

where $\tilde{z}$ is the mapped variable that goes from -1 to 1, z is the physical variable, and z_{max} and z_{min} are the physical limits between which the polynomial needs to be mapped. Figure 4.7 shows the two-dimensional Coanda jet and the normalized extracted polynomial for the top jet mapped to the two-dimensional jet location.

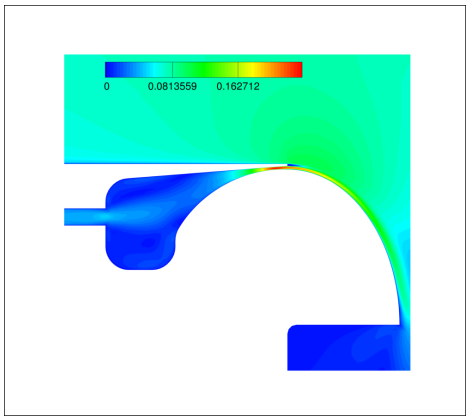

(a) Mach number contour of the two-dimensional top jet.

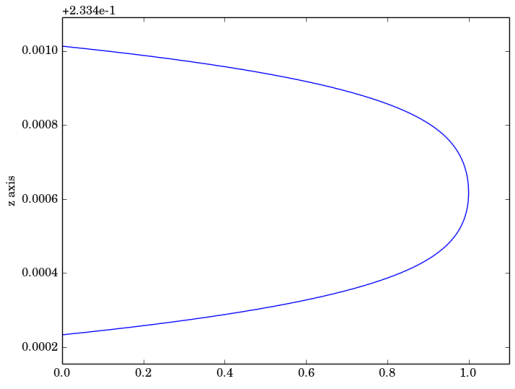

(b) Normalized velocity profile extracted from the top jet.

Figure 4.7: Velocity profile extracted from the 2D Coanda jet.

The transverse profile of each jet was approximated using a piece-wise function. This approach aims to accommodate the boundary layer growth inside of the plenum. The approximate boundary layer thickness is estimated using the turbulent boundary layer approximation over a flat plate for a flow that has traveled one truck width using Equation 4.7.

$$\delta = \frac{0.382\ W}{Re^{1/5}}, \tag{4.7}$$

$$Re = \frac{\rho_p * V_{peak} * W}{\mu_p}, \tag{4.8}$$

$$\mu_p = 1.716 * 10^{-5} \left[\frac{T_p}{273.15}\right]^{\frac{3}{2}} \left[\frac{273.15 + 110.4}{T_p + 110.4}\right], \tag{4.9}$$

where δ is the boundary layer thickness, W is the GTS model width, Re is the Reynolds number, ρ_p is the jet density calculated assuming the injected flow to be an ideal gas at $T_p = 290\ K$ and a pressure of 101325 Pa, V_{peak} is the peak velocity of the jet, and μ_p is the jet viscosity computed using Sutherland's law [92].

The function representing the transverse jet behavior has been normalized with respect to the peak velocity and the independent variable mapped to span between -1 and 1. Equation 4.10 describes this relationship and its graphical representation mapped at the spatial location of the top jet using Equation 4.6 is shown in Figure 4.8.

$$R = \begin{cases} 1 - \frac{4}{4\tilde{\delta}^2} * (\tilde{y} + 1 - \tilde{\delta})^2 & \text{if } -1 < \tilde{y} < -1 + \tilde{\delta}, \\ 1 & \text{if } -1 + \tilde{\delta} < \tilde{y} < 1 - \tilde{\delta}, \\ 1 - \frac{4}{4\tilde{\delta}^2} * (\tilde{y} - 1 + \tilde{\delta})^2 & \text{if } 1 - \tilde{\delta} < \tilde{y} < 1. \end{cases} \tag{4.10}$$

These functions are combined to form the three-dimensional velocity profile for the jet. The function representing this velocity distribution is $M(z, y)$, and its relationship with the previously presented profiles is described in Equation 4.11. The three-dimensional profile can be seen in Figure 4.9. All other jets are model using the same equations but in their specific spatial locations.

$$M(z, y) = P(z) * R(y) * V_{peak} \tag{4.11}$$

4.3 Design Optimization

The studies performed in Chapter 3 have shown that AFC systems are capable of reducing drag and power consumption in the two-dimensional representation of a heavy vehicle. Building upon the previously presented results, this section focuses on the aerodynamic enhancing capabilities of these systems for a three-dimensional representation of a tractor trailer.

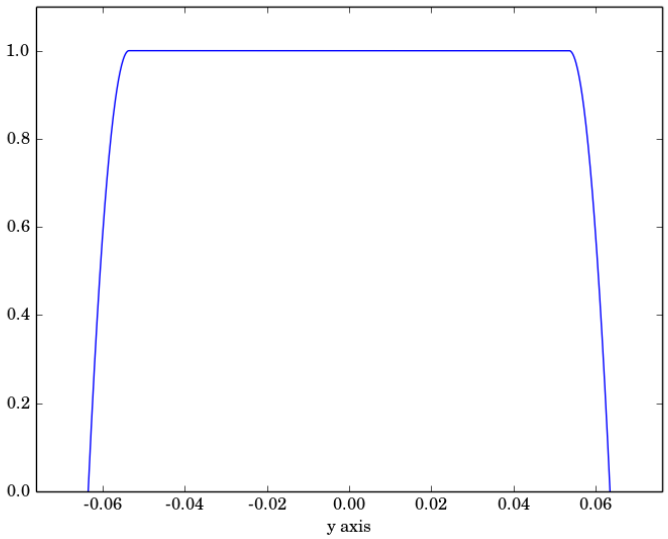

Figure 4.8: Normalized transverse velocity profile for the top jet.

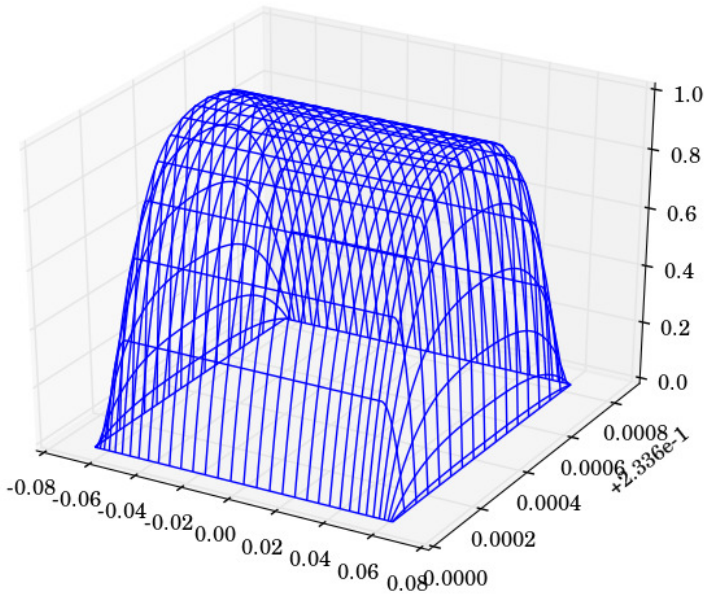

Figure 4.9: Normalized three-dimensional profile for the top jet.

The amount of air, speed at which it gets injected, and the blowing configuration of the AFC system are of the utmost importance for the design of these systems. To explore the design space using these as variables, a two-step approach was used. First, the jet momentum coefficient (C_μ) was set to be the same in all four jets, and the value for this varied. Second, the C_μ controlling the top, bottom, and side jets were allowed to vary independently, increasing the system's degrees of freedom and allowing for the exploration of not only the effect of jet strength, but also configuration in the aerodynamic and power performance of the vehicle.

4.3.1 Parametric Study

At first a parametric studies was performed maintaining the momentum coefficient constant across all four jets. The drag (C_D) and power (C_{Pow}) coefficients have been computed from the numerical simulation, and a continuous model of their behavior was generated using Gaussian Process Regression (GPR) [26]. This approach is used to generate a surrogate model of the system by fitting a curve in a probabilistic manner through the points evaluated. Additionally, this technique provides an uncertainty metric, represented by a covariance function [26], which can be used to guide the selection of future function evaluations as well as to have a metric for the uncertainty involved in the surrogate model. In this study, an squared exponential kernel was used for the covariance function, which is a representation of the standard deviation.

Table 4.1 shows the eleven equally-spaced cases that were used to sample the design space.

$\boldsymbol{Case}$	$\boldsymbol{C_\mu}$	$\boldsymbol{C_{\mu_j}}$	$\boldsymbol{V_{tb_{peak}}}$	$\boldsymbol{V_{ps_{peak}}}$
1	0.0000	0.0000	20.6737	16.6907
2	0.0049	0.0012	29.2089	23.5887
3	0.0098	0.0024	35.7544	28.8796
4	0.0147	0.0037	41.2705	33.3389
5	0.0196	0.0049	46.1291	37.2670
6	0.0245	0.0061	50.5208	40.8178
7	0.0294	0.0073	54.5586	44.0827
8	0.0342	0.0086	58.3165	47.1214
9	0.0391	0.0098	61.8456	49.9751
10	0.0440	0.0110	65.1831	52.6740
11	0.0489	0.0122	42.9844	34.7245

Table 4.1: Summary of the momentum coefficient and the corresponding velocities for each jet. C_μ is the total momentum coefficient, C_{μ_j} is the momentum coefficient per jet, $V_{tb_{peak}}$ is peak velocity for the top and bottom jets in $\frac{m}{s}$, $V_{ps_{peak}}$ is the peak velocity for the port and starboard jets in $\frac{m}{s}$.

The C_μ of all four jets combined was selected to vary between 0.00 and 0.0489, based on the work

by Pfeiffer *et al.* [74] and the experience from previous work on this topic by the author [55, 56]. C_μ was controlled by varying the peak velocity, which in turn changes the velocity profile. For the present jet configuration, the jet areas for both the top and bottom jets are the same, and the areas for the port and starboard jets are the same, but they differ between them. This disparity causes the peak velocity to be different between the two groups in order to maintain a constant C_μ.

Results

The use of RANS for the simulation of the flow past the basic GTS model has first been compared to experimental results found in the literature, and a summary of these can be found in Table 4.2.

Contribution	***Supports***	$\boldsymbol{Re_W}$	$\boldsymbol{C_D}$
Storms et al., 2001[89]	4	$360,000$	$0.37 - 0.40$
Englar 2001 [23]	1	$359,900$	0.43
Present	0	$359,900$	0.3323
Present	1	$359,900$	0.3959
Present	4	$359,900$	0.4070

Table 4.2: Experimental and computational results for the flow past the base GTS model. *Supports* are the number of cylindrical supports holding the GTS model, Re_W is the width based Reynolds number, and C_D is the vehicle drag coefficient.

Since the cylindrical supports that hold the model in place have not been modeled in this computational study, a correction has been used for comparison. To approximate the additional drag caused by having one and four cylindrical supports at the bottom of the GTS model, a two-dimensional diameter-based drag coefficient of 1 was used. The ground clearance of the vehicle was used as the strut length, which is 0.0447 m, the diameter was taken to be 0.05613 m for the single strut and 0.01650 m for each of the four struts. This correction amounts to 0.06354 and 0.07472 three-dimensional GTS-area-based drag coefficient respectively which was added to the vehicle aerodynamic C_D.

As can be seen, the C_D obtained is in good agreement with the results reported in the literature, and the values reported without the strut correction will be used as the base case drag moving forward. In addition to the quantitative results shown in Table 4.2, the wake structure for the base GTS model has been visualized and compared to the results presented by Roy *et al.* [82] and Storms *et al.* [89]. Figures 4.10 and 4.11 have been generated to match the available data and are in good agreement with the RANS results reported in the literature, but as expected, the experimental Particle Image Velocimetry (PIV) results for the wake structure differ. Despite these differences, the wake stabilizing effect of the ground [44, 2] allows for the accurate prediction of integrated forces.

The introduction of Coanda jets along the back of the GTS model stabilizes the wake further,

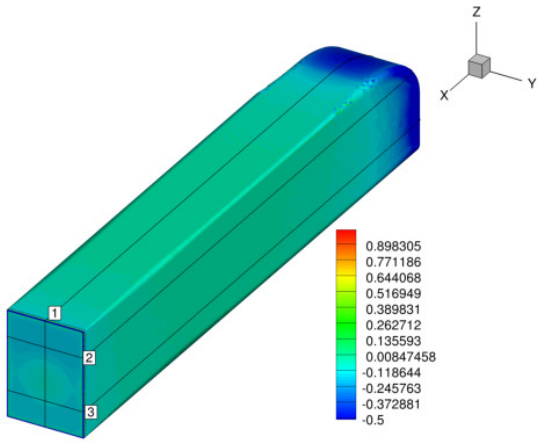

Figure 4.10: Pressure coefficient and the location of the planes where the wake is visualized in the base GTS model. Cut 1 is located at y/W = 0, cut 2 is located at z/W = 1.05 and cut 3 is located at z/W = 0.35.

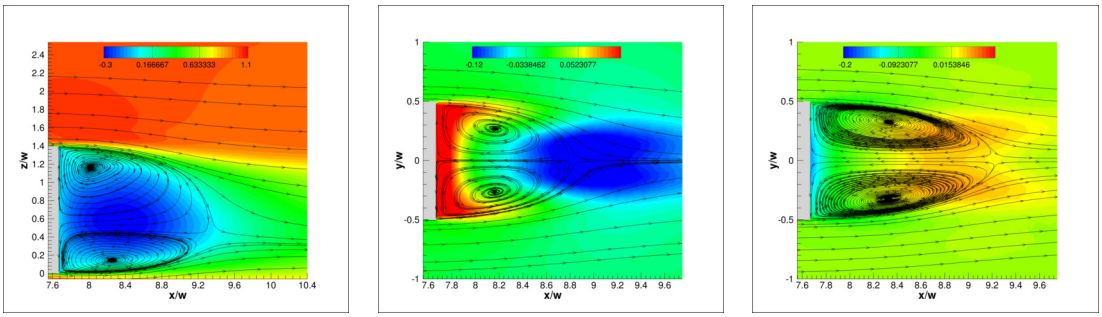

(a) Non-dimensional axial velocity in cut 1.

(b) Non-dimensional velocity normal to the ground in cut 2.

(c) Non-dimensional velocity normal to the ground in cut 3.

Figure 4.11: Visualization of the wake flow for the base GTS model at a Re_W of 359,900 and a Mach number of 0.09195.

while increasing the back pressure. This AFC system not only reduces drag, but also alters the flow around the vehicle, restraining the wake and increasing its stability. A parametric study was performed by varying the momentum coefficient of the jets to better understand the effect that this AFC system has on the GTS model. Table 4.3 summarizes the results obtained and Figure 4.12 shows the response of C_D and C_{Pow} as a function of C_μ.

$\boldsymbol{Case}$	$\boldsymbol{C_\mu}$	$\boldsymbol{C_{\mu_j}}$	$\boldsymbol{C_D}$	$\boldsymbol{C_{Pow}}$
1	0.00000	0.00000	0.3154	0.3154
2	0.00489	0.00122	0.3033	0.3045
3	0.00978	0.00245	0.2937	0.2971
4	0.01468	0.00367	0.2869	0.2933
5	**0.01957**	**0.00489**	**0.2824**	**0.2921**
6	0.02446	0.00612	0.2797	0.2933
7	0.02935	0.00734	0.2783	0.2962
8	0.03425	0.00856	0.2777	0.3003
9	0.03914	0.00978	0.2856	0.3132
10	0.04403	0.01101	0.3118	0.3448
11	0.04892	0.01223	0.3123	0.3509

Table 4.3: Parametric study results for a Coanda jet-based AFC system mounted in the trailing end of the GTS model. C_μ is the total momentum coefficient, C_{μ_j} is the momentum coefficient per jet, C_D is the drag coefficient and C_{Pow} is the power coefficient.

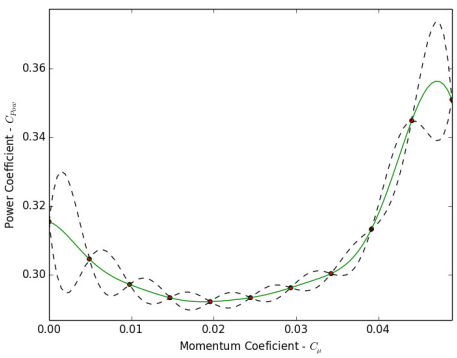

(a) C_{Pow} as function of C_μ. The dashed lines are the bounds for 95% confidence.

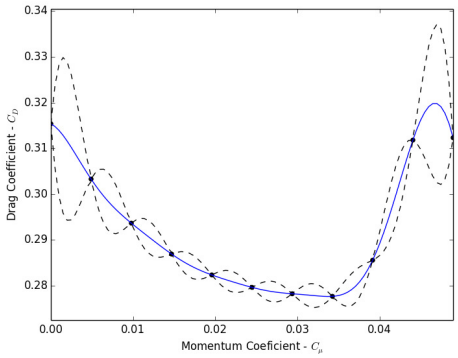

(b) C_D as function of C_μ. The dashed lines are the bounds for 95% confidence.

Figure 4.12: Surrogate models representing the behavior of power and drag for the GTS model outfitted with Coanda jets.

The surrogate models generated provide a continuous representation of the integrated forces and power consumption behavior as the jet strength is varied. This design space representation was used to approximate the jet configuration required to achieve minimum power consumption, which was found at $C_\mu = 0.01869$. The proximity of this configuration to case 5, which is $C_\mu = 0.01957$, and the response surface shape, lead to the selection of case 5 as the minimum power configuration for further investigation. Case 5 generated a $C_D = 0.2824$ and requires a $C_{Pow} = 0.2921$, which is equivalent to a 15% drag and a 12% power reduction with respect to the base GTS model.

The drag and power consumption improvement achieved due to the effect of the AFC system is due to changes in the wake behavior behind the vehicle. As expected, the injection of air through the Coanda jets restrain the wake and reduce it size. Figure 4.13 shows the wake structure for both the base GTS model and the GTS model with Coanda jets installed.

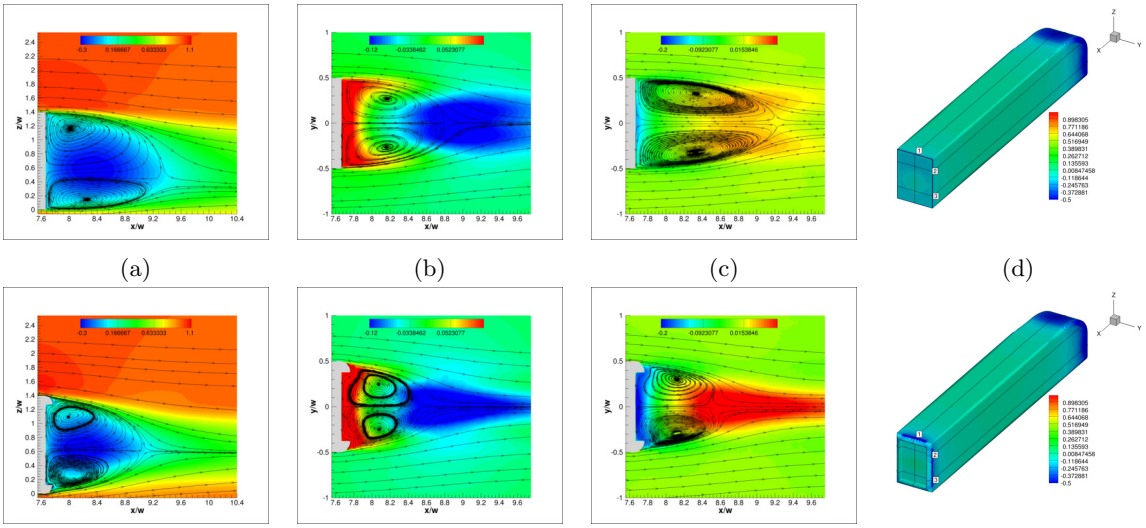

(a) (b) (c) (d)

(e) (f) (g) (h)

Figure 4.13: Wake comparison between the base GTS model and the GTS model outfitted with the add-on Coanda jet-base AFC system. (a) and (e) show the non-dimensional axial velocity at plane $y/W = 0$, (b) and (f) show the non-dimensional ground normal velocity at plane $z/W = 1.05$, (c) and (g) show the non-dimensional ground normal velocity at plane $z/W = 0.35$, and (d) and (g) the plane locations in the three-dimensional models. Figures (a), (b), (c), and (d) represent the base GTS and figures (e), (f), (g), and (h) the GTS model outfitted with the AFC system at a blowing strength $C_\mu = 0.01957$ (Case 5). Both simulations took place at a width-based Reynolds number of 359,900, and Mach number of 0.09195.

By looking at Figure 4.13(a) and (e), it can be seen that the wake has not only been reduced in size, but the injection of flow from the bottom jet increases its symmetry and moves the stagnation point further away from the ground. This effect can also be visualized by comparing Figure 4.13(b) with (f) and (c) with (g), where the magnitude of the ground normal velocity has increased and the distribution shows the symmetry increase. This reduction in wake size leads to an increase in wake

stability and symmetry, as well as to a pressure increase on the back of the vehicle. Figure 4.14 shows the pressure coefficient contours on the GTS vehicle back for both the base and Coanda jet configurations.

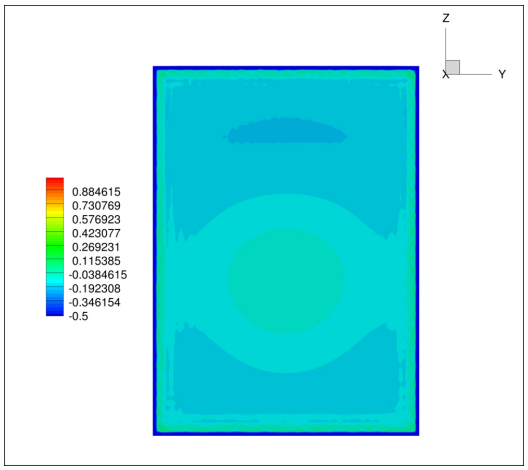

(a) Base case.

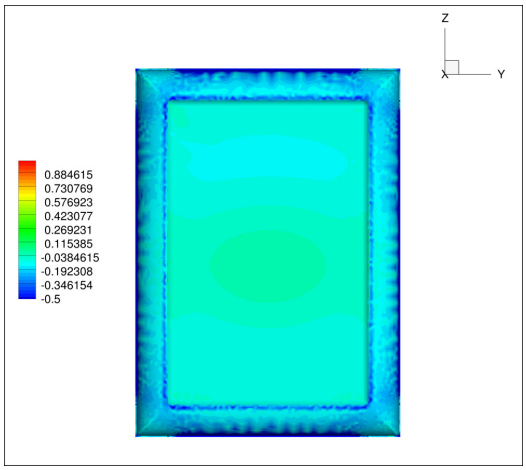

(b) Enhanced case using a C_μ of 0.01957. (Case 5)

Figure 4.14: Pressure coefficient distribution on the back of the base and enhanced GTS model at a Re_W of 359,900 and Mach number of 0.09195.

Comparing Figure 4.14(a) and (b), we see that the introduction of the Coanda jet AFC system increases the overall pressure on the back face of the vehicle. This view also highlights how the injection of flow through the bottom jet acts to shift the wake core upwards. In addition, it can be seen that the low-pressure ring caused by separation on the back of the base GTS vehicle has been eliminated in the regions where the jets are acting, but it has been replaced by localized low-pressure regions on the Coanda surfaces. These low pressure regions are caused by the introduction of high-speed flow from the jet and are responsible for helping the free-stream flow turn around the corner and confine the wake. It is evident that these two effects compete with each other, as the pressure on the flat back surface increases with jet velocity, the Coanda surface pressure decreases. This effect can be better understood by looking at Figures 4.15, 4.12, and Table 4.4.

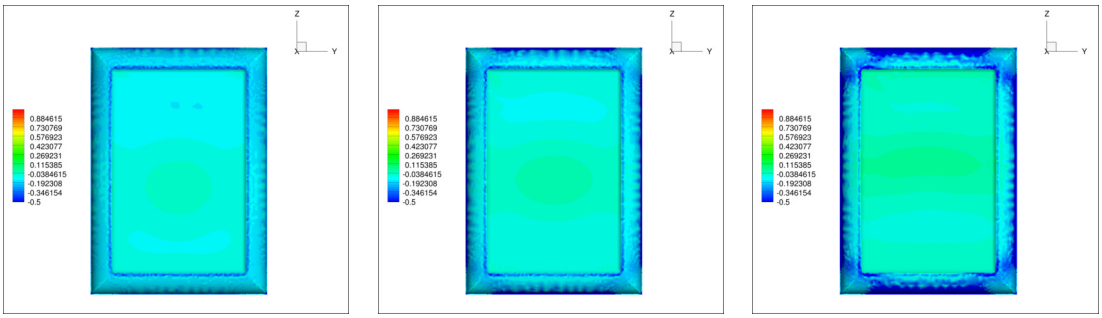

(a) Case 2 where $C_\mu = 0.00489$. (b) Case 5 where $C_\mu = 0.01957$. (c) Case 9 where $C_\mu = 0.03914$.

Figure 4.15: Pressure coefficient distribution on the back of the enhanced GTS model at a Re_W of 359,900 and Mach number of 0.09195.

$\boldsymbol{Case}$	$\boldsymbol{C_\mu}$	$\boldsymbol{C_{D\ back}}$	$\boldsymbol{C_{D\ Coanda}}$	$\boldsymbol{C_D}$	$\boldsymbol{C_{Pow\ aero}}$	$\boldsymbol{C_{Pow\ comp}}$	$\boldsymbol{C_{Pow}}$
Base	0.00000	0.1810	0.0000	0.3323	0.3323	0.0000	0.3323
2	0.00489	0.0688	0.0714	0.3033	0.3033	0.0012	0.3045
5	0.01957	0.0503	0.0795	0.2824	0.2824	0.0098	0.2921
9	0.03914	0.0300	0.1171	0.2856	0.2856	0.0276	0.3132

Table 4.4: C_D and C_{Pow} break down. C_μ is the jet momentum coefficient, $C_{D\ back}$ is the drag contribution from the back of the truck, $C_{D\ Coanda}$ is the drag contribution from the Coanda surfaces, C_D is the vehicle drag coefficient, $C_{Pow\ aero}$ is the power required to overcome aerodynamic drag, $C_{Pow\ comp}$ is the power required to energize the jets and C_{Pow} is the overall required power coefficient.

Figure 4.15(a) shows a low-momentum coefficient configuration where the back pressure increases while the Coanda surface pressure remains relatively high. This allows for a decrease in drag without a significant power consumption increase due to jet actuation. As the momentum coefficient is increased toward its ideal value, the back pressure increases further, and the Coanda surface pressure drops. The pressure contour for this configuration is shown in Figure 4.15(b) and the values can be seen in Figure 4.4. The use of this AFC system causes drag reduction, but the rate at which this occurs is reduced due to the competing effect of the integrated forces on these surfaces. In addition, as the momentum coefficient is increased, the power required to actuate the AFC system raises. In case 9, which can be seen in Figure 4.15(c), the momentum coefficient has been increased to a point where the change in drag due to back pressure increase has been completely overshadowed by the pressure decrease on the Coanda surfaces. This configuration not only leads to an increase in the power required to overcome drag, but also to an increase in the power required to actuate the jets.

4.3.2 Full Factorial Study

After looking at the effect that jet strength has on the power consumption and aerodynamic behavior of the vehicle, the focus shifted towards blowing configuration to further improve aerodynamic efficiency. It was shown, in the previous section, that a 12% power reduction can be achieved by varying the momentum coefficient of all jets as a single variable [54]. The study presented in this section leveraged on the understanding of ground effect and its stabilizing influence in the wake behavior [44, 2], which in addition to allowing for the reduction of computational costs, unveiled the need for jet specific momentum coefficients. The introduction of these new variables opened the design space to the existence of new power coefficient extrema, which can be found by better understanding the physics behind aerodynamic modifications. Due to symmetry, the port and starboard jets, also referred as side jets, can be controlled using a single parameter, but the top and bottom jets need to be controlled individually [57].

To span the design space, a full-factorial study was put in place, where each momentum coefficient (C_μ) was allowed to vary between 0.00125, 0.005625 and 0.01. The 27 function evaluations that result from the permutation of these blowing coefficients can be seen in Table 4.5. The peak velocities shown in this table are inversely proportional to the corresponding jet area. Therefore, the peak velocity differences at a given C_μ between top, bottom, and side jets are due to this feature.

To better interpret the results obtained from this study, the data has been split in three groups keeping the bottom jet momentum coefficient ($C_{\mu B}$) constant for each group due to its direct relation with ground effect. Each group is conformed by 9 sample points which are evenly distributed. The design spaces for both the power and drag coefficients at each of the $C_{\mu B}$ levels were assumed to be continuous, and have been represented using surrogate models. These response surfaces have been generated using GPR techniques, and a square exponential kernel was chosen to build the surrogate models [26]. The open source python library Scikit-learn [72] implementation of this technique was used to generate the response surfaces and the resulting design space representations can be seen in Figure 4.16.

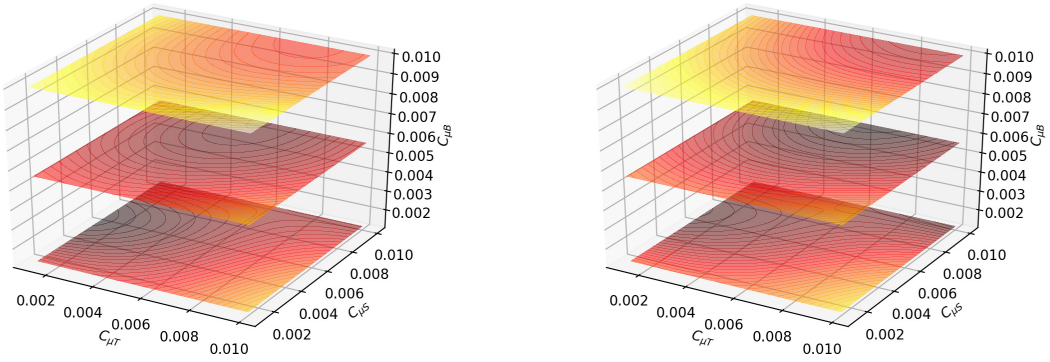

(a) Design Space - C_{Pow}

(b) Design Space - C_D

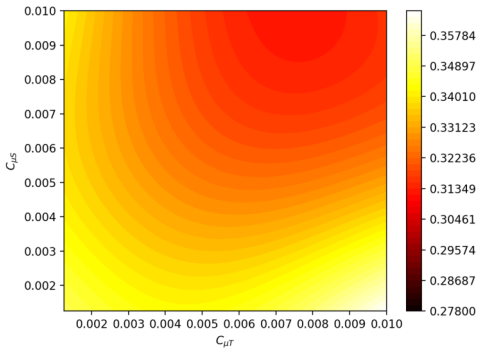

(c) $C_{\mu B} = 0.01$

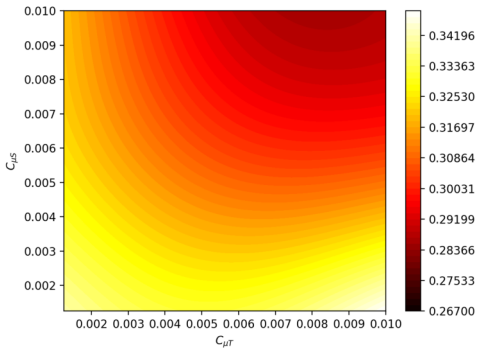

(d) $C_{\mu B} = 0.01$

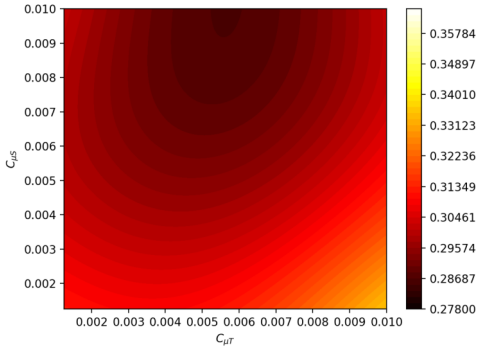

(e) $C_{\mu B} = 0.005625$

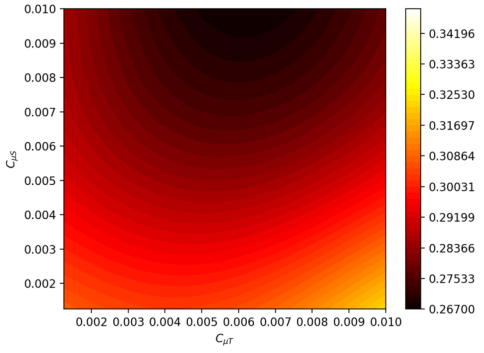

(f) $C_{\mu B} = 0.005625$

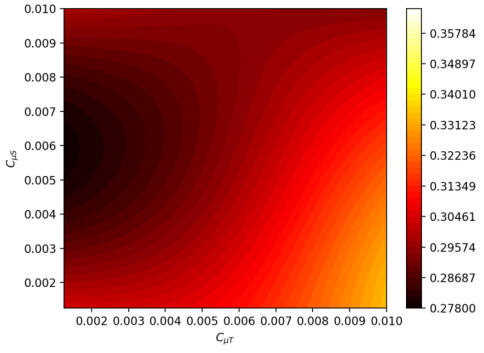

(g) $C_{\mu B} = 0.00125$

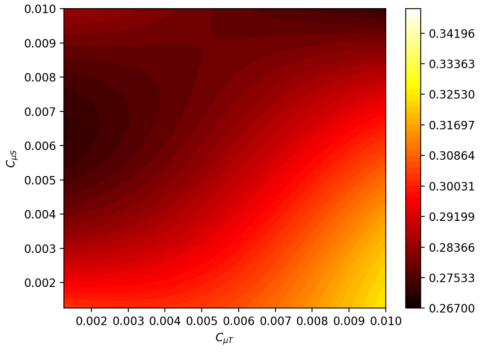

(h) $C_{\mu B} = 0.00125$

Figure 4.16: Surrogate models of the power coefficient in the left column (a, c, e, g) and the drag coefficient in the right column (b, d, f, h) for the full-factorial study at different bottom jet momentum coefficient values.

$Case$ [−]	$C_{\mu B}$ [−]	$V_{PBottom}$ [$\frac{m}{s}$]	$C_{\mu T}$ [−]	V_{PTop} [$\frac{m}{s}$]	$C_{\mu S}$ [−]	V_{PSide} [$\frac{m}{s}$]	C_D [−]	C_{Pow} [−]
1	0.001250	20.8997	0.001250	20.8997	0.001250	16.8732	0.3032	0.3044
2	0.001250	20.8997	0.001250	20.8997	0.005625	35.7443	0.2727	0.2788
3	0.001250	20.8997	0.001250	20.8997	0.010000	47.6366	0.2852	0.2987
4	0.001250	20.8997	0.005625	44.2461	0.001250	16.8732	0.3053	0.3095
5	0.001250	20.8997	0.005625	44.2461	0.005625	35.7443	0.2856	0.2947
6	0.001250	20.8997	0.005625	44.2461	0.010000	47.6366	0.2781	0.2945
7	0.001250	20.8997	0.010000	58.9541	0.001250	16.8732	0.3252	0.3340
8	0.001250	20.8997	0.010000	58.9541	0.005625	35.7443	0.3060	0.3196
9	0.001250	20.8997	0.010000	58.9541	0.010000	47.6366	0.2726	0.2936
10	0.005625	44.2461	0.001250	20.8997	0.001250	16.8732	0.3078	0.3121
11	0.005625	44.2461	0.001250	20.8997	0.005625	35.7443	0.2907	0.2998
12	0.005625	44.2461	0.001250	20.8997	0.010000	47.6366	0.2857	0.3021
13	0.005625	44.2461	0.005625	44.2461	0.001250	16.8732	0.3050	0.3122
14	0.005625	44.2461	0.005625	44.2461	0.005625	35.7443	0.2806	0.2926
15	0.005625	44.2461	0.005625	44.2461	0.010000	47.6366	0.2673	0.2867
16	0.005625	44.2461	0.010000	58.9541	0.001250	16.8732	0.3233	0.3351
17	0.005625	44.2461	0.010000	58.9541	0.005625	35.7443	0.2919	0.3085
18	0.005625	44.2461	0.010000	58.9541	0.010000	47.6366	0.2777	0.3017
19	0.010000	58.9541	0.001250	20.8997	0.001250	16.8732	0.3411	0.3499
20	0.010000	58.9541	0.001250	20.8997	0.005625	35.7443	0.3251	0.3387
21	0.010000	58.9541	0.001250	20.8997	0.010000	47.6366	0.3200	0.3410
22	0.010000	58.9541	0.005625	44.2461	0.001250	16.8732	0.3319	0.3437
23	0.010000	58.9541	0.005625	44.2461	0.005625	35.7443	0.3063	0.3229
24	0.010000	58.9541	0.005625	44.2461	0.010000	47.6366	0.2910	0.3150
25	0.010000	58.9541	0.010000	58.9541	0.001250	16.8732	0.3486	0.3649
26	0.010000	58.9541	0.010000	58.9541	0.005625	35.7443	0.3056	0.3267
27	0.010000	58.9541	0.010000	58.9541	0.010000	47.6366	0.2874	0.3159

Table 4.5: Blowing strength configurations and resulting drag and power coefficients for the full-factorial study of a GTS model outfitted with the AFC system. $C_{\mu B}$ is the bottom jet momentum coefficient, $V_{PBottom}$ is the peak velocity on the bottom jet, $C_{\mu T}$ is the top jet momentum coefficient, V_{PTop} is the peak velocity on the top jet, $C_{\mu S}$ is the momentum coefficient on each of the side jets, V_{PSide} is the peak velocity on each of the side jets, C_D is the drag coefficient and C_{Pow} is the power coefficient.

In order to better understand the physical changes of the wake, and the overall vehicle aerodynamic behavior, two-dimensional cuts of the flow behind the GTS were examined. Using the same slice locations as in the previous study, the wake structure was analyzed. Figure 4.17 shows the slice locations for the GTS model outfitted with the AFC system.

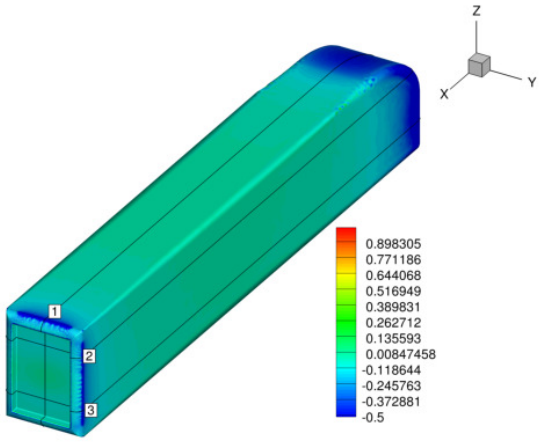

Figure 4.17: Location of the slices used to study the wake of a GTS model outfitted with a Coanda based AFC system. (1) is a vertical slice located at $y/W = 0$, (2) is a horizontal slice located at $z/W = 1.05$ and (3) is a horizontal slice placed at $z/W = 0.35$. Pressure coefficient is shown in the vehicle's surface.

Starting from Figures 4.16c and 4.16d, it is clear that the power consumption of the system, and the drag generated by the vehicle, are at the highest levels when the bottom jet operates at full strength and is trying to counteract the ground effect. Case 25 exhibits the highest power and drag coefficients with values of 0.3649 and 0.3486 respectively. This configuration was obtained by blowing the top and bottom jets at full strength ($C_\mu = 0.01$), while the side jets were operated at the minimum strength ($C_\mu = 0.00125$). The bottom jet propels the flow from under the body upwards and shifts the wake's tail above the vertical centerline. At the mean time, the top jet attempts to push the wake back down, but due to its interaction with the external flow coming from the top of the vehicle, the top jet effect on the wake is further downstream. The interaction between the top and bottom jets gives rise to an asymmetric pair of counter rotating horizontal vortices that are pushed towards the back of the truck, as can be seen in Figure 4.18b. The overwhelming effect of the top and bottom jets can be better appreciated by looking at the normalized ground-normal velocity magnitude in Figures 4.18c and 4.18d. Furthermore, these Figures show a pair of vertical counter rotating vortices that span the height of the GTS model and have been forced outside of the top and bottom jet's influence region. The side jets struggle to constrain the position of these vortical structures and allow a thick wake to form. The position of these vortices gives rise to intermittent

smaller vortices in the back of the truck, and their interaction causes a low and asymmetric back pressure distribution, as can be seen in Figure 4.18a.

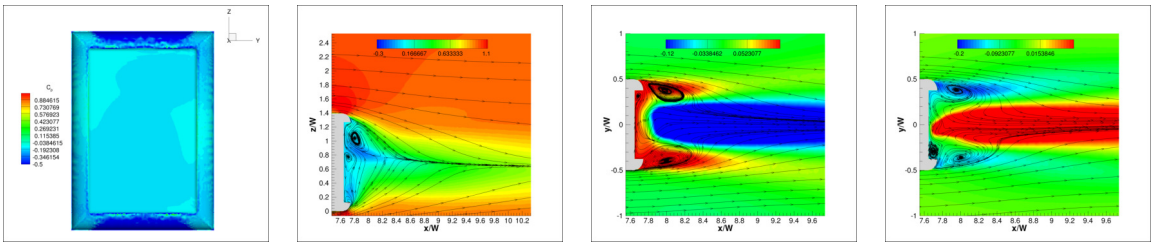

(a) (b) (c) (d)

Figure 4.18: Wake structure and pressure distribution of the flow triggered by the blowing configuration of case 25. (a) shows the back pressure coefficient, (b) is slice 1 showing a contour of the normalized stream-wise velocity, (c) is slice 2 showing a contour of the normalized ground-normal velocity, and (d) is slice 3 showing a contour of the normalized ground-normal velocity.

To reduce the effect of the vertical vortices in case 25, the blowing strength of the side jets has been increased to its maximum setting. This configuration is represented in case 27, were both the power and drag coefficients decreased to 0.3159 and 0.2874 respectively. In this configuration the wake is fully restrained, and its behavior is driven by the top and bottom jets, which establish a pair of counter-rotating horizontal vortices. The introduction of high-momentum flow from the side jets constrains the wake laterally and influences the ground-normal behavior by giving it a quasi-symmetric structure, as can be seen in Figure 4.19b.

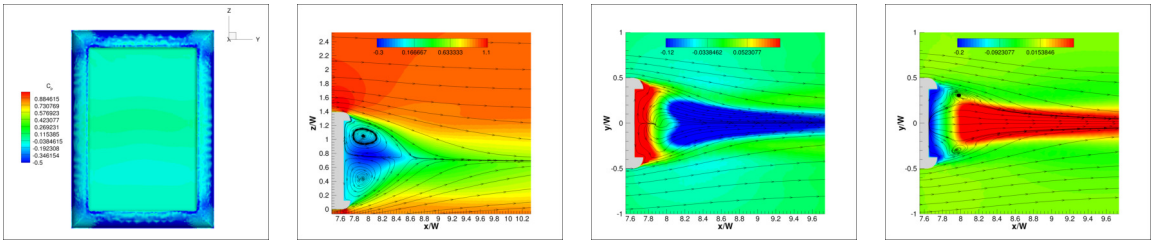

(a) (b) (c) (d)

Figure 4.19: Wake structure and pressure distribution of the flow triggered by the blowing configuration of case 27. (a) shows the back pressure coefficient, (b) is slice 1 showing a contour of the normalized stream-wise velocity, (c) is slice 2 showing a contour of the normalized ground-normal velocity, and (d) is slice 3 showing a contour of the normalized ground-normal velocity.

Furthermore, the side jets significantly decrease the presence of vertical vortices, as shown in Figures 4.19c and 4.19d, and allow for a significant increase of the back pressure, shown in Figure 4.19a. The presence for high momentum jet flow in this configuration counteracts the pressure increase in the back of the vehicle, by inducing low-pressures in the Coanda surfaces, which despite

the aerodynamic improvements in the wake causes the drag to stagnate. The power required to energize the AFC system in this configuration is significantly higher and its power signature drives the system behavior despite the drag improvements.

By reducing the strength of the bottom and top jets to the mid-level ($C_\mu = 0.005625$), while maintaining the side jets at a high blowing strength, the GTS drag and power coefficients decrease. Case 15 uses this configuration and, as can be seen in Figures 4.20b, 4.20c, and 4.20d, the dominance of the horizontal vortices is decreased as the vertical vortices reappear. The recirculating nature of the wake is represented as a torus of revolution with a coplanar axis positioned parallel to the flow stream direction and normal to the back of the GTS. The bottom jet counteracts the ground effect and pushes the wake's tail closer to the centerline. This wake structure significantly increases the pressure in the back face of the GTS, as can be seen in Figure 4.20a, and the drag coefficient obtained is the global minimum with a value of 0.2673. The power coefficient required to maintain this wake configuration is 0.2867.

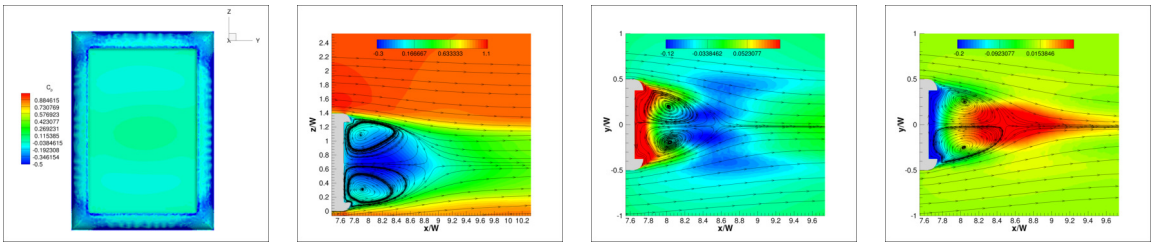

(a) (b) (c) (d)

Figure 4.20: Wake structure and pressure distribution of the flow triggered by the blowing configuration of case 15. (a) shows the back pressure coefficient, (b) is slice 1 showing a contour of the normalized stream-wise velocity, (c) is slice 2 showing a contour of the normalized ground-normal velocity, and (d) is slice 3 showing a contour of the normalized ground-normal velocity.

Although case 15 represented the minimum drag coefficient in the study, the minimum power coefficient was achieved in case 2, where the top and bottom jets are blowing at the minimum momentum coefficient, and the side jets at the mid-level. This case is analogous to case 15 but at a lower blowing level for all jets. The wake behavior under this blowing configuration is similar to the one described in case 15, were both horizontal and vertical vortices interact and behave as a torus of revolution. The tail of the wake is closer to the ground since the bottom jet is doing less work against the ground effect, which introduces a slight vertical asymmetry and can be seen in Figure 4.21b. In addition, the wake is longer in this configuration and, due to the lower overall momentum coefficient, is wider and allows for a lower back pressure, when compared to case 15, as can be clearly seen in Figures 4.21a, 4.21c and 4.21d. The reduced jet velocity contributes to the presence of higher pressure in the Coanda surfaces, preventing a sharp increase in drag, and requires less power to energize the system, which makes this configuration the most power efficient in this

study. The power and drag coefficients for this configuration are 0.2788 and 0.2727 respectively, which compared to the base GTS model power coefficient of 0.3323 [54] produce an improvement of 16.1% in power consumption.

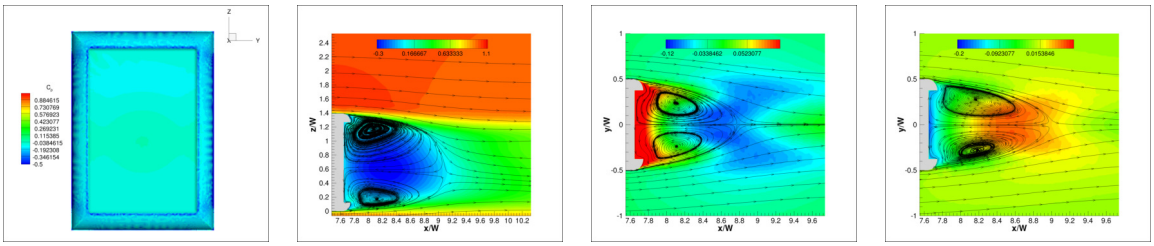

(a) (b) (c) (d)

Figure 4.21: Wake structure and pressure distribution of the flow triggered by the blowing configuration of case 2. (a) shows the back pressure coefficient, (b) is slice 1 showing a contour of the normalized stream-wise velocity, (c) is slice 2 showing a contour of the normalized ground-normal velocity, and (d) is slice 3 showing a contour of the normalized ground-normal velocity.

4.3.3 Conclusion

This Chapter described the aerodynamic profile of the GTS model and studied the use of RANS to simulate airflow around this geometry to obtaining the integrated forces acting on it. This apporach was validated, for design purposes, by comparing the obtained integrated forces and wake structure with those available in the literature [89, 81, 23]. To reduce the computational resources require to study the effects of using AFC systems, the capability of specifying velocity profiles as inlets was implemented in SU2. With this capability in place, a velocity profile was built by using previous two-dimensional aerodynamic studies of the AFC system, and boundary layer theory to extend it in the third dimension.

In the first section of this Chapter, a parametric study was performed, and surrogate models were used to represent the power and drag behavior as a function of the momentum coefficient for the GTS model outfitted with the AFC system. The parametric study imposed equal momentum coefficients for all jets, which were allowed to vary between 0 and 0.01223 per jet, or 0 and 0.04892 cumulatively. The configuration that uses the minimum amount of power was identified using a GPR driven surrogate model. At this configuration drag was reduced by 15% and power consumption by 12%.

The wake structure of the minimum power configuration was compared to the base GTS wake structure, and the mechanisms for achieving drag reduction were identified. Finally, the pressure distribution on the back face of the vehicle for various levels of blowing using the AFC system, as well as the base GTS model were compared.

To better understand the system's influence on the power consumption and vehicle's aerodynamic drag, jet specific momentum coefficients were used in the second part of this Chapter. Due to

symmetry the port and starboard jets were controlled together, while the top and bottom jets were allowed to vary separately.

To span the design space, a full-factorial study using 27 sampling configurations was used. The jet specific momentum coefficients were allowed to vary between 0.00125, 0.005625, and 0.01; and all combinations of these parameters were studied. The drag and power consumption resulting from these simulations were visualized by dividing the data set into 3 groups of 9 function evaluations each, where the bottom jet momentum coefficient was kept constant, and surrogate models of each group were generated using GPR methods.

Using the surrogate models to guide the exploration, four cases were selected to highlight the effect the AFC system had in the wake structure and performance of the vehicle. In case 25, the jets manipulate the wake to increase the drag of the vehicle by making the wake unstable. Although this behavior is consistent with the results reported in the literature [55, 56, 23], an accurate simulation of this configuration using unsteady methods is required. The configuration used in Case 27 increases the side jet air injection strength to restrain the wake and improve its stability, but a combination of low Coanda surface pressure and high power consumption guide the selection to a more conservative blowing approach. Case 15 is shown to restrain the wake and is able to reduce drag by 19.6%, which gives the minimum drag value for this section and Chapter. This configuration requires a significant amount of blowing and therefore a compromise on drag is required to find the minimum power consumption configuration. Case 2 is a low-blowing analogous of case 15, where the wake is controlled in a similar manner, but by compromising in drag minimization, it achieves the minimum power usage seen in this study with a 16.1% power and 17.9% drag reduction.

This Chapter has shown the importance blowing strength and jet configuration have in the aerodynamic and power behavior of the vehicle. It is clear that a trade-off exists between the increase in base face pressure and a decrease in Coanda surface pressure, which provides a physical interpretation of the drag and power behavior of the system.

Chapter 5

Grid Refinement Studies

In the study of heavy vehicle aerodynamics, particular attention has been placed in regions which hold the potential to change the vehicle aerodynamic profile and behavior. Chapter 1 presents a detailed description of the flow features around heavy vehicles, and this Chapter will focus specifically in the aerodynamic behavior of the Ground Transportation System (GTS) model, which is a simplified and clean geometry used mainly to study the wake and its effect in the power and aerodynamic response of the vehicle.

In this chapter the changes in pressure distribution and the flow features that contribute to it are analyzed as the mesh resolution is changed. Particular focus has been placed in the effect these changes have in the integrated force behavior, pressure distribution, and how each section of the vehicle contribute to the overall drag. Finally, this Chapter evaluates the drag changes at each resolution level due to the introduction of the Active Flow Control (AFC) system and its comparison to the base GTS.

5.1 Computational Grids

The computational grids used to represent the base and Coanda jet-equipped GTS models are fully unstructured with mixed element types. On each of these meshes the surface is modeled using triangles, the boundary layer region is represented by prisms while the rest of the mesh is composed of tetrahedra. For this study, the coarse mesh for the base GTS model was generated using $2,715,771$ points and $13,131,248$ cells. The surface grid that represents the GTS model can be seen in Figure 5.1.

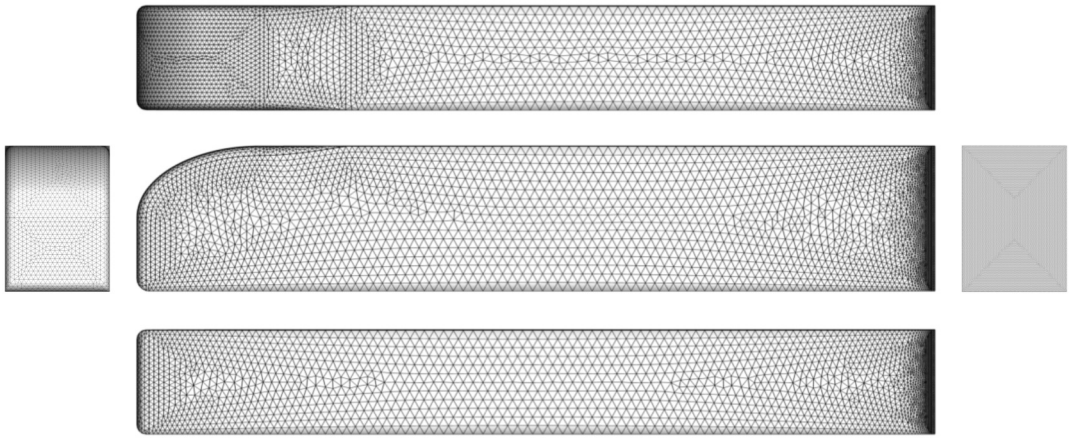

Figure 5.1: Coarse level surface grid of the base GTS model.

In the development if this mesh, extra resolution was placed in regions of high curvature, the region closer to the sharp edges in the back, and the back itself. This increase in resolution was driven by the presence of flow and surface pressure gradients. These regions are of particular interest to model the flow past the vehicle and to understand the effect each of them has in the overall integrated forces.

Since the flow over the vehicle travels its entire length, the Reynolds number used to construct the viscous mesh was based on the length of the vehicle, and was found to be 2.759 million. Using this approach to build the coarse level mesh, a y+ set to 0.99 was used. The volume mesh, which can be seen in Figure 5.2, was built to increase its resolution closer to the vehicle and to expand quickly towards the far-field. The far-field boundary of the domain is located in the axial direction at 5 truck lengths from the front and 9 truck lengths from the back. In the direction perpendicular to the flow, the vehicle is centered within 11 truck lengths, and in the direction normal to the ground, the domain spans 5 truck lengths.

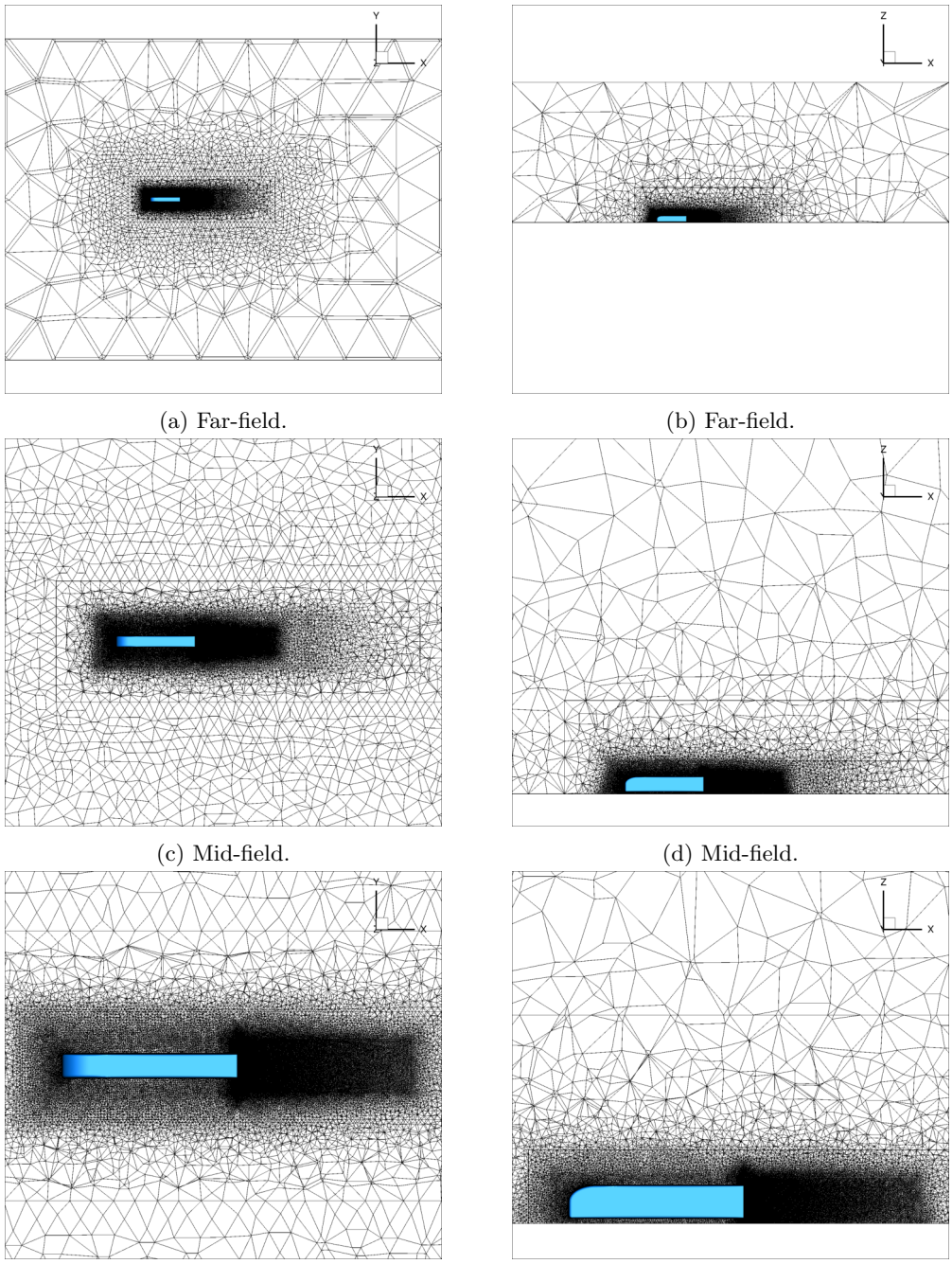

(a) Far-field. (b) Far-field.

(c) Mid-field. (d) Mid-field.

(e) Near-field. (f) Near-field.

Figure 5.2: Coarse level volume grid of the base GTS model. (a), (c), and (e) show the top view perspective of a grid slice located at 0.1 m from the bottom of the vehicle. (b),(d), and (f) show the side view perspective of a grid slice located a the center plane of the vehicle.

In the GTS model, and other flat back vehicles, viscous pressure drag is caused by flow separation in the back. To capture the flow physics and its effect in the pressure signature of the vehicle, the mesh resolution was increased in the surface mesh representing the back of the vehicle, and a high resolution volume region directly behind the vehicle was introduced. A close up of the mesh at the rear side of the vehicle can be seen in Figure 5.3.

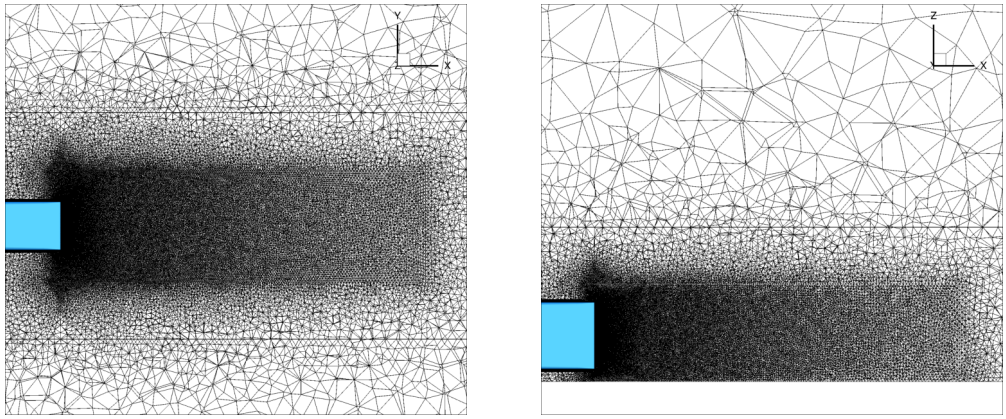

(a) Top view. (b) Side view.

Figure 5.3: Coarse level volume grid of the wake region behind the base GTS model. (a) shows the top view perspective of a grid slice located at 0.1 m from the bottom of the vehicle, and (b) shows the side view perspective of a grid slice located a the center plane of the vehicle.

To maintain consistency for each mesh resolution level, every mesh was build using a modular approach, where the far-field, and mid-field remained the same for the base and enhanced models, and the near-field was updated to accommodate for the introduction of the AFC system. This approach allowed for both meshes to have a similar topology away from the vehicle.

The enhanced model was built by mounting the AFC system to the back of the base GTS. This add-on system introduces changes in the back portion of the vehicle, but allows the front to remain unchanged. The surface mesh for the GTS model outfitted with the AFC system in the back was generated using $3,756,261$ points and $15,125,985$ cells and the same y+ as the base GTS was used. This surface grid is shown in Figure 5.4.

The increase in resolution towards the back of the vehicle was used to maintain a smooth area change between the cells representing the tailer region, and the cells modeling the curvature of the Coanda surfaces. Furthermore, the volumetric grid used to capture the boundary layer was modified to follow the curvature of the AFC system, and to accommodate for the introduction of air in the back, as can be seen in Figure 5.5.

Starting from these two meshes, a family of grids was created where the resolution was homogeneously increased over the entire domain. To maintain the mesh topology unchanged a script

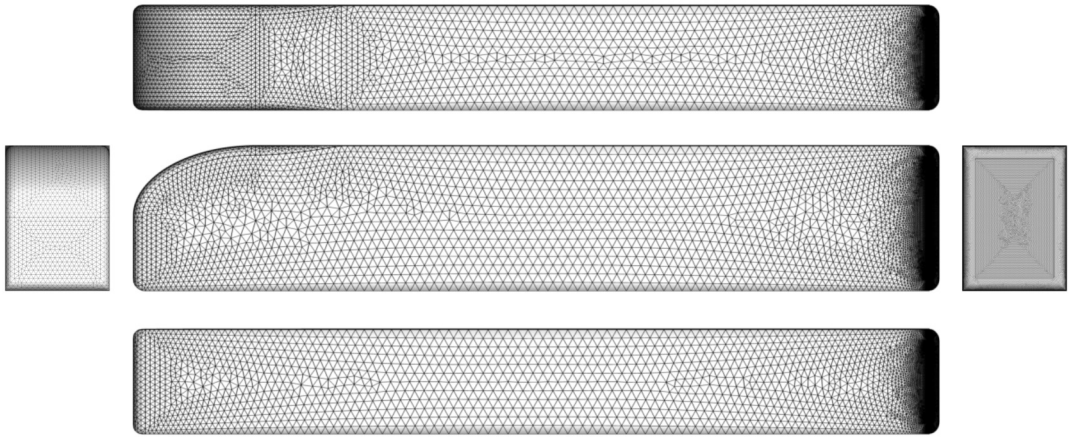

Figure 5.4: Coarse level surface grid of the GTS model outfitted with the AFC system.

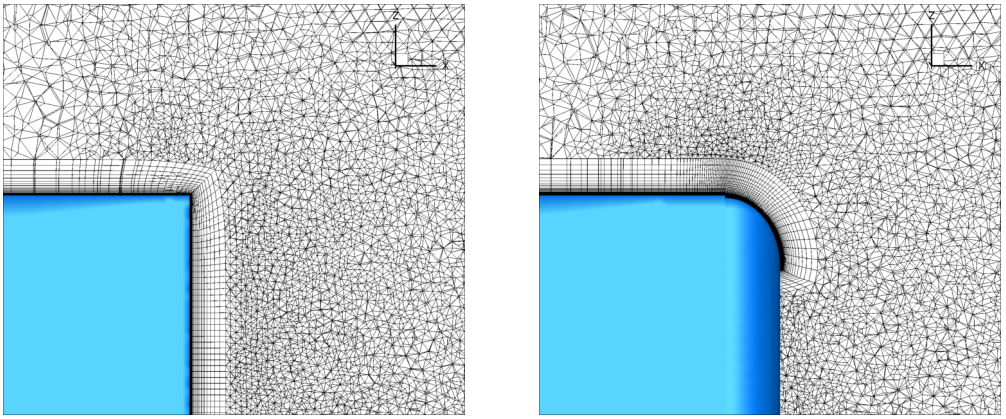

(a) Base GTS. (b) GTS outfitted with the AFC system.

Figure 5.5: Side view slice located at the center plane of the vehicle of the Coarse level grid used to capture the boundary layer behavior in the back of the vehicle.

developed by Pointwise [1] was used.

Each resolution level was designed to have twice the number of points as the previous one, and therefore a two-step approach was used. First, the Pointwise script was used to homogeneously refine the grid by increasing the number of points in each connector by a user specified refinement factor. This step allowed for the quick refinement of the entire mesh at once. To guarantee that the areas of interest have the proper resolution, a second step with visual inspection and targeted refinement was introduced. The targeted areas include the curved surfaces leading away from the front, and the flat domains that connect to the back. The latter region was targeted to guarantee a smooth area transition both from the curved regions in the front, and to the flat back. Figures 5.6 and 5.7 show the surface mesh for the middle level mesh representing the GTS model with and without the AFC system attached to its back.

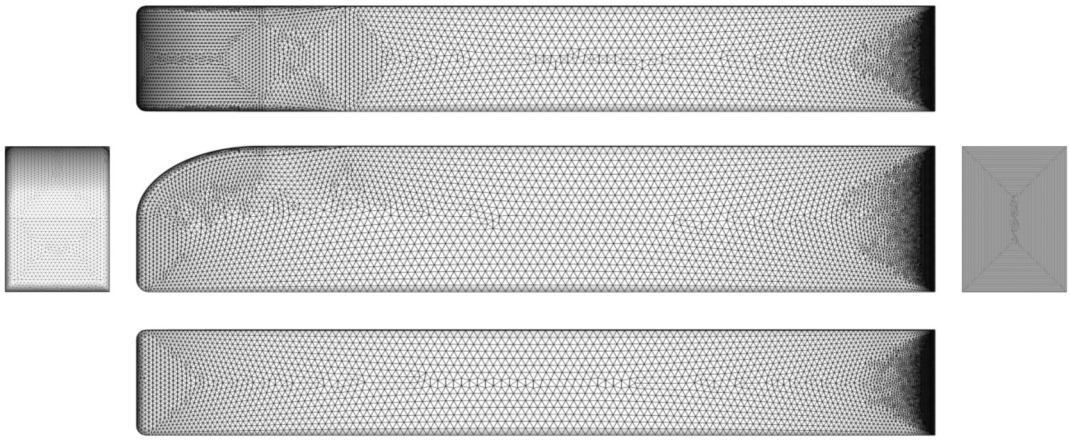

Figure 5.6: Mid level surface grid of the base GTS model.

The base GTS model mesh shown in Figure 5.6 was generated using $5,071,479$ points, $25,035,583$ cells, and a y+ of 0.78. The mesh representing the GTS outfitted with the AFC system is shown in Figure 5.7 and was generated using $6,787,982$ points, $28,037,812$ cells, and the same y+ as in the base model. The volume grid for this resolution level can be seen in Appendix A.2.

[1] https://github.com/pointwise/GridRefine

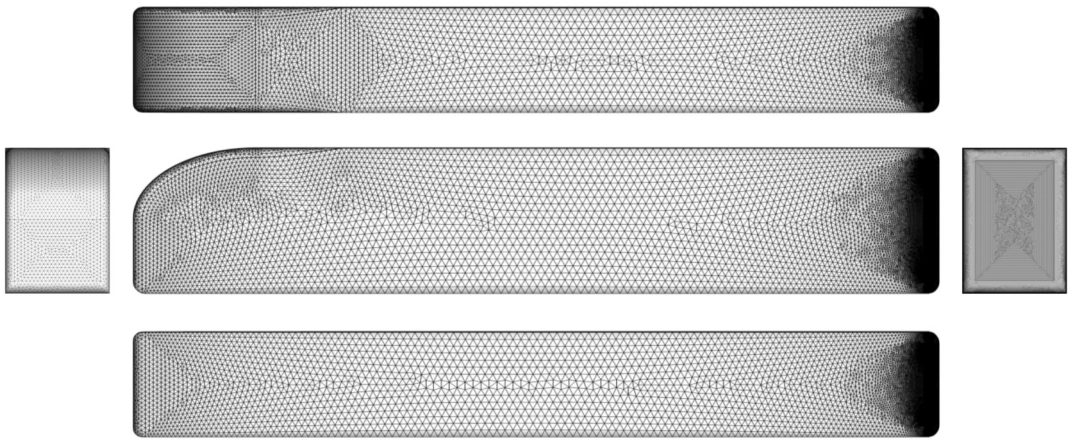

Figure 5.7: Mid level surface grid of the GTS model outfitted with the AFC system.

The same approach used to generate the mid level mesh was used to generate the fine level set of grids. The surface mesh for the base GTS model is shown in Figure 5.8. This grid was generated using $9,618,049$ points, $49,340,375$ cells, and a y+ of 0.58.

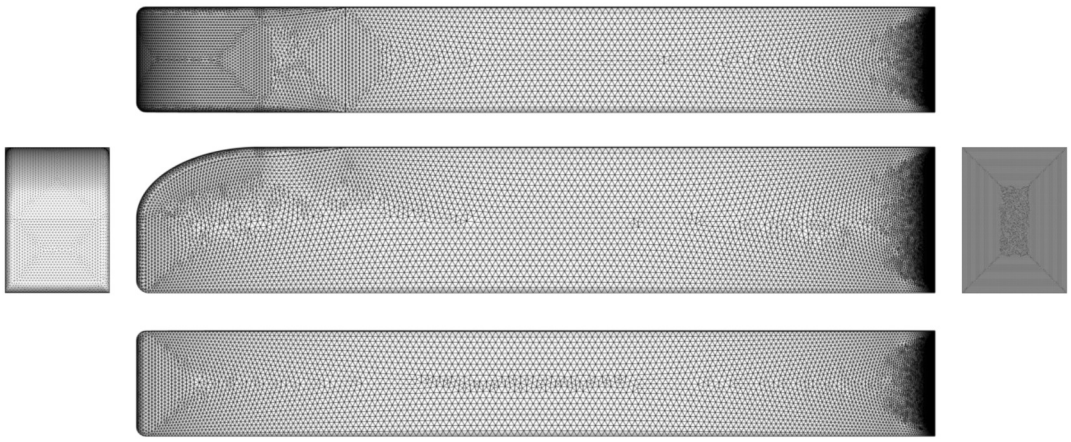

Figure 5.8: Fine level surface grid of the base GTS model.

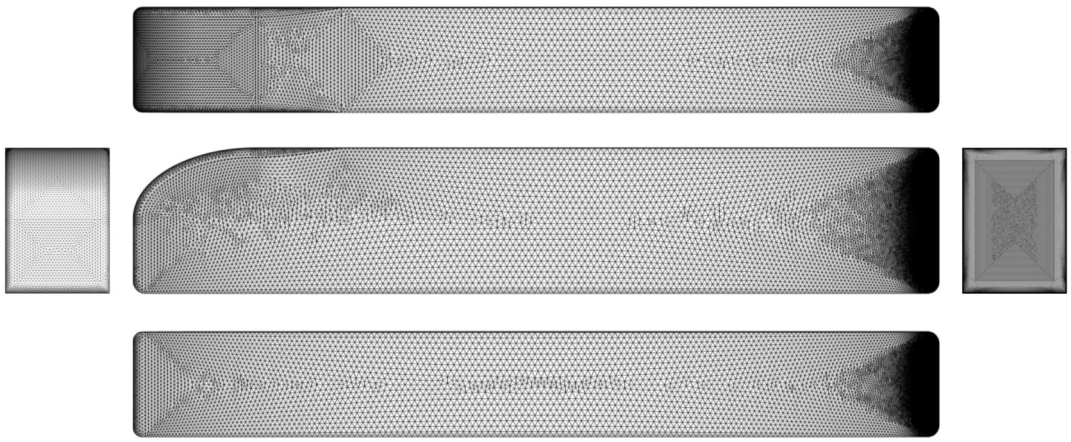

Figure 5.9: Fine level surface grid of the GTS model outfitted with the AFC system.

The surface mesh for the GTS outfitted with the AFC system is shown in Figure 5.9 and was generated using $13,180,154$ points, $56,349,134$ cells, and the same y+ as in the base model. The volume grid for the base GTS at this resolution level can be seen in Appendix A.3.

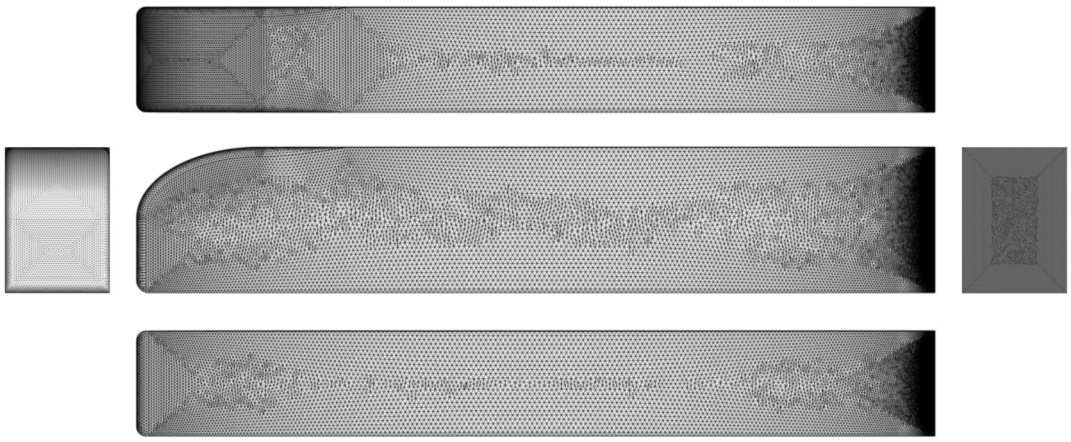

Figure 5.10: Extra fine level surface grid of the base GTS model.

Finally, one more level of refinement was introduced and named Extra Fine. These computational grids where created following the same two step approach and the surface meshes fo both the base GTS and the enhanced model can be see in Figures 5.10 and 5.11.

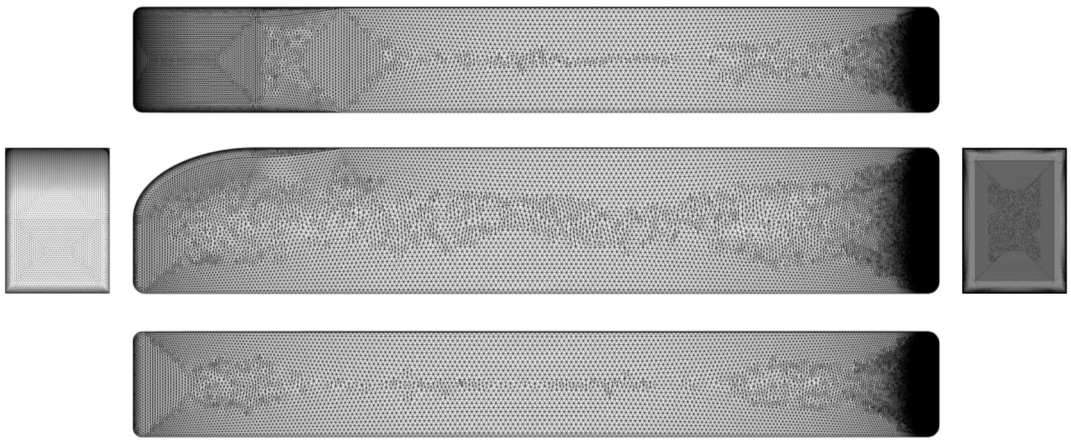

Figure 5.11: Extra fine level surface grid of the GTS model outfitted with the AFC system.

The viscous layer of the extra fine resolution grid was generated using a y+ of 0.47. The base GTS model was represented using $19,001,977$ points and $99,728,355$ cells, and the model outfitted with the Coanda jet-based system was represented using $25,357,242$ points, $110,853,184$ cells. The volume grid for the base GTS at this resolution level can be seen in Appendix A.4.

In addition to tracking the number of points and cells in the computational grids used in this Chapter, the Back Cell Size has been recorded. This feature has been selected as a metric of resolution, since it represents the smallest features that can be captured in the back of the vehicle. A summary of the meshes used in this Chapter can be found in Table 5.1.

Geometry	***Points***	***Cells***	***Back Cell Size***	***y+***
Base GTS	$2,715,771$	$13,131,248$	$2.0000e-03$	0.99
Base GTS	$5,071,479$	$25,035,583$	$1.5800e-03$	0.78
Base GTS	$9,618,049$	$49,340,375$	$1.2300e-03$	0.58
Base GTS	$19,001,977$	$99,728,355$	$9.5600e-04$	0.47
Enhanced GTS	$3,756,261$	$15,125,985$	$1.9818e-03$	0.99
Enhanced GTS	$6,787,982$	$28,037,812$	$1.5855e-03$	0.78
Enhanced GTS	$10,959,124$	$43,251,615$	$1.2435e-03$	0.58
Enhanced GTS	$25,357,242$	$110,853,184$	$9.5600e-04$	0.47

Table 5.1: Summary of the family of meshes used to study the effects of mesh resolution in the GTS model with and without the AFC system.

5.2 Flow Features

The flow around the vehicle was simulated using standard air at sea-level treated as a calorically perfect ideal gas. The velocity was set to 31.3 m/s (70 mph) which translates to a Mach number of 0.09195 and Reynolds number, using the GTS model width as the length scale, of $359,900$.

To remain consistent with the results obtained in Chapter 4, the simulations were performed using the steady compressible solver in SU2 [20, 70, 69] with a combination of Jameson-Schmidt-Turkel (JST) numerical scheme [42] and Shear-Stress-Transport (SST) turbulence model [62]. The vehicle surface has been treated using an adiabatic no-slip condition, the outer domain boundaries are treated with the typical characteristic-based far-field condition for external aerodynamics, and the ground plane is modeled using a slip condition, to avoid influencing the solution with the presence of a boundary layer.

To quantify the effect of mesh resolution, the integrated forces were monitored using the drag coefficient, which has been defined in Equations 4.4. In addition to the integrated forces, special emphasis has been placed in the pressure distribution in the surface of the vehicle, for which the pressure coefficient has been defined as:

$$C_P = \frac{P - P_\infty}{q}, \tag{5.1}$$

where, C_P is the pressure coefficient, P is the local static pressure, P_∞ is the free-stream static pressure, q is the dynamic pressure calculated as $\frac{1}{2}\rho_\infty U_\infty^2$, ρ_∞ is the free-stream density, and U_∞ the free-stream velocity.

5.3 Base Ground Transportation System

On average the GTS model achieved 6 orders of magnitude of convergence across every mesh level used, ranging from 5.5 in the Extra Fine mesh to 6.6 orders of magnitude in the Coarse mesh. The drag coefficient for this vehicle decreased from 0.3372 to 0.2924 as the mesh resolution went from 2.7 million points to 19 million points. Since the majority of drag in the GTS model comes from pressure drag, the analysis of the changes in pressure start by looking at Figure 5.12, which shows the pressure coefficient contour in the front of the vehicle at every mesh level.

As the mesh resolution increases, the stagnation region becomes better defined and the high-pressure center rounder, smaller, and sharper. This region morphs into a more defined square and the pressure recovery, which takes place as the flow moves away from the center, is smoother. The low-pressure expansion regions in the left and right edges thicken and grow towards the top of the vehicle. The bottom edge continues to show the low-pressure effects of flow expansion, and as mesh resolution increases, it increases its effect towards the center. Finally, as the bottom left and right corners are refined, the surface mesh is able to better represent the rounded nature of this geometry

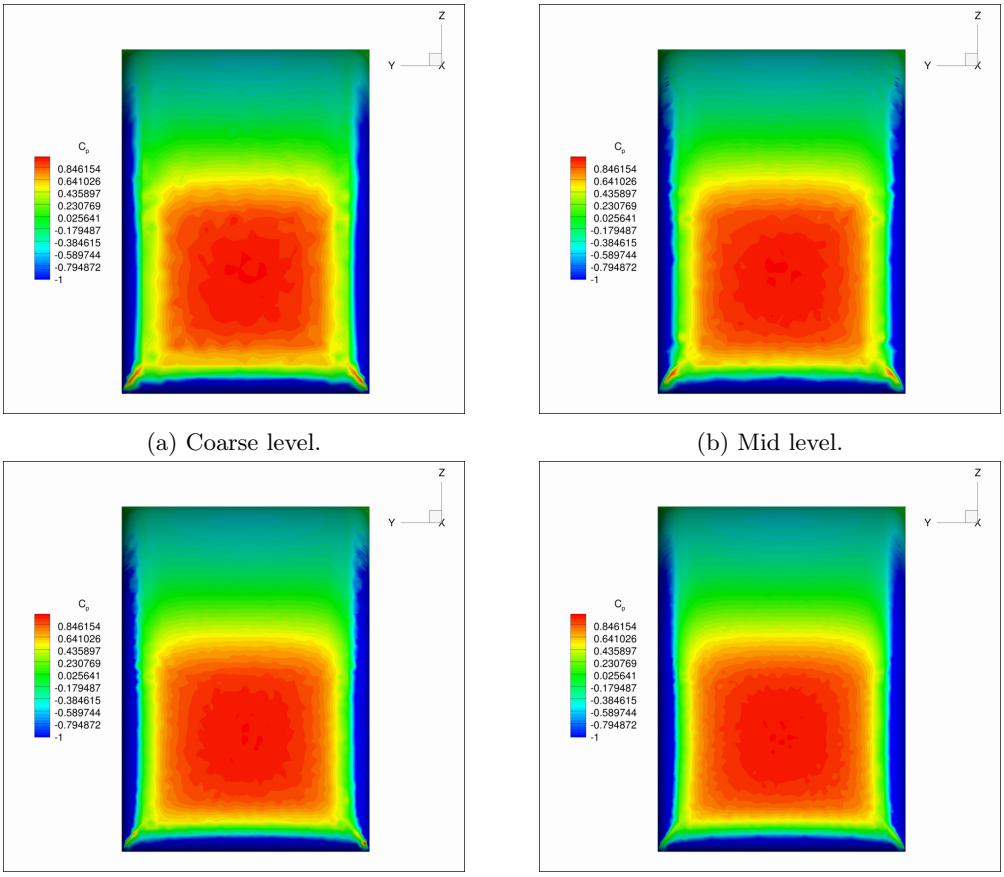

(a) Coarse level.

(b) Mid level.

(c) Fine level.

(d) Extra fine level.

Figure 5.12: Pressure distribution in the front of the GTS model at different mesh resolutions.

and the existence of high pressure stagnation points in these regions are significantly reduced. The pressure contour changes in this region of the vehicle lead to a sharp drop in its contribution the overall vehicle drag, as can be seen in Table 5.2.

Mesh Level	C_D	$C_{D\ Pressure}$	$C_{D\ Friction}$	$C_{D\ Front}$	$C_{D\ Back}$
Coarse	0.3372	0.2557	0.0815	0.0745	0.1812
Mid	0.3304	0.2481	0.0823	0.0739	0.1742
Fine	0.3089	0.2228	0.0861	0.0522	0.1706
Extra Fine	0.2924	0.2038	0.0886	0.0366	0.1672

Table 5.2: Drag breakdown for the base GTS model. C_D is the vehicle drag coefficient, $C_{D\ Pressure}$ is the pressure contribution to drag, $C_{D\ Friction}$ is the viscous friction contribution to drag, $C_{D\ Front}$ is the pressure contribution to drag from the front of the vehicle, and $C_{D\ Back}$ is the pressure contribution to drag from the back of the vehicle.

In addition to the pressure distribution in the front of the vehicle, the flow features surrounding this area have been analyzed. As can be seen from Figure 5.13 the flow patterns around the vehicle are consistent for all grid levels and no discernible difference has been found.

The main contributor to the drag of the GTS model is the back of the vehicle. Due to the sharp corners it causes the flow to separate and develop a wake with recirculating flow within, as has been explained in detail in the previous chapters. The flow patterns in the back of the vehicle are shown in Figure 5.14.

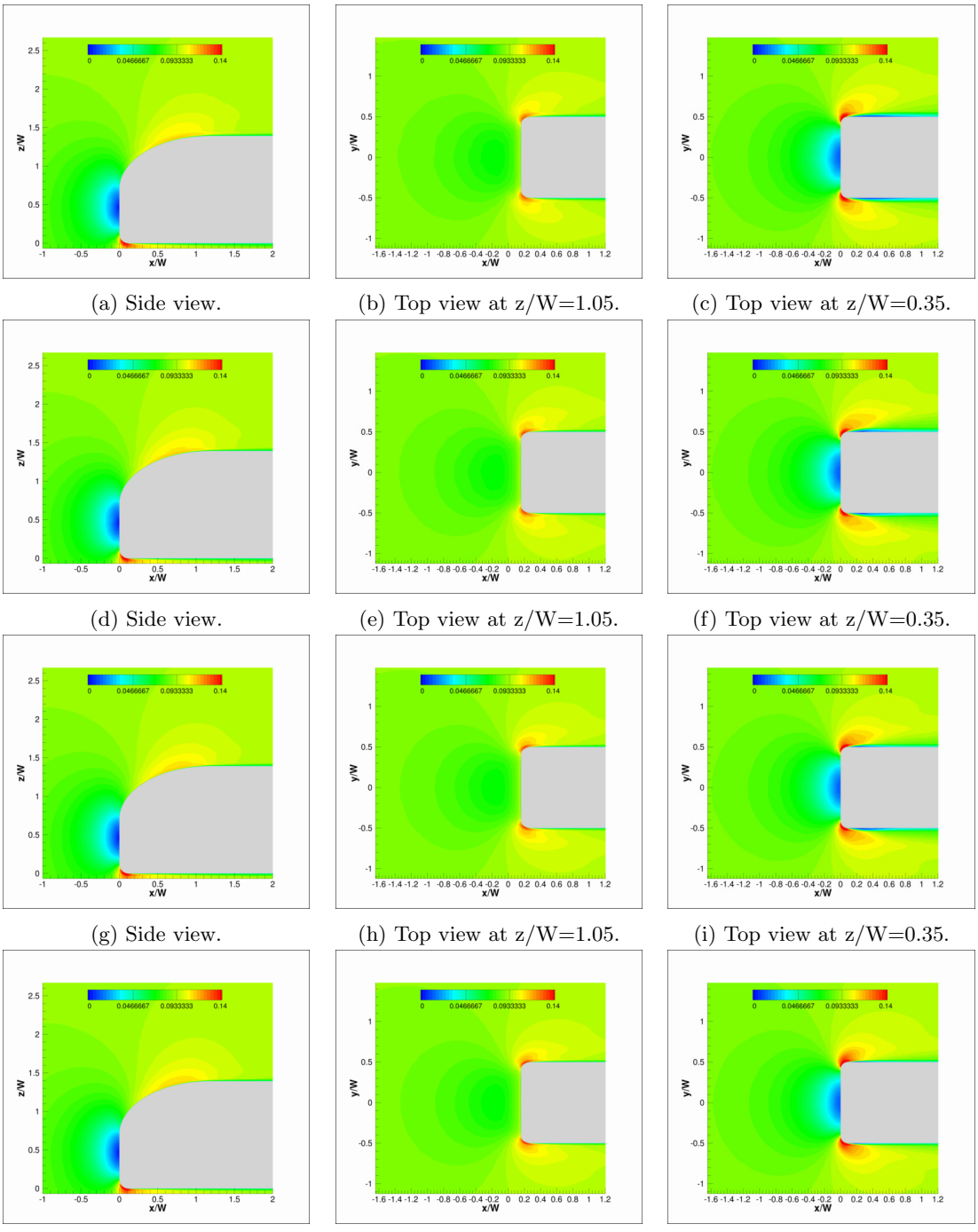

(a) Side view. (b) Top view at z/W=1.05. (c) Top view at z/W=0.35.

(d) Side view. (e) Top view at z/W=1.05. (f) Top view at z/W=0.35.

(g) Side view. (h) Top view at z/W=1.05. (i) Top view at z/W=0.35.

(j) Side view. (k) Top view at z/W=1.05. (l) Top view at z/W=0.35.

Figure 5.13: Mach number contours to visualize the flow structures in front of the base GTS model at different mesh resolutions. (a), (b), and (c) used the coarse level mesh, (d), (e), and (f) used the mid level mesh, (g), (h), and (i) used the fine level mesh, and (j), (k), and (l) used the extra fine level mesh.

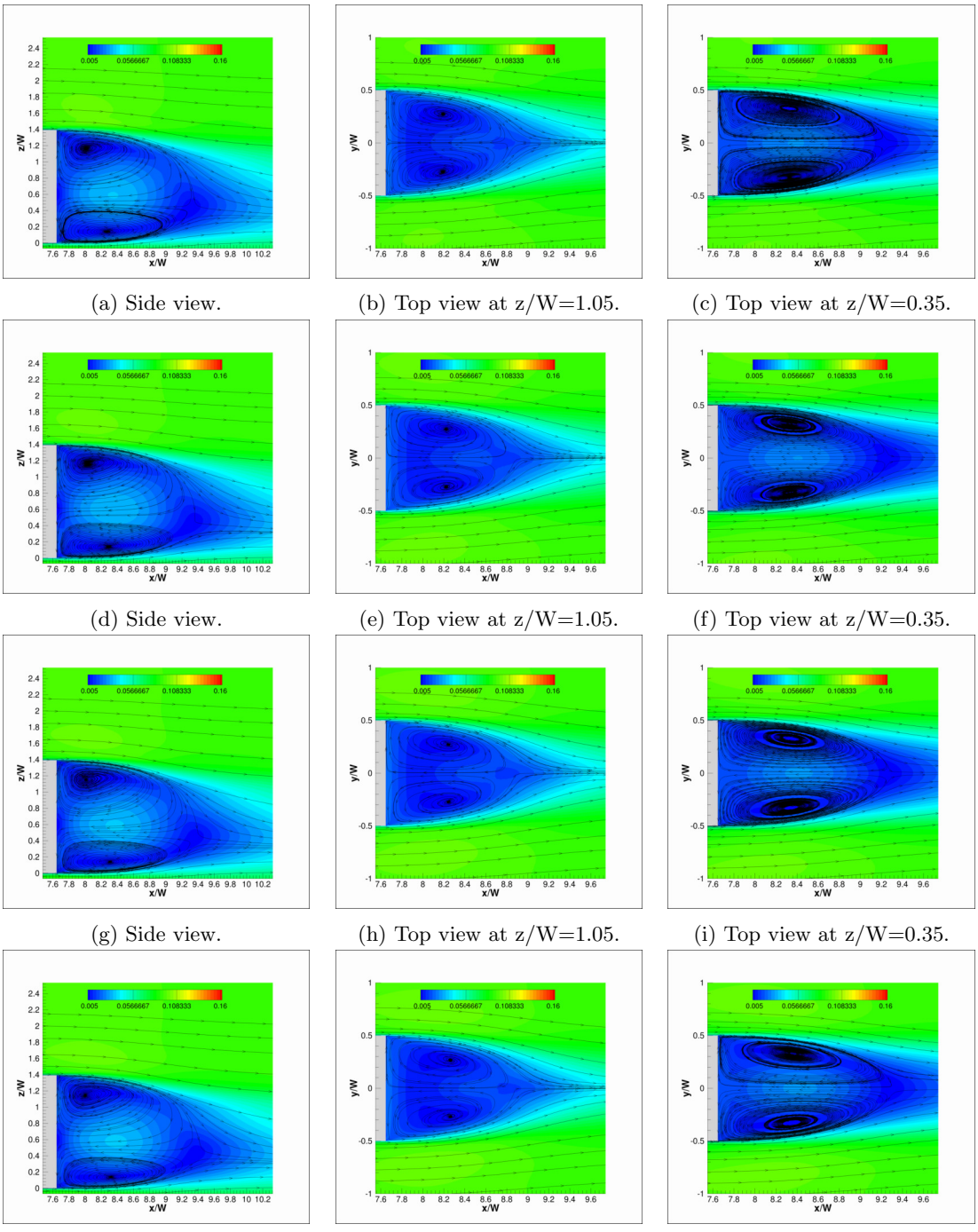

(a) Side view. (b) Top view at z/W=1.05. (c) Top view at z/W=0.35.

(d) Side view. (e) Top view at z/W=1.05. (f) Top view at z/W=0.35.

(g) Side view. (h) Top view at z/W=1.05. (i) Top view at z/W=0.35.

(j) Side view. (k) Top view at z/W=1.05. (l) Top view at z/W=0.35.

Figure 5.14: Mach number contours of the flow in the back of the base GTS model at different mesh resolutions. (a), (b), and (c) used the coarse level mesh, (d), (e), and (f) used the mid level mesh, (g), (h), and (i) used the fine level mesh, and (j), (k), and (l) used the extra fine level mesh.

It is clear that as the resolution increases in this region, the general wake structure, length, and overall behavior stay constant. There are however small changes in the location of the wake's core, as can be seen in the side view of the wake. Furthermore, when looking at the core region from the top, it can be seen that it grows in diameter and speed as the mesh resolution increases.

The changes in the wake can be better quantified when looking at the pressure response in the back of the vehicle. Figure 5.15 shows the evolution of the pressure contour as the mesh changes.

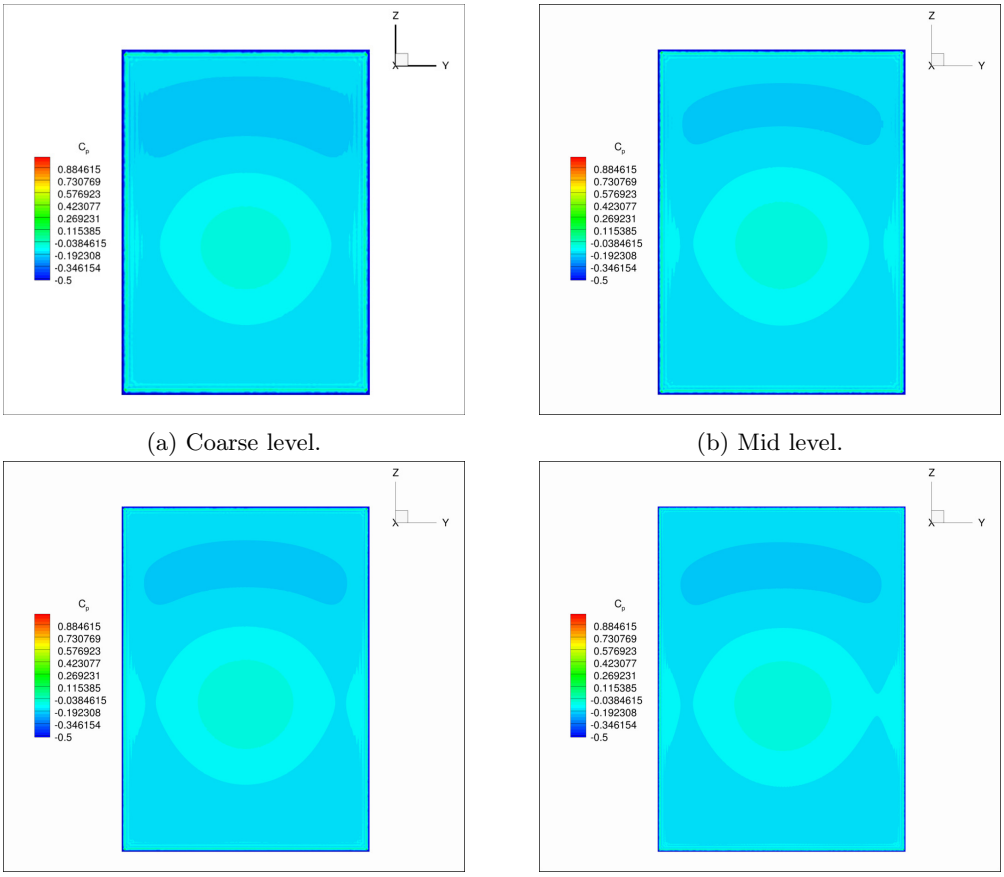

(a) Coarse level.

(b) Mid level.

(c) Fine level.

(d) Extra fine level.

Figure 5.15: Pressure distribution in the back of the GTS model at different mesh resolutions.

Starting from the edges of the trailer, it can be seen that as the resolution increases the low pressure in this region shrinks and is confined to a thinner region that outlines the contour. The ground effect causes asymmetry in the wake, as can be seen in Figure 5.14, and its effect in the pressure distribution at the back of the vehicle can be clearly seen by comparing the top and bottom half of the contours in Figure 5.15.

In the top half of the contour is a region of low-pressure that reduces its size as the resolution

increases, but the pressure level remains constant. The areas closer to the side gain definition and the edges are sharper. The overall effect is small compared with the front and the actual values can be seen in Table 5.2.

5.4 Enhanced Ground Transportation System

Once the Coanda jet-based system is mounted to the back of the GTS model the flow around the vehicle changes. The system was set to inject air in the back of the vehicle at the jet configuration found to obtain the optimum drag behavior in Chapter 4. The top and bottom jets where operated a momentum coefficient of 0.005625 and the side jets at 0.01.

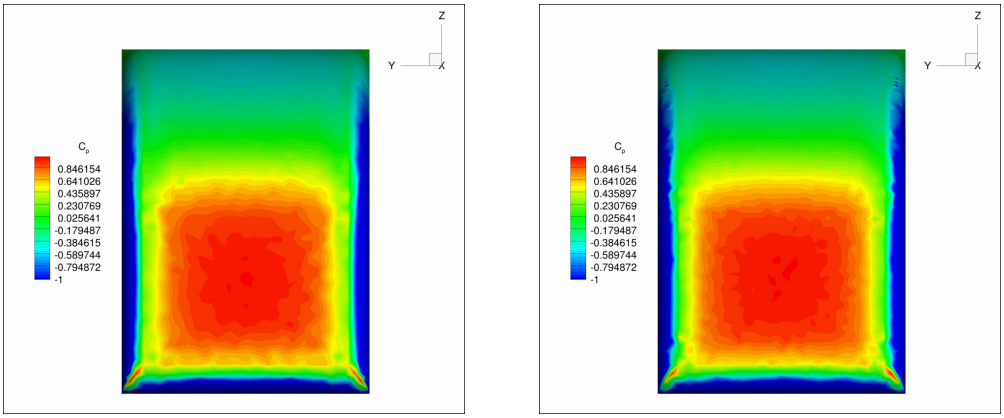

(a) Coarse level.

(b) Mid level.

(c) Fine level.

(d) Extra fine level.

Figure 5.16: Pressure distribution in the front of the enhanced GTS model at different mesh resolutions.

On average this geometry achieved 5 orders of magnitude of convergence across every mesh level used ranging from 3.3 in the Mid mesh to 7.2 orders of magnitude in the Coarse mesh. The drag

coefficient for this vehicle decreased from 0.2782 to 0.2475 as the mesh resolution went from 3.7 million points to 25 million points.

The pressure contour at the front of the vehicle can be seen in Figure 5.16 and are very similar to the pressure contours in the front of the base GTS. The stagnation point at the front of the vehicle becomes sharper and smoother as the resolution increases. The low-pressure regions located at the left, right, and bottom of the contour show a smoother expansion and, due to a better approximation of the rounded nature of the bottom corners, the stagnation points that appear in that region reduce its effect as mesh resolution increases. As can be seen in Table 5.3 the drag contribution from this region of the vehicle sharply decreases as the numerical representation approaches the true geometry of the vehicle. Figure 5.17 shows the flow structure in the front of the vehicle as the mesh resolution increases and the expansion in its top becomes sharper, but no major structural differences take place.

Mesh Level	C_D	$C_{D\ Pressure}$	$C_{D\ Friction}$	$C_{D\ Front}$	$C_{D\ Back}$
Coarse	0.2782	0.1995	0.0857	0.0749	0.1176
Mid	0.2796	0.1996	0.0860	0.0744	0.1191
Fine	0.2611	0.1767	0.0902	0.0512	0.1197
Extra Fine	0.2475	0.1592	0.0930	0.0317	0.1227

Table 5.3: Drag breakdown for the GTS model outfitted with an AFC system. C_D is the vehicle drag coefficient, $C_{D\ Pressure}$ is the pressure contribution to drag, $C_{D\ Friction}$ is the viscous friction contribution to drag, $C_{D\ Front}$ is the pressure contribution to drag from the front of the vehicle, and $C_{D\ Back}$ is the pressure contribution to drag from the back of the vehicle.

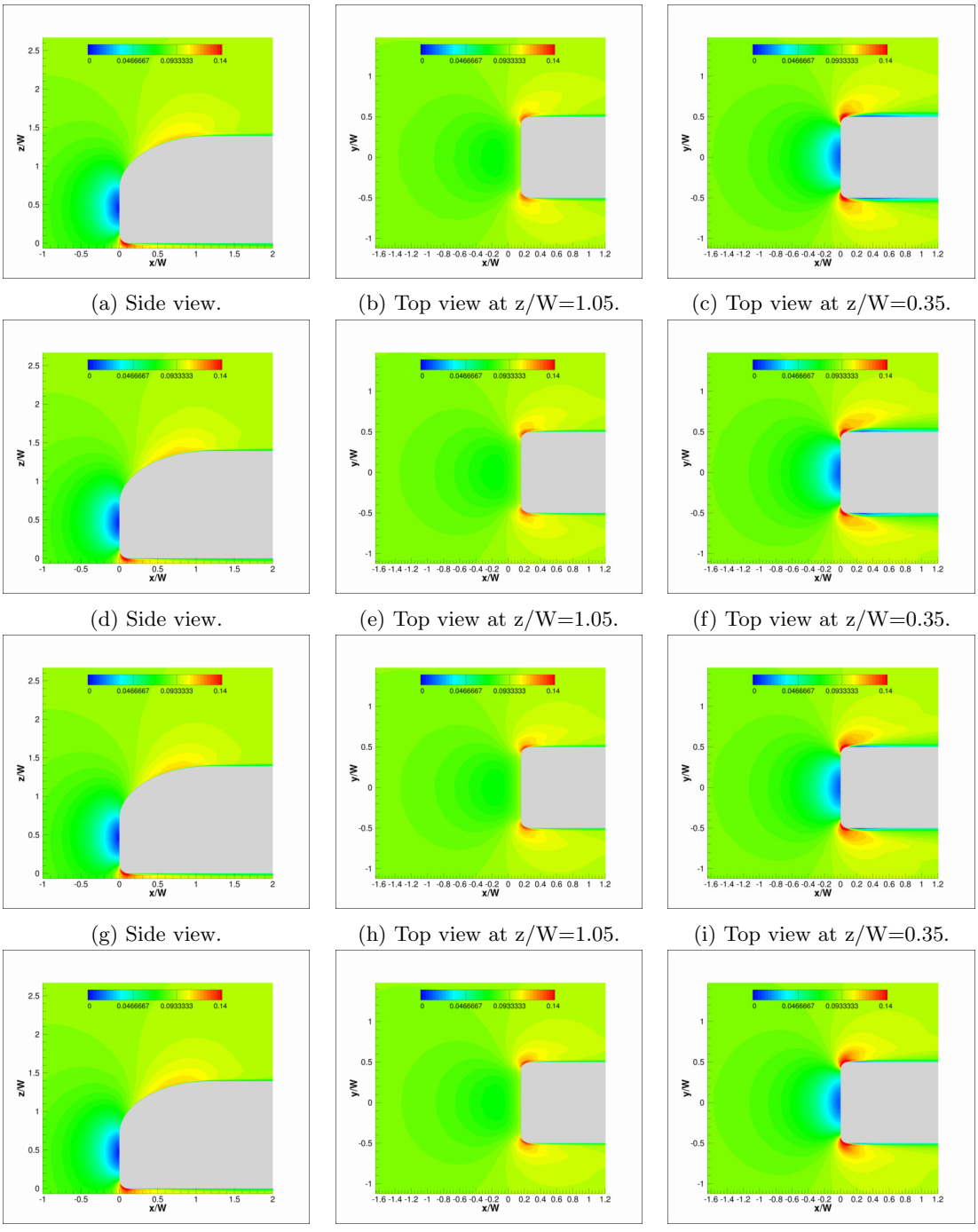

(a) Side view. (b) Top view at z/W=1.05. (c) Top view at z/W=0.35.

(d) Side view. (e) Top view at z/W=1.05. (f) Top view at z/W=0.35.

(g) Side view. (h) Top view at z/W=1.05. (i) Top view at z/W=0.35.

(j) Side view. (k) Top view at z/W=1.05. (l) Top view at z/W=0.35.

Figure 5.17: Mach number contours to visualize the flow structures in front of the GTS model outfitted with an AFC system at different mesh resolutions. (a), (b), and (c) used the coarse level mesh, (d), (e), and (f) used the mid level mesh, (g), (h), and (i) used the fine level mesh, and (j), (k), and (l) used the extra fine level mesh.

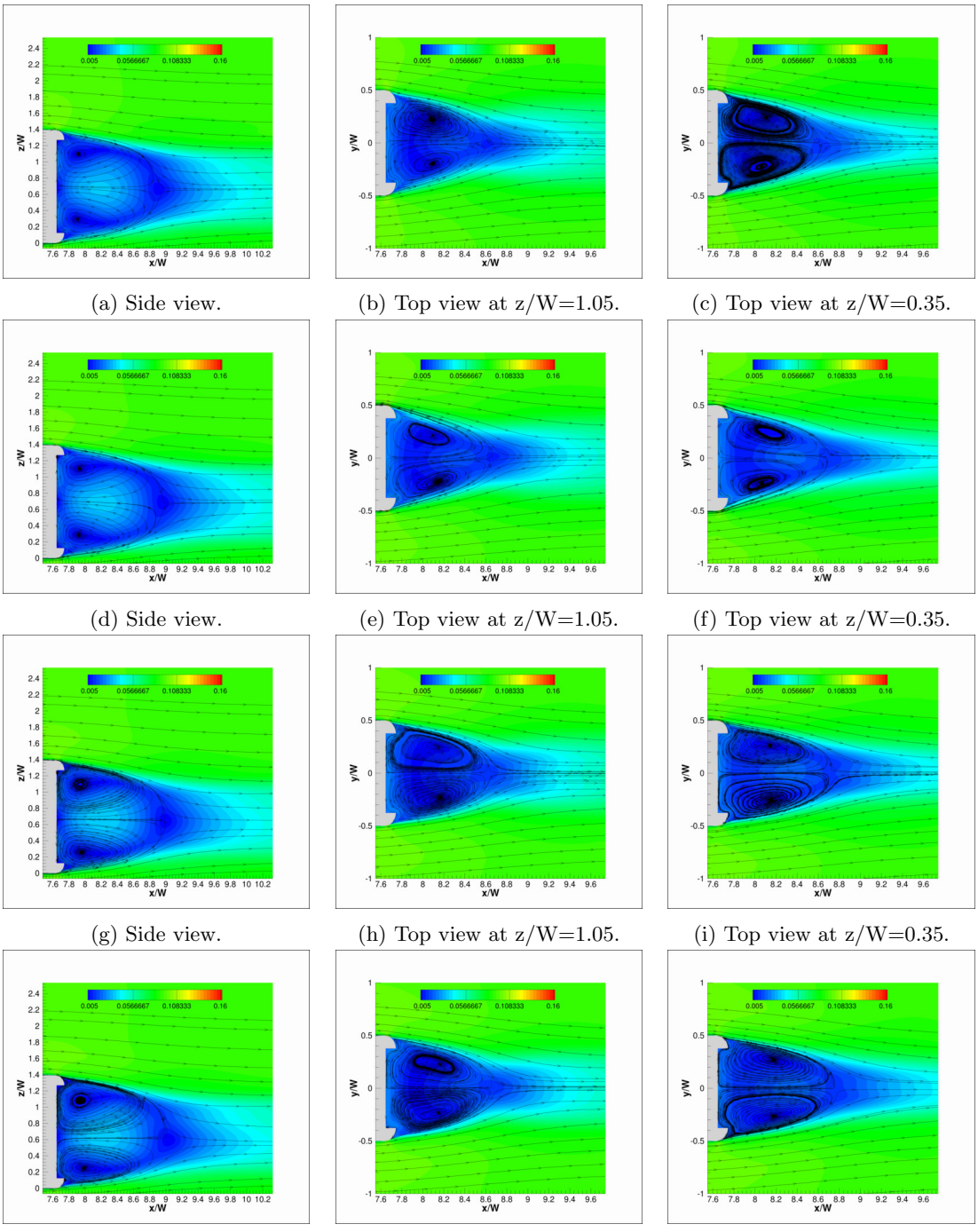

(a) Side view. (b) Top view at z/W=1.05. (c) Top view at z/W=0.35.

(d) Side view. (e) Top view at z/W=1.05. (f) Top view at z/W=0.35.

(g) Side view. (h) Top view at z/W=1.05. (i) Top view at z/W=0.35.

(j) Side view. (k) Top view at z/W=1.05. (l) Top view at z/W=0.35.

Figure 5.18: Mach number contours of the flow in the back of the GTS model outfitted with a AFC system at different mesh resolutions. (a), (b), and (c) used the coarse level mesh, (d), (e), and (f) used the mid level mesh, (g), (h), and (i) used the fine level mesh, and (j), (k), and (l) used the extra fine level mesh.

As can be seen from Figure 5.18, the structure of the wake, its length, and the overall behavior of it remain unchanged as the resolution increases, but the pressure distribution in the back of the vehicle does.

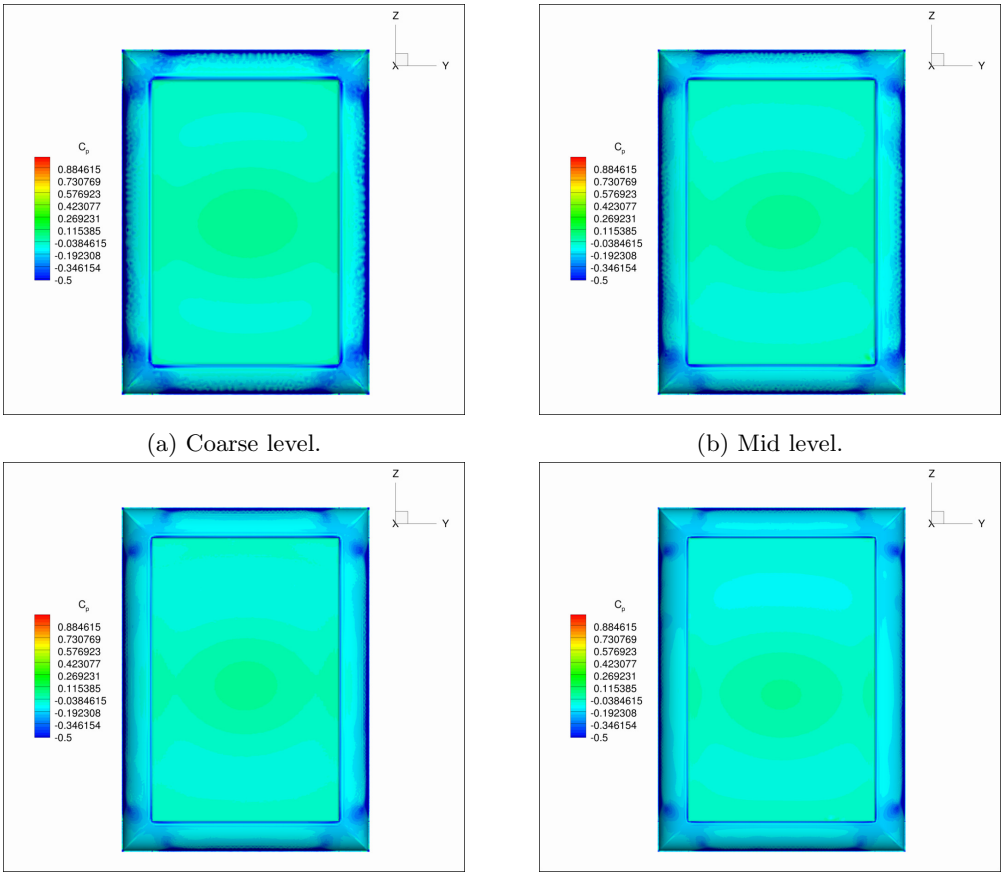

(a) Coarse level.

(b) Mid level.

(c) Fine level.

(d) Extra fine level.

Figure 5.19: Pressure distribution in the back of the enhanced GTS model at different mesh resolutions.

Figure 5.19 shows the change in behavior in the back of the GTS model outfitted with the Coanda jet-based AFC system as the mesh resolution changes. The pressure footprint of the jet injection significantly change as the mesh resolution increases, it smooths out the low pressure caused by the high speed jet, and spreads the effect of it through the entire Coanda surface. In the corners of the jet's nozzle, the increase in resolution revels the interaction between the injected air and the incoming flow. The high resolution representation of the vehicle unveil the ground effect by showing a vertical pressure gradient in the lateral Coanda surfaces. Finally, the pressure contour structure in the center remains relatively unchanged through the increase in resolution, but the high pressure region shrinks as the mesh count increases. By looking at Table 5.3 it can be determined that by

increasing the resolution in this part of the vehicle, the overall pressure distribution becomes slightly more negative and therefore it increases its contribution to the overall drag.

5.5 Design Outcomes

The increase in resolution in the simulation of the flow past the base and enhanced GTS models resulted in a decrease in drag for both geometries, as can be seen in Figure 5.20 and Table 5.4.

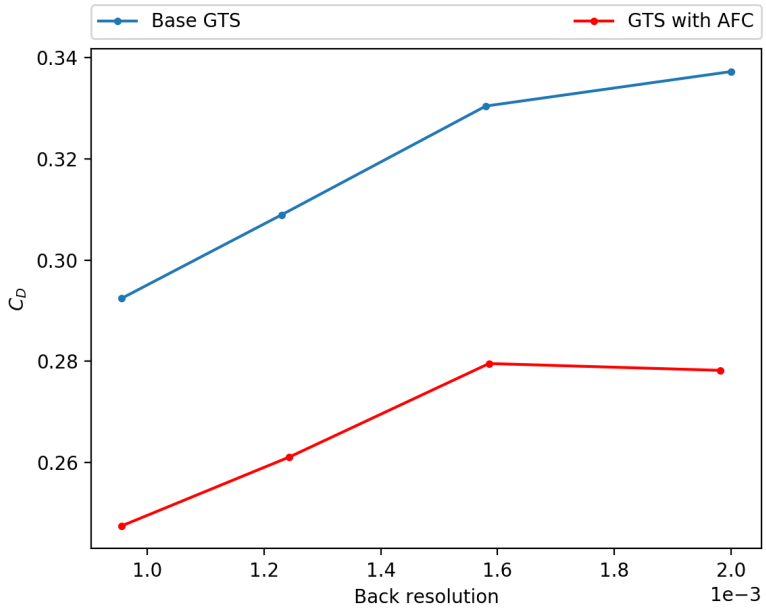

Figure 5.20: Drag coefficient history for the base and enhanced GTS models as the mesh resolution changes.

	C_D		$C_{D\ Front}$		$C_{D\ Back}$		
Mesh Level	***GTS***	***AFC***	***GTS***	***AFC***	***GTS***	***AFC***	ΔC_D
Coarse	0.3372	0.2782	0.0745	0.0749	0.1812	0.1176	17.5%
Mid	0.3304	0.2796	0.0739	0.0744	0.1742	0.1191	15.4%
Fine	0.3089	0.2611	0.0522	0.0512	0.1706	0.1197	15.5%
Extra Fine	0.2924	0.2475	0.0366	0.0317	0.1672	0.1227	15.4%

Table 5.4: Summary of the drag changes in the base GTS and model outfitted with an AFC system due to mesh resolution. C_D is the vehicle drag coefficient, $C_{D\ Front}$ is the pressure contribution to drag from the front of the vehicle, and $C_{D\ Back}$ is the pressure contribution to drag from the back of the vehicle, ΔC_D is the percentage change in drag due to the AFC system.

By observing the pressure contours on the vehicle, it is clear that the contribution from the back, which is the region being modified using the Coanda jet-based AFC system, is consistent at every mesh level. The main source of drag reduction, due to mesh refinement, is the front of the vehicle. This region reduces its drag contribution by over 50% as the resolution increases, since it is able to better represent the actual vehicle geometry. Figure 5.21 shows the change in drag contribution due to pressure for the front and back of the vehicle.

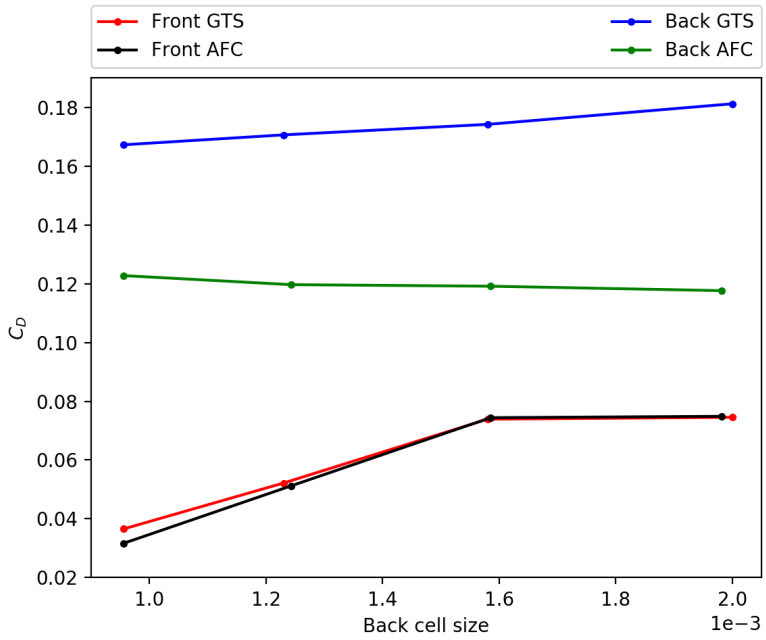

Figure 5.21: Base drag contribution history of the front and back of the base and enhanced GTS model as the mesh resolution changes.

By looking at Figure 5.20 and the percentage change in drag reported in Table 5.4, it is clear that as the mesh resolution increases the change in drag due to the introduction of the AFC system is consistent for all mesh levels. This outcome validates the use of coarse meshes for the design of drag reduction systems.

Chapter 6

Conclusions and Future Directions

This dissertation explores the use of computationally inexpensive tools for the analysis and design of heavy vehicle Active Flow Control (AFC) drag reduction systems. The presented work starts by evaluating the capabilities of the features in SU2 [20, 70, 69] for the simulation of bluff body aerodynamics. Using circular and square cylinders to test the effectiveness of these tools, the combination of Jameson-Schmidt-Turkel (JST) [42] numerical scheme and Shear-Stress-Transport (SST) [62] turbulence model proved to perform the best when compared with experimental results.

Using the selected numerical tools, the flow over a two-dimensional representation of the Ground Transportation System (GTS) model was simulated and the effects of adding Coanda jets analyzed. The jet strength and Coanda surface geometry were modified to understand the effect this system has on the aerodynamic performance of the vehicle. By tracking the drag, side force, and power consumption, the performance of the system was evaluated. To reduce the computational cost of exploring the design space a surrogate model approach was used. In addition to guiding the optimization process, the surrogate model served as a map to better understand the role each part of the AFC system plays. These optimization results were used to build a jet velocity profile and the Coanda surface geometry for the three-dimensional model.

Using the two-dimensional results as a guide, a representative three-dimensional system was developed. Leveraging the vertical stabilization effect of the ground and lateral stabilization capabilities of the AFC system, time was decoupled from the three-dimensional aerodynamic simulation. The integrated forces over the base GTS model were compared against experimental results found in the literature, and the use of a steady solver was validated. The power requirements and drag behavior of the vehicle were monitored as the jet injection strength was changed. Parametric and full-factorial studies were performed to better understand the effect of outfitting a GTS model with an AFC system and surrogate models for drag and power were generated to better understand the design space.

The use of a coarse grid to perform the design process significantly decreases its computational

cost to a level acceptable for industrial applications. To validate this approach, a grid refinement study was performed. Four different grid resolution levels, ranging from 2.7 to 25 million points, were used to study the flow around the GTS with and without the AFC system in the back. By looking at the integrated forces, the contribution to these by different parts of the vehicle, and exploring the changes in surface pressure as a function of grid resolution it was clear that the change in drag and power consumption due to the use of AFC systems is consistent across refinement levels, and that relatively coarse grids can be used for the design of AFC systems.

The research performed in this thesis has enabled the formulation of a computationally possible procedure for the design of drag reduction systems using the Coanda effect. It has also confirmed that a significant reduction of power consumption can be achieved with a purposefully designed system.

This dissertation has focused on the development of a computationally inexpensive approach for the design of AFC drag reduction systems. Future avenues of research involve:

- The use of higher fidelity simulation techniques, such as Detached Eddy Simulation (DES) and Large Eddy Simulation (LES), to further analyze the wake structure.
- Computational studies of the full-scale vehicle aerodynamic profile in order to quantify the effect of these AFC systems at higher Reynolds numbers.
- The use of shape and topology optimization to further optimize the Coanda surfaces.
- The use of unsteady jet injection to improve power consumption.
- The development of physical prototypes to validate the computational results.

Pursuing these areas of future research will contribute to shifting the direction of the trucking industry towards an eco-friendy future. Improving the design process and aerodynamic enhancements provided to these vehicles will reduce this industry's carbon footprint while reducing its operating costs.

Appendix A

Mesh Study Expanded

A.1 Coarse Level Grids

Base Ground Transportation System (GTS)

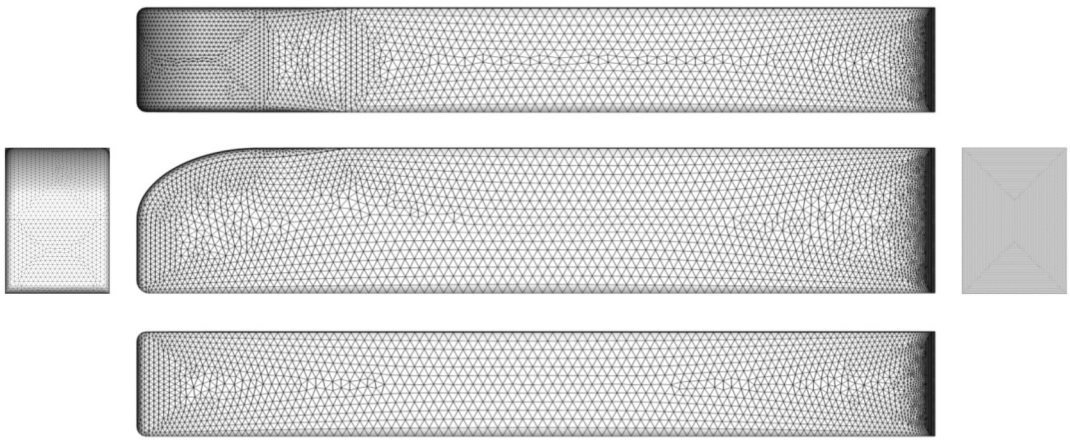

Figure A.1: Coarse level surface grid of the base GTS model.

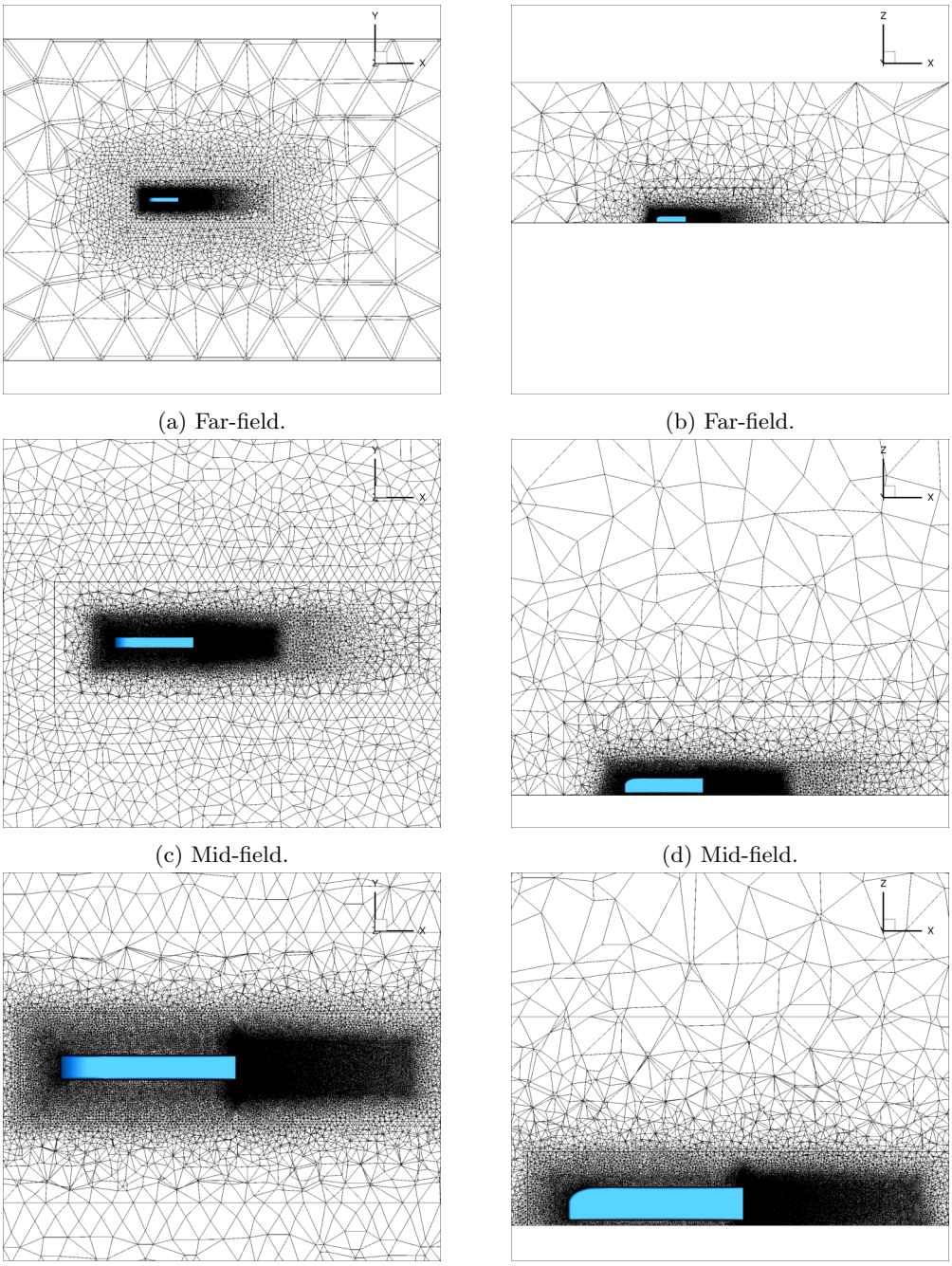

(a) Far-field.

(b) Far-field.

(c) Mid-field.

(d) Mid-field.

(e) Near-field.

(f) Near-field.

Figure A.2: Coarse level volume grid of the base GTS model. (a), (c), and (e) show the top view perspective of a grid slice located at 0.1 m from the bottom of the vehicle. (b),(d), and (f) show the side view perspective of a grid slice located a the center plane of the vehicle.

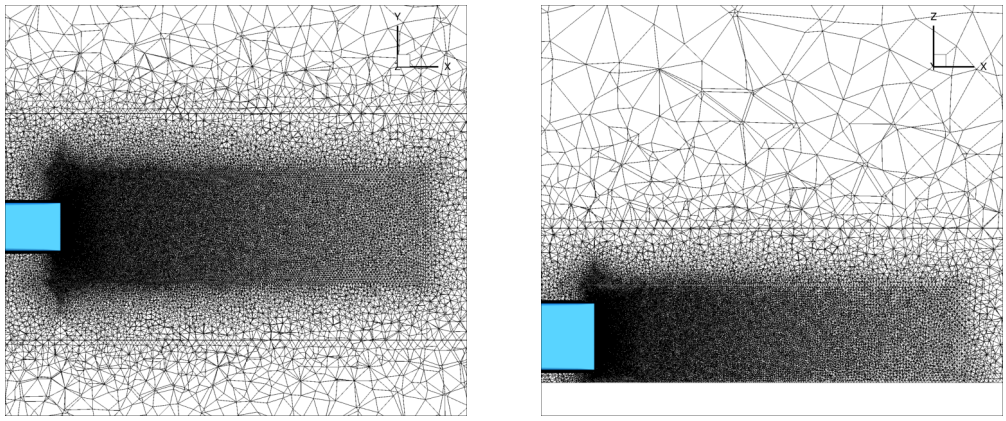

(a) Top view. (b) Side view.

Figure A.3: Coarse level volume grid of the wake region behind the base GTS model. (a) shows the top view perspective of a grid slice located at 0.1 m from the bottom of the vehicle, and (b) shows the side view perspective of a grid slice located a the center plane of the vehicle.

Enhanced GTS

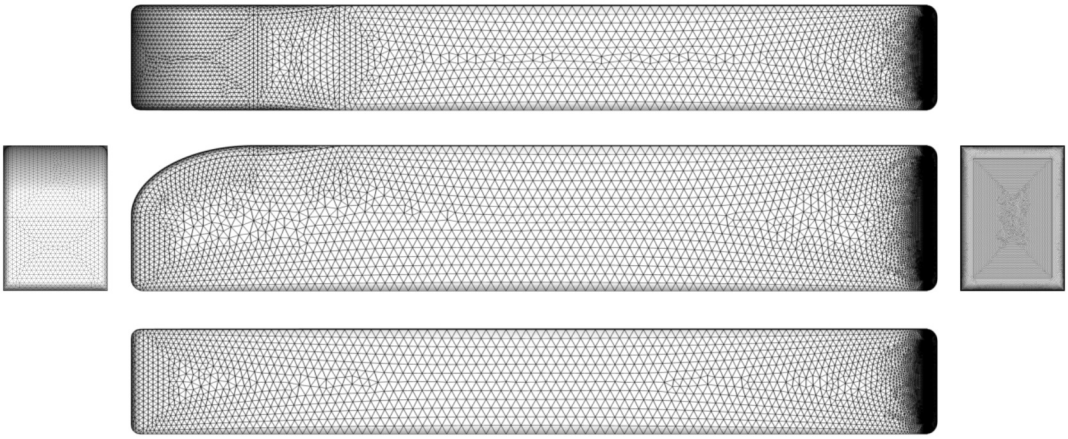

Figure A.4: Coarse level surface grid of the GTS model outfitted with the Active Flow Control (AFC) system.

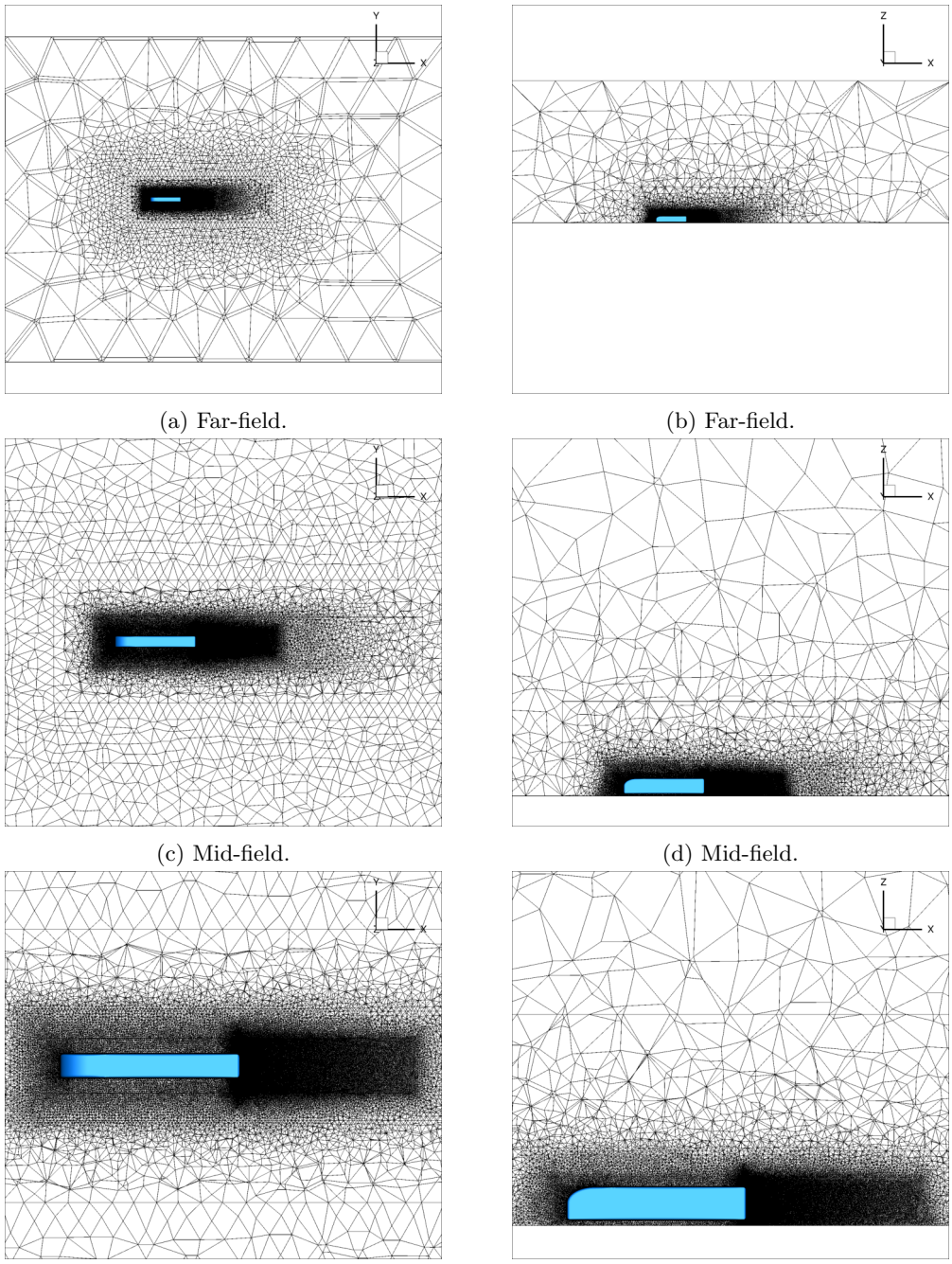

(a) Far-field.

(b) Far-field.

(c) Mid-field.

(d) Mid-field.

(e) Near-field.

(f) Near-field.

Figure A.5: Coarse level volume grid of the GTS model outfitted with the AFC system. (a), (c), and (e) show the top view perspective of a grid slice located at 0.1 m from the bottom of the vehicle. (b),(d), and (f) show the side view perspective of a grid slice located a the center plane of the vehicle.

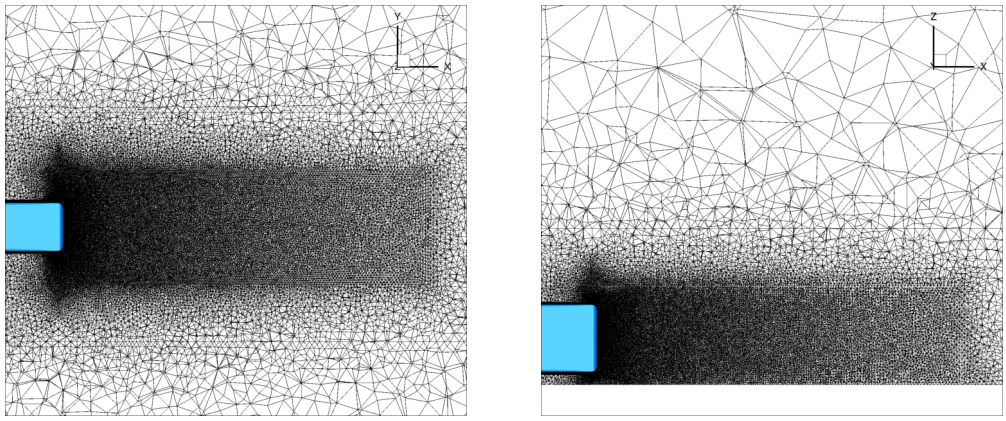

(a) Top view. (b) Side view.

Figure A.6: Coarse level volume grid of the wake region behind the GTS model outfitted with the AFC system. (a) shows the top view perspective of a grid slice located at 0.1 m from the bottom of the vehicle, and (b) shows the side view perspective of a grid slice located a the center plane of the vehicle.

A.2 Mid Level Grids

Base GTS

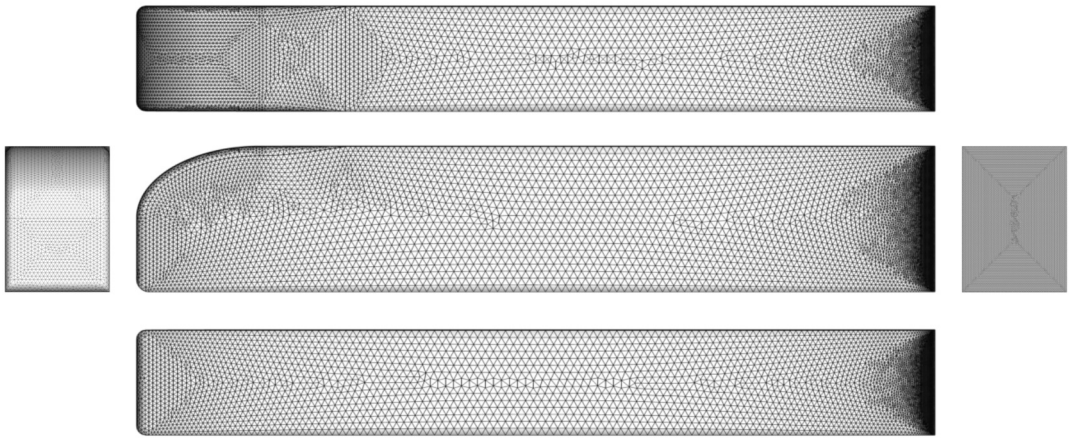

Figure A.7: Mid level surface grid of the base GTS model.

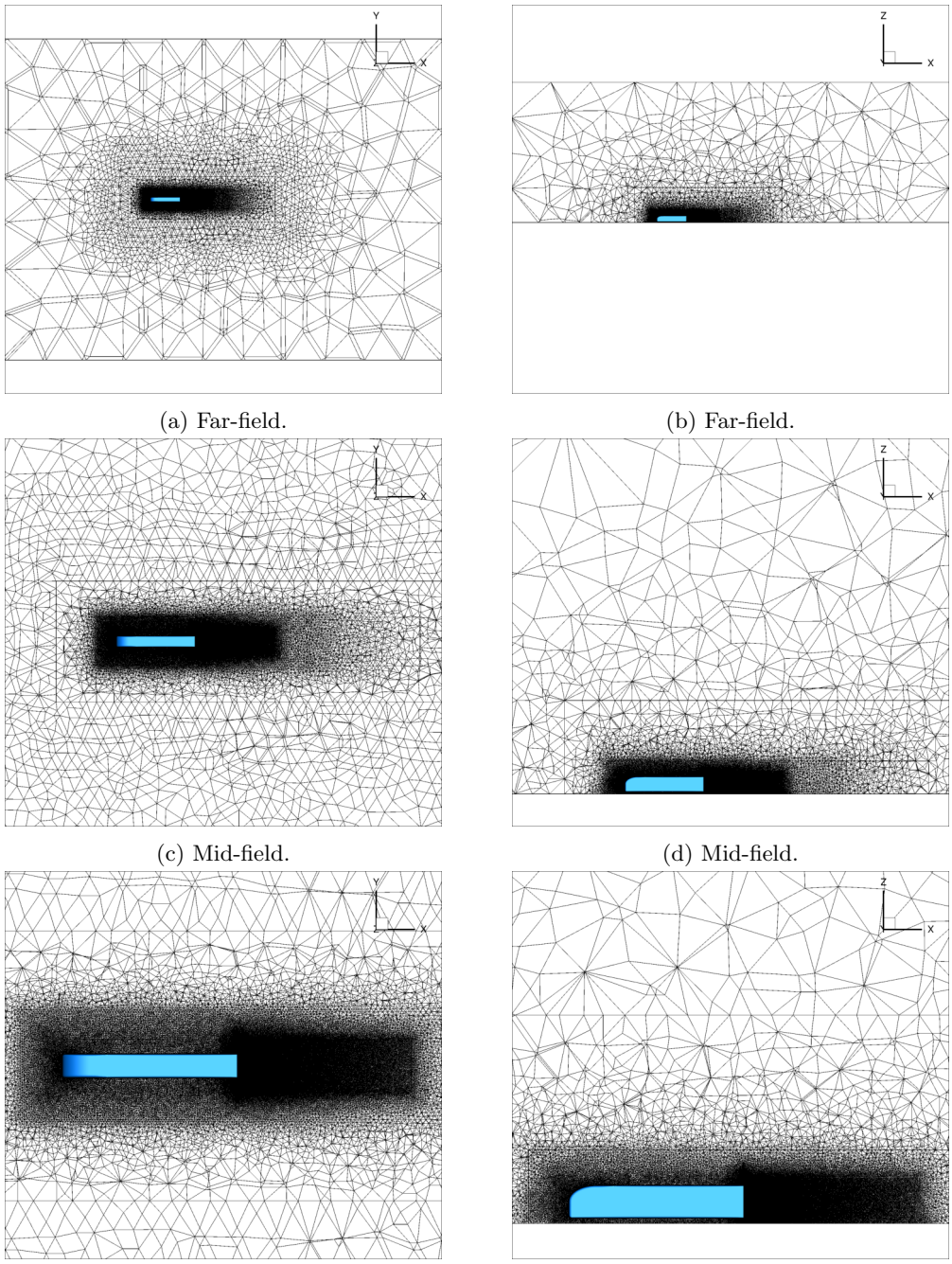

(a) Far-field.

(b) Far-field.

(c) Mid-field.

(d) Mid-field.

(e) Near-field.

(f) Near-field.

Figure A.8: Mid level volume grid of the base GTS model. (a), (c), and (e) show the top view perspective of a grid slice located at 0.1 m from the bottom of the vehicle. (b),(d), and (f) show the side view perspective of a grid slice located a the center plane of the vehicle.

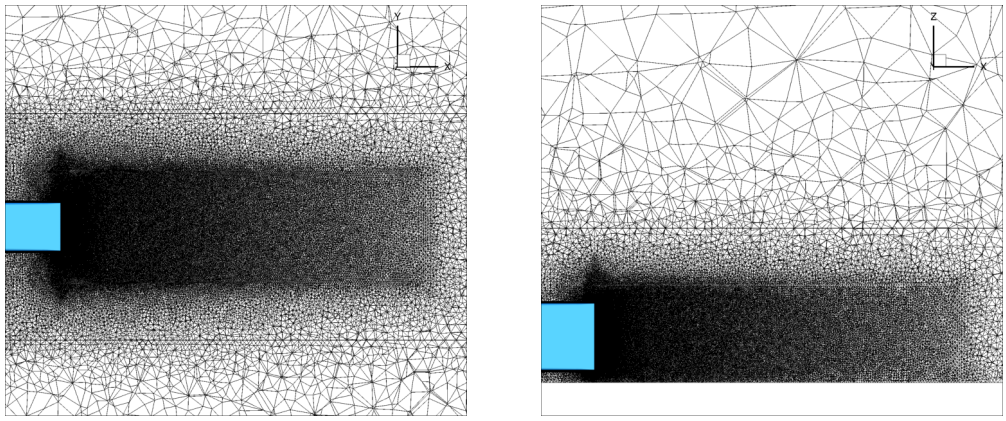

(a) Top view. (b) Side view.

Figure A.9: Mid level volume grid of the wake region behind the base GTS model. (a) shows the top view perspective of a grid slice located at 0.1 m from the bottom of the vehicle, and (b) shows the side view perspective of a grid slice located a the center plane of the vehicle.

Enhanced GTS

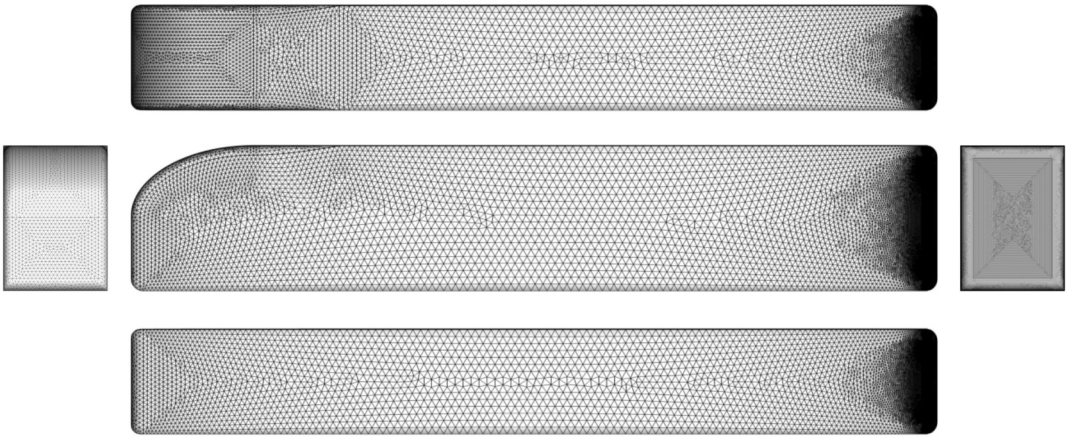

Figure A.10: Mid level surface grid of the GTS model outfitted with the AFC system.

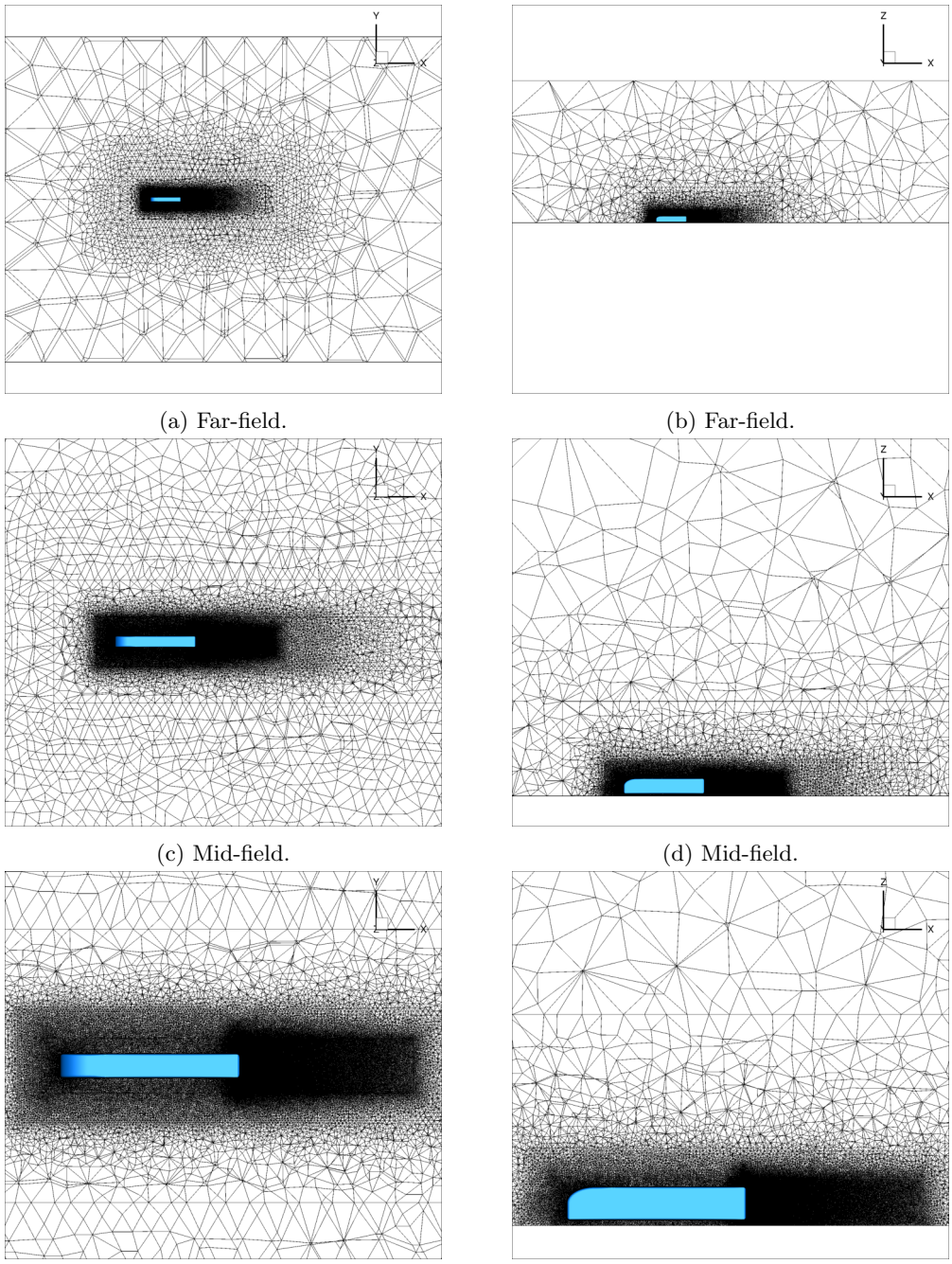

(a) Far-field.

(b) Far-field.

(c) Mid-field.

(d) Mid-field.

(e) Near-field.

(f) Near-field.

Figure A.11: Mid level volume grid of the GTS model outfitted with the AFC system. (a), (c), and (e) show the top view perspective of a grid slice located at 0.1 m from the bottom of the vehicle. (b),(d), and (f) show the side view perspective of a grid slice located a the center plane of the vehicle.

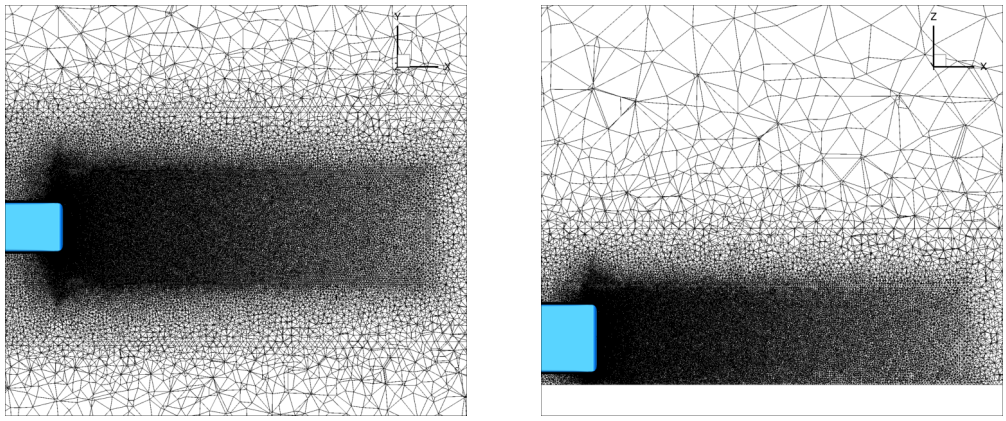

(a) Top view. (b) Side view.

Figure A.12: Mid level volume grid of the wake region behind the GTS model outfitted with the AFC system. (a) shows the top view perspective of a grid slice located at 0.1 m from the bottom of the vehicle, and (b) shows the side view perspective of a grid slice located a the center plane of the vehicle.

A.3 Fine Level Grids

Base GTS

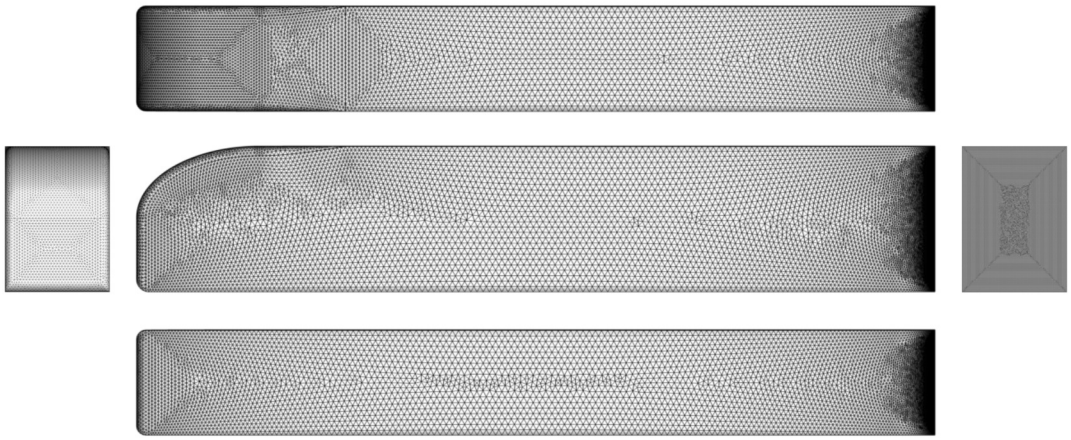

Figure A.13: Fine level surface grid of the base GTS model.

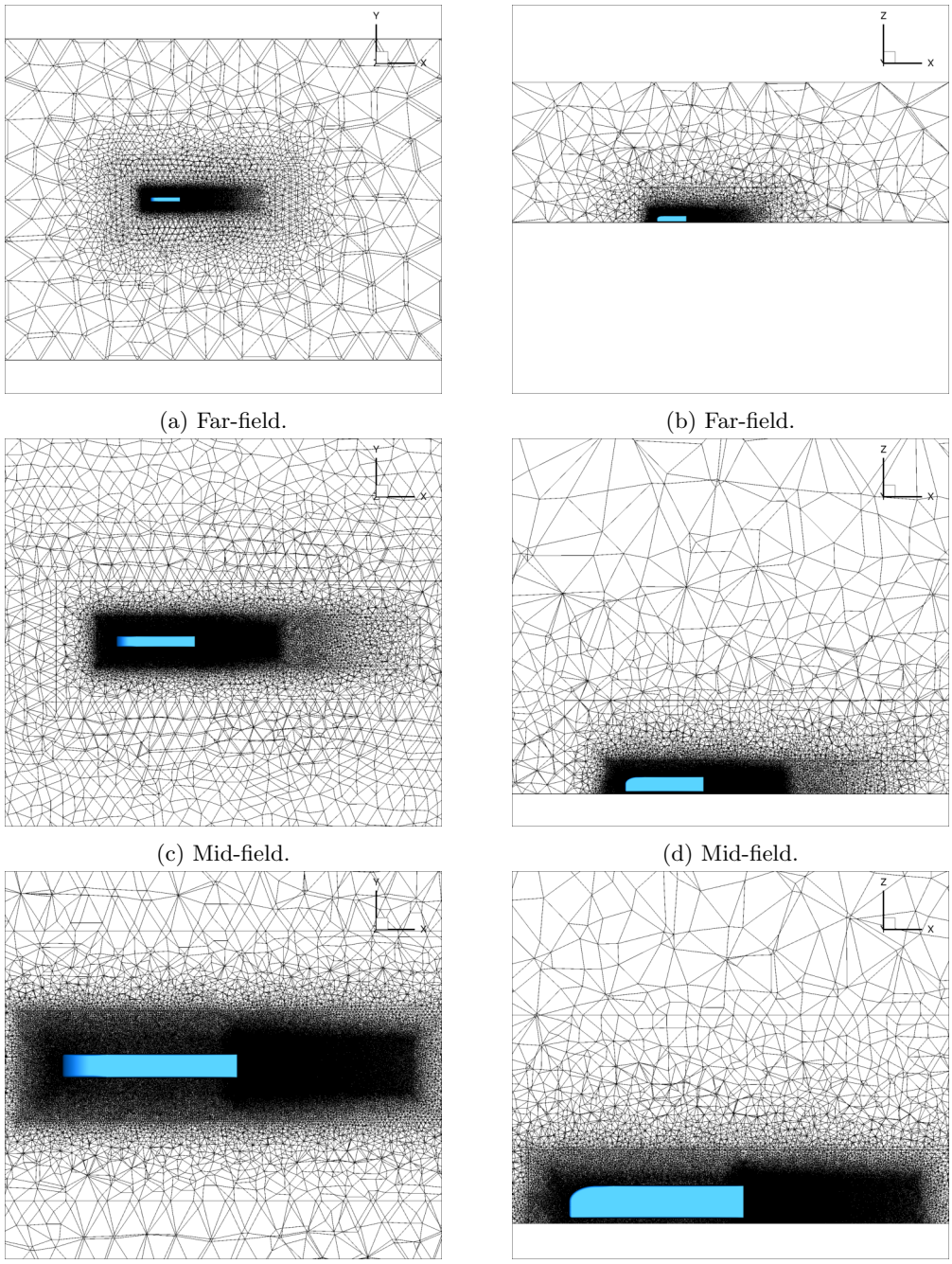

(a) Far-field.

(b) Far-field.

(c) Mid-field.

(d) Mid-field.

(e) Near-field.

(f) Near-field.

Figure A.14: Fine level volume grid of the base GTS model. (a), (c), and (e) show the top view perspective of a grid slice located at 0.1 m from the bottom of the vehicle. (b),(d), and (f) show the side view perspective of a grid slice located a the center plane of the vehicle.

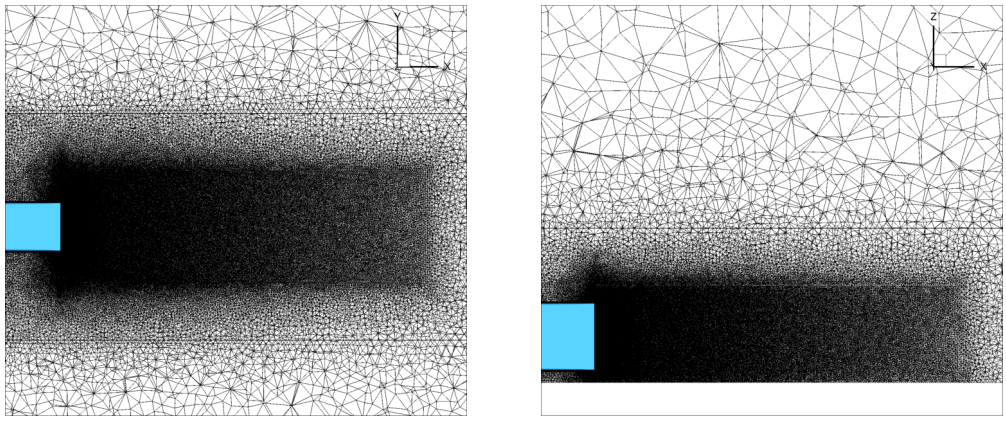

(a) Top view. (b) Side view.

Figure A.15: Fine level volume grid of the wake region behind the base GTS model. (a) shows the top view perspective of a grid slice located at 0.1 m from the bottom of the vehicle, and (b) shows the side view perspective of a grid slice located a the center plane of the vehicle.

Enhanced GTS

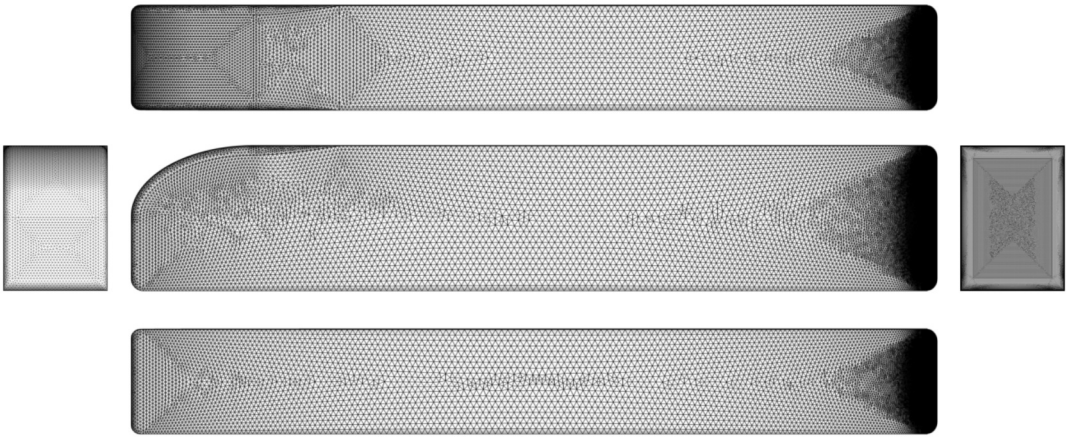

Figure A.16: Fine level surface grid of the GTS model outfitted with the AFC system.

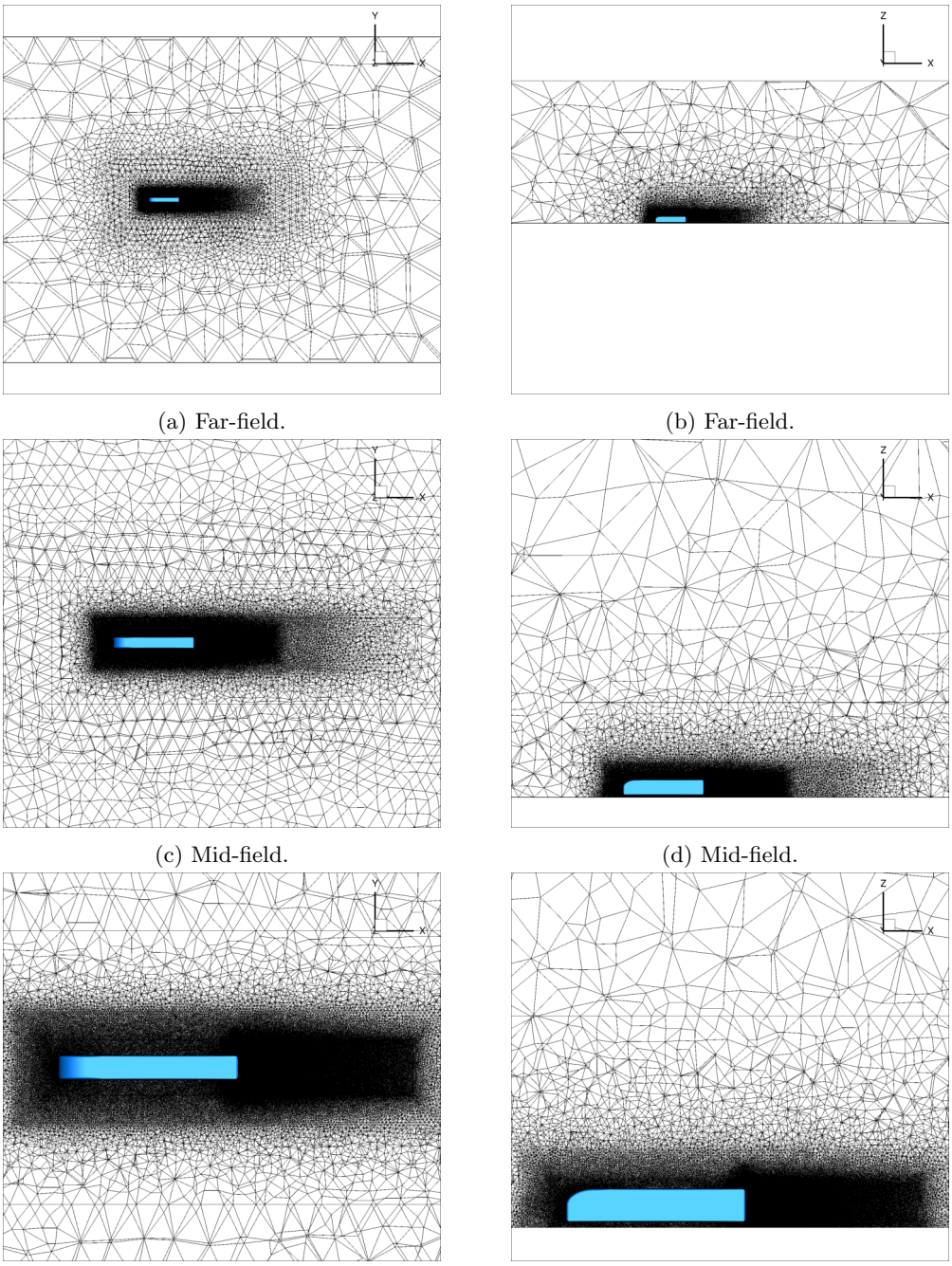

(a) Far-field. (b) Far-field.

(c) Mid-field. (d) Mid-field.

(e) Near-field. (f) Near-field.

Figure A.17: Fine level volume grid of the GTS model outfitted with the AFC system. (a), (c), and (e) show the top view perspective of a grid slice located at 0.1 m from the bottom of the vehicle. (b),(d), and (f) show the side view perspective of a grid slice located a the center plane of the vehicle.

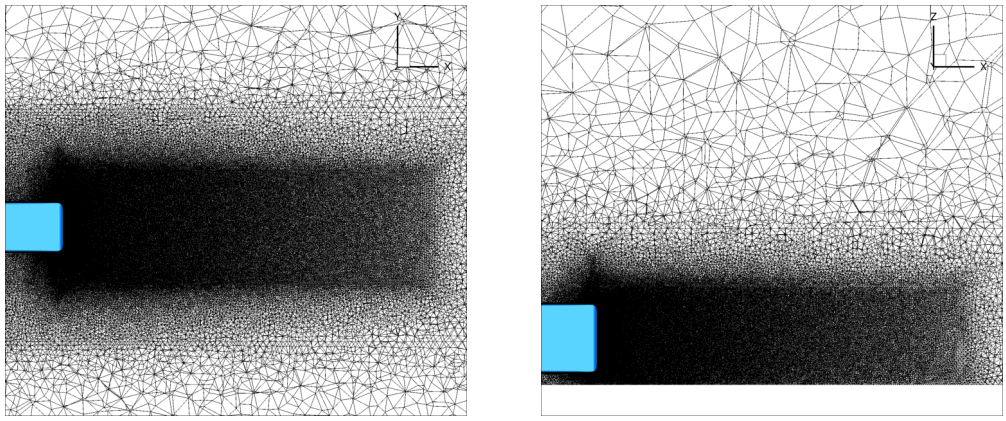

(a) Top view. (b) Side view.

Figure A.18: Fine level volume grid of the wake region behind the GTS model outfitted with the AFC system. (a) shows the top view perspective of a grid slice located at 0.1 m from the bottom of the vehicle, and (b) shows the side view perspective of a grid slice located a the center plane of the vehicle.

A.4 Extra Fine Level Grids

Base GTS

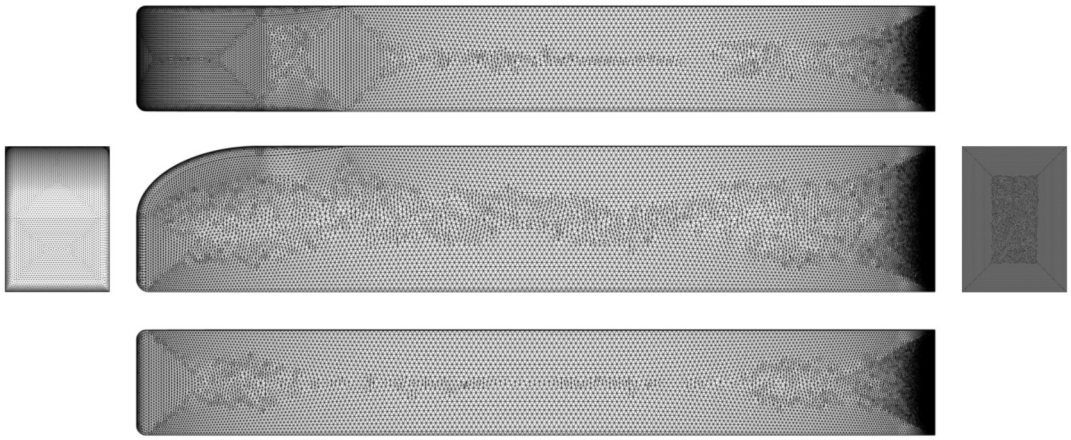

Figure A.19: Extra fine level surface grid of the base GTS model.

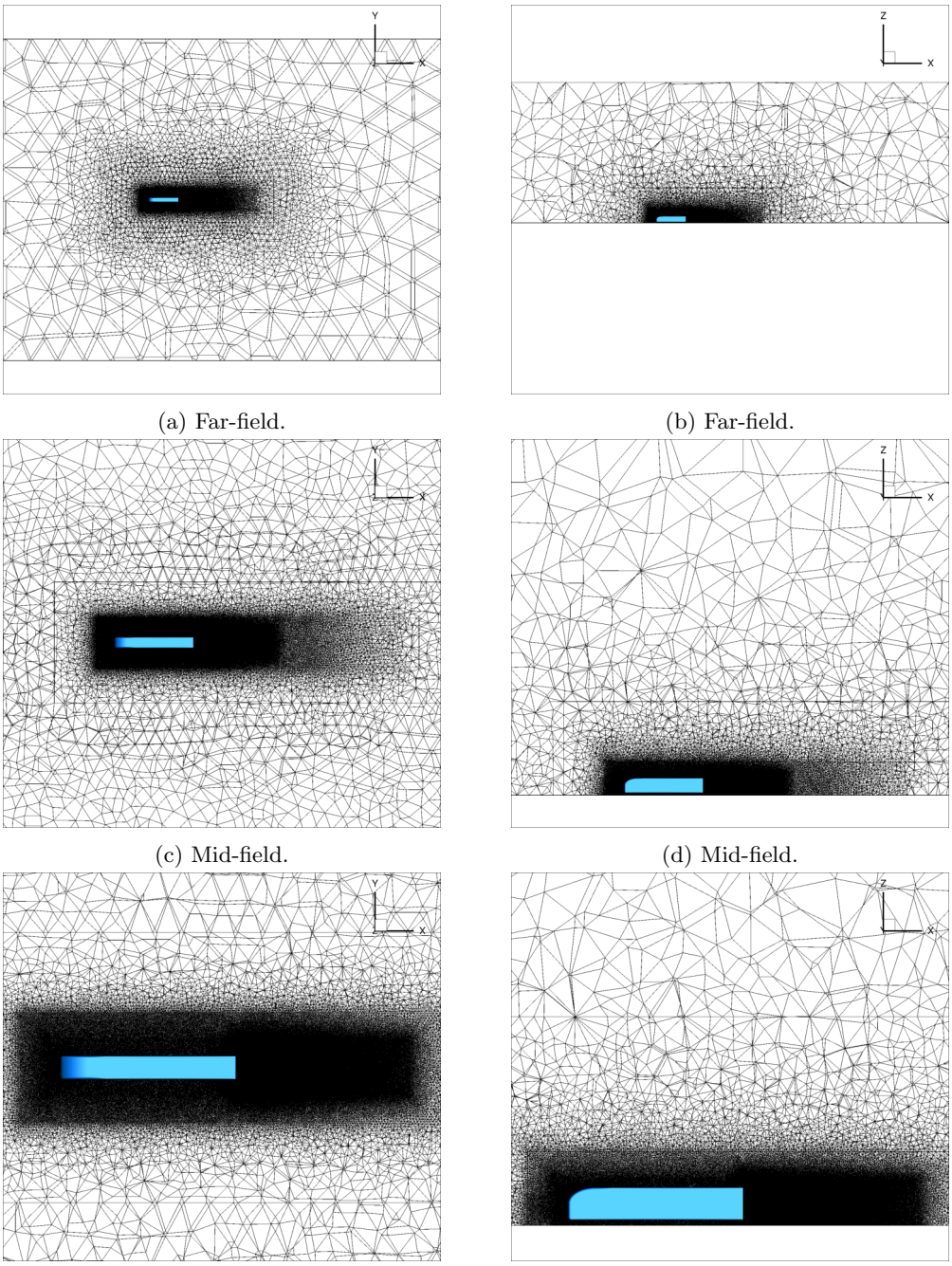

(a) Far-field.

(b) Far-field.

(c) Mid-field.

(d) Mid-field.

(e) Near-field.

(f) Near-field.

Figure A.20: Extra fine level volume grid of the base GTS model. (a), (c), and (e) show the top view perspective of a grid slice located at 0.1 m from the bottom of the vehicle. (b),(d), and (f) show the side view perspective of a grid slice located a the center plane of the vehicle.

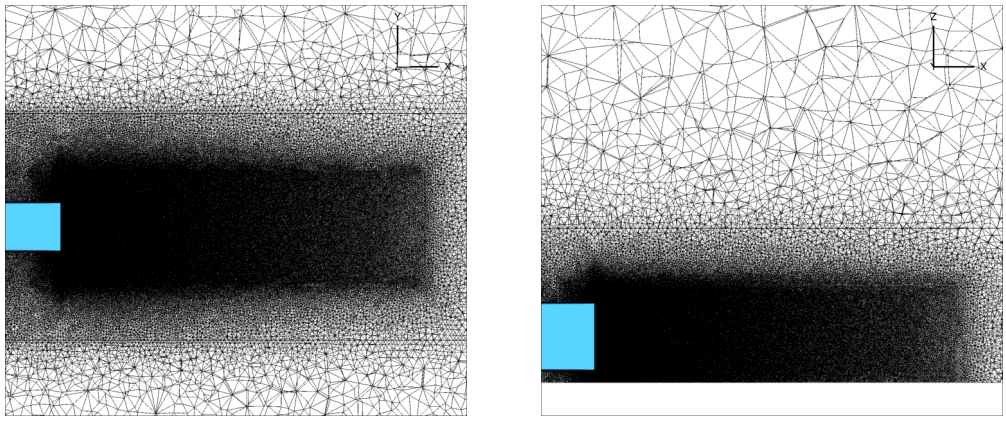

(a) Top view. (b) Side view.

Figure A.21: Extra fine level volume grid of the wake region behind the base GTS model. (a) shows the top view perspective of a grid slice located at 0.1 m from the bottom of the vehicle, and (b) shows the side view perspective of a grid slice located a the center plane of the vehicle.

Enhanced GTS

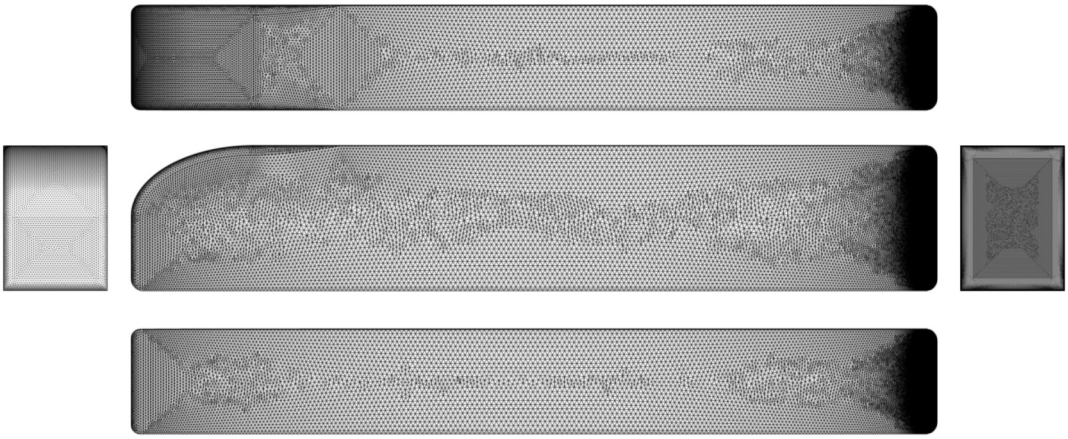

Figure A.22: Extra fine level surface grid of the GTS model outfitted with the AFC system.

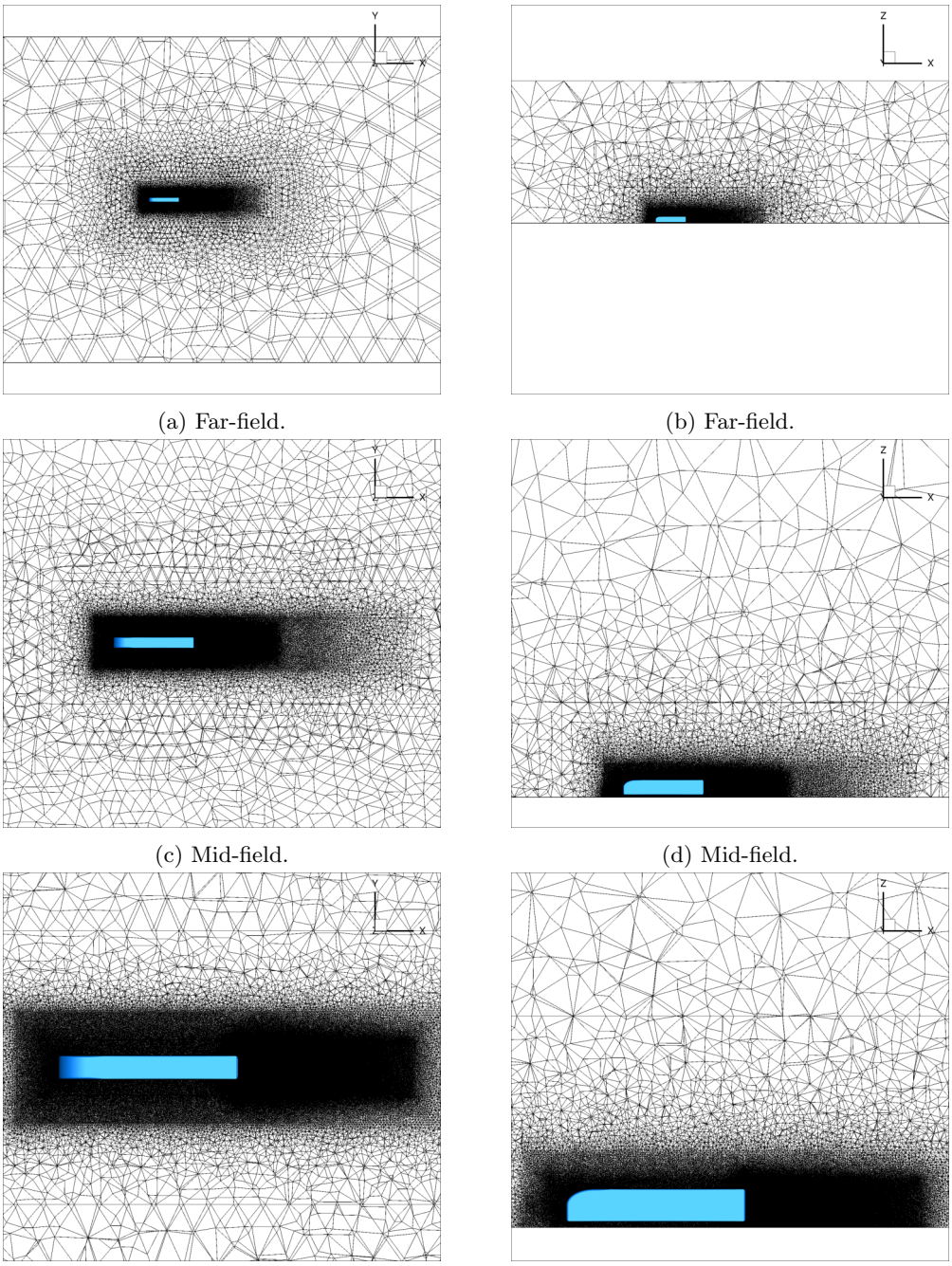

(a) Far-field.

(b) Far-field.

(c) Mid-field.

(d) Mid-field.

(e) Near-field.

(f) Near-field.

Figure A.23: Extra fine level volume grid of the GTS model outfitted with the AFC system. (a), (c), and (e) show the top view perspective of a grid slice located at 0.1 m from the bottom of the vehicle. (b),(d), and (f) show the side view perspective of a grid slice located a the center plane of the vehicle.

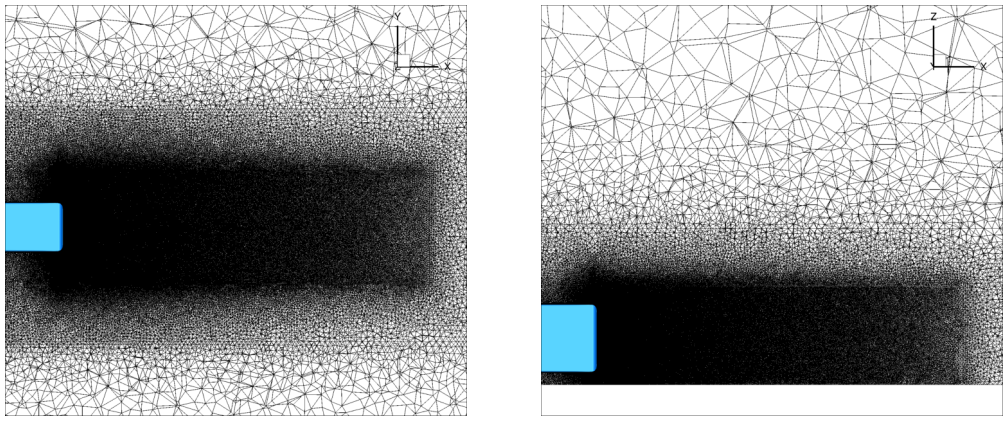

(a) Top view.

(b) Side view.

Figure A.24: Extra fine level volume grid of the wake region behind the GTS model outfitted with the AFC system. (a) shows the top view perspective of a grid slice located at 0.1 m from the bottom of the vehicle, and (b) shows the side view perspective of a grid slice located a the center plane of the vehicle.

Bibliography

[1] E Achenbach. Distribution of Local Pressure and Skin Friction Around a Circular Cylinder in Cross-Flow up to Re=5x10ˆ6. *Journal of Fluid Mechanics*, 1968.

[2] R Agarwal. Computational Study of Drag Reduction of Models of Truck-Shaped Bodies in Ground Effect by Active Flow Control. *SAE Technical Paper Series*, 2013.

[3] S Ahmed, R Gawthorpe, and P Mackrodt. Aerodynamics of Road and Rail Vehicles. *Vehicle System Dynamics*, 1985.

[4] S Ahmed, G Ramm, and G Faltin. Some Salient Features of the Time-Averaged Ground Vehicle Wake. *SAE Technical Paper Series*, 1984.

[5] J Allan. Aerodynamic Drag and Pressure Measurements on a Simplified Tractor-Trailer Model. *Journal of Wind Engineering and Industrial Aerodynamics*, 1981.

[6] American Trucking Association. American Trucking Trends 2017. Technical report, 2017.

[7] S Balkanyi, L Bernal, and B Khalighi. Analysis of the Near Wake of Bluff Bodies in Ground Proximity. In *Journal of Fluids Engineering*. American Society of Mechanical Engineers, 2002.

[8] T J Barth. Aspects of Unstructured Grids and Finite-Volume Solvers for the Euler and Navier-Stokes Equations. *NASA Technical Note*, 1992.

[9] F Browand, R McCallen, and J Ross. *The Aerodynamics of Heavy Vehicles II: Trucks, Buses, and Trains*. Springer, 2009.

[10] R Buil and L Ferrer. Aerodynamic Analysis of a Vehicle Tanker. *Journal of Fluids Engineering*, 2009.

[11] P Castellucci and K Salari. Computational Simulation of Tractor-Trailer Gap Flow with Drag-Reducing Aerodynamic Devices. *SAE Technical Paper Series*, 2005.

[12] P Catalano, M Wang, G Iaccarino, and P Moin. Numerical Simulation of the Flow Around a Circular Cylinder at High Reynolds Numbers. *International Journal of Heat and Fluid Flow*, 2003.

[13] H Choi, W Jeon, and J Kim. Control of Flow Over a Bluff Body. *Annual Review of Fluid Mechanics*, 2008.

[14] H Choi, J Lee, and H Park. Aerodynamics of Heavy Vehicles. *Annual Review of Fluid Mechanics*, 2013.

[15] K Cooper. Truck Aerodynamics Reborn - Lessons from the Past. *SAE Technical Paper Series*, 2003.

[16] K Cooper and J Leuschen. Model and Full-Scale Wind Tunnel Tests of Second-Generation Aerodynamic Fuel Saving Devices for Tractor-Trailers. *SAE Technical Paper Series*, 2005.

[17] R H Croll, W T Gutierrez, B Hassan, J E Suazo, and A J Riggins. Experimental Investigation of the Ground Transportion Systems (GTS) Project for Heavy Vehicle Drag Reduction. *SAE Technical Paper Series*, 1996.

[18] R P Dwight. Robust Mesh Deformation Using the Linear Elasticity Equations. *Computational Fluid Dynamics 2006*, 2006.

[19] T D Economon. *Optimal Shape Design Using an Unsteady Continuous Adjoint Approach*. PhD thesis, Stanford University, 2014.

[20] T D Economon, F Palacios, S R Copeland, T W Lukaczyk, and J J Alonso. SU2: An Open-Source Suite for Multiphysics Simulation and Design. *AIAA Journal*, 2016.

[21] M El-Alti. *Active Flow Control for Drag Reduction of Heavy Vehicles*. PhD thesis, Chalmers University of Technology, 2012.

[22] R Englar. Development of Pneumatic Aerodynamic Devices to Improve the Performance , Economics, and Safety of Heavy Vehicles. *SEA Technical Paper Series*, 2000.

[23] R Englar. Advanced Aerodynamic Devices to Improve the Performance, Economics, Handling, and Safety of Heavy Vehicles. *SAE Technical Paper Series*, 2001.

[24] R Englar. Application of Advanced Aerodynamic Technology to Ground and Sport Vehicles. *AIAA Applied Aerodynamics Conference*, 2008.

[25] R Englar, G Jones, B Allan, and J Lin. 2-D Circulation Control Airfoil Benchmark Experiments Intended for CFD Code Validation. *47th AIAA Aerospace Sciences Meeting Including The New Horizons Forum and Aerospace Exposition*, 2009.

[26] A Forrester, A Sobester, and A Keane. *Engineering Design Via Surrogate Modeling: A Practical Guide*. Wiley & Sons, 2008.

[27] P Gillieron and A Kourta. Aerodynamic Drag Reduction by Vertical Splitter Plates. *Experiments in Fluids*, 2010.

[28] H Gotz and G Mayr. Commercial Vehicles. In W Hucho, editor, *Aerodynamics of Road Vehicles*, chapter 9, pages 415–488. Society of Automotive Engineers, fourth edition, 1998.

[29] F Gowen and E Perkins. Drag of Circular Cylinders for a Wide Range of Reynolds Numbers and Mach Numbers. *NACA Technical Note*, 1953.

[30] W T Gutierrez, B Hassan, and H Robert. Aerodynamics Overview of the Ground Transportation Systems (GTS) Project for Heavy Vehicle Drag Reduction. *SAE International Congress and Exposition*, 1996.

[31] M Hammache and F Browand. On the Aerodynamics of Tractor-Trailers. In *The Aerodynamics of Heavy Vehicles: Trucks, Buses, and Trains*, pages 185–205. Springer, 2004.

[32] T Han, D Hammond, and C Sagi. Optimization of Bluff Body for Minimum Drag in Ground Proximity. *AIAA Journal*, 1992.

[33] T Han, V Sumantran, C Harris, T Kuzmanov, M Huebler, and T Zak. Flow-Field Simulations of Three Simplified Vehicle Shapes and Comparisons with Experimental Measurements. *SAE Technical Paper Series*, 1996.

[34] J Heineck, S Walker, and D Satran. The Measurement of Wake and Gap Flows of the Generic Conventional Truck Model (GCM) using Three-Component PIV. In *The Aerodynamics of Heavy Vehicles: Trucks, Buses, and Trains*, pages 173–184. Springer, 2004.

[35] C Hirsch. *Numerical Computation of Internal and External Flows*. Wiley & Sons, 1984.

[36] J Howell, A Sheppard, and A Blakemore. Aerodynamic Drag Reduction for a Simple Bluff Body Using Base Bleed. *SAE International*, 2003.

[37] W Hucho. *Aerodynamics of Road Vehicles*. Society of Automotive Engineers, fourth edition, 1998.

[38] D Hyams, K Sreenivas, R Pankajakshan, D Nichols, W Briley, and D Whitfield. Computational Simulation of Model and Full Scale Class 8 Trucks with Drag Reduction Devices. *Computers and Fluids*, 2011.

[39] G Iaccarino, A Ooi, P Durbin, and M Behnia. Reynolds Averaged Simulation of Unsteady Separated Flow. *International Journal of Heat and Fluid Flow*, 2003.

[40] A Jameson. Time Dependent Calculations Using Multigrid, with Applications to Unsteady Flows Past Airfoils and Wings. *10th AIAA Computational Fluid Dynamics Conference*, 1991.

[41] A Jameson. *A Perspective on Computational Algorithms for Aerodynamic Analysis and Design*. Elsevier, 2001.

[42] A Jameson, W Schmidt, and E Turkel. Numerical Solution of the Euler Equations by Finite Volume Methods Using Runge Kutta Time Stepping Schemes. *14th AIAA Fluid and Plasma Dynamics Conference*, jun 1981.

[43] B Khalighi, S Zhang, C Koromilas, S Balkanyi, L Bernal, G Iaccarino, and P Moin. Experimental and Computational Study of Unsteady Wake Flow Behind a Bluff Body with a Drag Reduction Device. *SAE Technical Paper Series*, 2001.

[44] T Kim, B Lee, D Lee, D Lee, J Hwang, and D Lee. A Study on Vortex Shedding Around a Bluff Body Near the Ground. *SAE Technical Paper Series*, 2003.

[45] G. Le Good and K. Garry. On the Use of Reference Models in Automotive Aerodynamics. *SAE Technical Paper Series*, 2004.

[46] B E Lee. The Effect of Turbulence on the Surface Pressure Field of a Square Prism. *Journal of Fluid Mechanics*, 1975.

[47] J Leuschen and K Cooper. Summary of Full-Scale Wind Tunnel Tests of Aerodynamic Drag-Reducing Devices for Tractor-Trailers. *Lecture Notes in Applied and Computational Mechanics*, 2009.

[48] R J LeVeque. *Finite Volume Methods for Hyperbolic Problems*. Cambridge University Press, 2002.

[49] R. P. Littlewood and M. Passmore. Aerodynamic Drag Reduction of a Simplified Squareback Vehicle Using Steady Blowing. *Experiments in Fluids*, 2012.

[50] T Lukaczyk. *Surrogate Modeling and Active Subspaces for Efficient Optimization of Supersonic Aircraft*. PhD thesis, Stanford University, 2015.

[51] D A Lyn, S Einav, W Rodi, and J H Park. A Laser-Doppler Velocimetry Study of Ensemble-Averaged Characteristics of the Turbulent Near Wake of a Square Cylinder. *Journal of Fluid Mechanics*, 1995.

[52] R MacCormack. *Numerical Computation of Compressible and Viscous Flow*. American Institute of Aeronautics and Astronautics, first edition, 2014.

[53] V Malviya, R Mishra, and J Fieldhouse. CFD Investigation of a Novel Fuel-Saving Device for Articulated Tractor-Trailer Combinations. *Engineering Applications of Computational Fluid Mechanics*, 2009.

[54] D E Manosalvas, T D Economon, C Othmer, and A Jameson. Computational Design of Drag Diminishing Active Flow Control Systems for Heavy Vehicles. *8th AIAA Flow Control Conference*, 2016.

[55] D E Manosalvas, T D Economon, F Palacios, and A Jameson. Finding Computationally Inexpensive Methods to Model the Flow Past Heavy Vehicles and the Design of Active Flow Control Systems for Drag Reduction. *32nd AIAA Applied Aerodynamics Conference*, jun 2014.

[56] D E Manosalvas, T D Economon, F Palacios, and A Jameson. Techniques for the Design of Active Flow Control Systems in Heavy Vehicles. *33rd AIAA Applied Aerodynamics Conference*, jun 2015.

[57] D E Manosalvas-Kjono, T D Economon, C Othmer, and A Jameson. Computations of Active Flow Control for Heavy Vehicle Drag Reduction. *35th AIAA Applied Aerodynamics Conference*, 2017.

[58] R McCallen, D Flowers, T Dunn, J Owens, F Browand, M Hammache, A Leonard, M Brady, K Salari, W Rutledge, J Ross, B Storms, J Heineck, D Driver, J Bell, S Walker, and G Zilliac. Aerodynamic Drag of Heavy Vehicles (Class 7-8): Simulation and Benchmarking. *SAE Technical Paper Series*, 2000.

[59] R McCallen, K Salari, J Ortega, P Castellucci, J Paschkewitz, C Eastwood, L Dechant, B Hassan, W Pointer, F Browand, C Radovich, T Merzel, D Plocher, A Leonard, M Rubel, J Ross, J Heineck, S Walker, B Storms, C Roy, D Whitfield, R Pankajakshan, L Taylor, K Sreenivas, and R Englar. DOE's Effort to Reduce Truck Aerodynamic Drag Through Joint Experiments and Computations. *34th AIAA Fluid Dynamics Conference and Exhibit*, 2005.

[60] R McCallen, K Salari, J Ortega, L DeChant, B Hassan, C Roy, W Pointer, F Browand, M Hammache, T Hsu, A Leonard, M Rubel, P Chatelain, R Englar, J Ross, D Satran, J Heineck, S Walker, D Yaste, and B Storms. DOE's Effort to Reduce Truck Aerodynamic Drag - Joint Experiments and Computations Lead to Smart Design. *34th AIAA Fluid Dynamics Conference and Exhibit*, 2004.

[61] J McManus and X Zhang. A Computational Study of the Flow Around an Isolated Wheel in Contact With the Ground. *Journal of Fluids Engineering*, 2006.

[62] F Menter. Two-Equation Eddy-Viscosity Turbulence Models for Engineering Applications. *AIAA Journal*, 1994.

[63] E Mercker and N Breuer. On the Aerodynamic Interference Due to the Rolling Wheels of Passenger Cars. *SAE Technical Paper Series*, 1991.

[64] Z Mohamed-Kassim and A Filippone. Fuel Savings on a Heavy Vehicle Via Aerodynamic Drag Reduction. *Transportation Research Part D: Transport and Environment*, 2010.

[65] V Muirhead and E Saltzman. Reduction of Aerodynamic Drag and Fuel Consumption for Tractor-Trailer Vehicles. *Journal of Energy*, 1979.

[66] J Ortega, T Dunn, R McCallen, and K Salari. Computational Simulation of a Heavy Vehicle Trailer Wake. In *The Aerodynamics of Heavy Vehicles: Trucks, Buses, and Trains*, pages 219–233. Springer, 2004.

[67] J Ortega and K Salari. An Experimental Study of Drag Reduction Devices for a Trailer Underbody and Base. *34th AIAA Fluid Dynamics Conference and Exhibit*, 2004.

[68] J Ortega, K Salari, and B Storms. Investigation of Tractor Base Bleeding for Heavy Vehicle Aerodynamic Drag Reduction. In *The Aerodynamics of Heavy Vehicles II: Trucks, Buses, and Trains*, pages 161–178. Springer, 2007.

[69] F Palacios, M Colonno, A Aranake, A Campos, S Copeland, T D Economon, A Lonkar, T Lukaczyk, T Taylor, and J J Alonso. Stanford University Unstructured (SU2): An Open-Source Integrated Computational Environment for Multi-Physics Simulation and Design. *51st AIAA Aerospace Sciences Meeting including the New Horizons Forum and Aerospace Exposition*, 2013.

[70] F Palacios, T D Economon, A Aranake, S Copeland, A Lonkar, T Lukaczyk, D E Manosalvas, K Naik, A S Padron, B Tracey, A Variyar, and J J Alonso. Stanford University Unstructured (SU2): Analysis and Design Technology for Turbulent Flows. *52nd AIAA Aerospace Sciences Meeting*, 2014.

[71] R Pankajakshan, B Mitchell, and D Whitfield. Full-Scale Simulations of Drag Reduction Devices for Class 8 Trucks. *Lecture Notes in Applied and Computational Mechanics*, 2009.

[72] F Pedregosa, G Varoquaux, A Gramfort, V Michel, B Thirion, O Grisel, M Blondel, P Prettenhofer, R Weiss, V Dubourg, J Vanderplas, A Passos, D Cournapeau, M Brucher, M Perrot, and É Duchesnay. Scikit-learn: Machine Learning in Python. *Journal of Machine Learning Research*, 2011.

[73] R Peterson. Drag Reduction by the Adoption of a Boattail to a Box Shaped Vehicle. *NASA Technical Note*, 1981.

[74] J Pfeiffer and R King. Multivariable Closed-Loop Flow Control of Drag And Yaw Moment For A 3D Bluff Body. *6th AIAA Flow Control Conference*, 2012.

[75] S Pirozzoli, P Orlandi, and M Bernardini. The Fluid Dynamics of Rolling Wheels at Low Reynolds Number. *Journal of Fluid Mechanics*, 2012.

[76] T Regert and T Lajos. Description of Flow Field in the Wheelhouses of Cars. *International Journal of Heat and Fluid Flow*, 2007.

[77] W Rodi. Comparison of LES and RANS Calculations of the Flow Around Bluff Bodies. *Journal of Wind Engineering and Industrial Aerodynamics*, 1997.

[78] P Roe. Approximate Riemann Solvers, Parameter Vectors, and Difference Schemes. *Journal of Computational Physics*, 1981.

[79] A Roshko. On the Wake and Drag of Bluff Bodies. *Journal of the Aeronautical Sciences*, 1955.

[80] A Roshko. Experiments on the Flow Past a Circular Cylinder at Very High Reynolds Number. *Journal of Fluid Mechanics*, 1961.

[81] C Roy, J Brown, L DeChant, and M Barone. Unsteady Turbulent Flow Simulations of the Base of a Generic Tractor/Trailer. *34th AIAA Fluid Dynamics Conference and Exhibit*, 2004.

[82] C Roy, J Payne, and M McWherter-Payne. RANS Simulations of a Simplified Tractor/Trailer Geometry. *Journal of Fluids Engineering*, 2006.

[83] E Saltzman and R Meyer. A Reassessment of Heavy-Duty Truck Aerodynamic Design Features and Priorities. *NASA Technical Note*, 1999.

[84] J Samareh. Aerodynamic Shape Optimization Based on Free-Form Deformation. *10th AIAA/ISSMO Multidisciplinary Analysis and Optimization Conference*, 2004.

[85] D Schatzman, J Wilson, E Arad, A Seifert, and T Shtenedel. Flow Physics of Drag Reduction Mechanism using Suction and Pulsed Blowing. *AIAA Aerospace Science Meetings*, 2013.

[86] A Seifert, O Stalnov, D Sperber, G Arwatz, V Palei, S David, I Dayan, and I Fono. Large Trucks Drag Reduction Using Active Flow Control. In *46th AIAA Aerospace Sciences Meeting and Exhibit*. American Institute of Aeronautics and Astronautics, 2008.

[87] N Shao, G Yao, C Zhang, and M Wang. A New Method to Optimize the Wake Flow of a Vehicle : The Leading Edge Rotating Cylinder. *Mathematical Problems in Engineering*, 2017.

[88] P Spalart and S Allmaras. A One-Equatlon Turbulence Model for Aerodynamic Flows. *30th AIAA Aerospace Sciences Meeting and Exhibit*, 1992.

[89] B Storms, J Ross, J Heineck, S Walker, D Driver, and G Zilliac. An Experimental System Study of the Ground Transportation System (GTS) in the NASA Ames 7- by 10-Ft Wind Tunnel. *NASA Technical Note*, 2001.

[90] B Storms, D Satran, J Heineck, and S Walker. A Study of Reynolds Number Effects and Drag-Reduction Concepts on a Generic Tractor-Trailer. *34th AIAA Fluid Dynamics Conference and Exhibit*, 2004.

[91] B Storms, D Satran, J Heineck, and S Walker. A Summary of the Experimental Results for a Generic Tractor-Trailer in the Ames Research Center 7- by 10-Foot and 12-Foot Wind Tunnels. *NASA Technical Note*, 2006.

[92] W Sutherland. The Viscosity of Gases and Molecular Force. *The London, Edinburgh, and Dublin Philosophical Magazine and Journal of Science*, 1893.

[93] P van Leeuwen. *Computational Analysis of Base Drag Reduction Using Active Flow Control*. PhD thesis, Delft University of Technology, 2009.

[94] V Venkatakrishnan. On the Accuracy of Limiters and Convergence to Steady State Solutions. *31st AIAA Aerospace Sciences Meeting*, jan 1993.

[95] R Verzicco, M Fatica, G Iaccarino, P Moin, and B Khalighi. Large Eddy Simulation of a Road Vehicle with Drag-Reduction Devices. *AIAA Journal*, 2002.

[96] B J Vickery. Fluctuating Lift and Drag on a Long Cylinder of Cross Section in a Smooth and in a Turbulent Stream. *Journal of Fluid Mechanics*, 1966.

[97] M Vinokur. An Analysis of Finite-Difference and Finite-Volume Formulations of Conservation Laws. *Journal of Computational Physics*, 1989.

[98] J Weiss, J Maruszewski, and W Smith. Implicit Solution of the Navier-Stokes Equations on Unstructured Meshes. *13th AIAA Computational Fluid Dynamics Conference*, 1997.

[99] D Wilcox. *Turbulence Modeling for CFD*. DCW Industries, third edition, 1993.

[100] D Wong and W Mair. Boat-Tailed Afterbodies of Square Section as Drag-Reduction Devices. *Journal of Wind Engineering and Industrial Aerodynamics*, 1983.

[101] R Wood. Impact of Advanced Aerodynamic Technology on Transportation Energy Consumption. *SAE Technical Paper Series*, 2004.

[102] R Wood. A Discussion of a Heavy Truck Advanced Aerodynamic Trailer System. *9th AIAA International Symposium of Heavy Vehicle Weights and Dimensions*, 2006.

[103] R Wood. A Review of Reynolds Number Effects on the Aerodynamics of Commercial Ground Vehicles. *SAE International Journal of Commercial Vehicles*, 2012.

[104] R Wood and S Bauer. Simple and Low-Cost Aerodynamic Drag Reduction Devices for Tractor-Trailer Trucks. *SAE Technical Paper Series*, 2003.